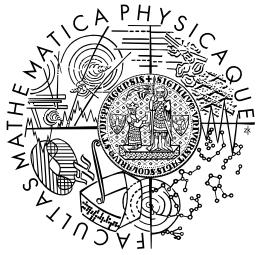

FACULTY
OF MATHEMATICS
AND PHYSICS
Charles University

MASTER THESIS

David Kománek

Re-accretion of wind and supernova matter onto a central black hole

Astronomical Institute of Charles University

Supervisor of the master thesis: Mgr. Richard Wünsch, Ph.D.
Study programme: Astronomy and Astrophysics

Prague 2025

I declare that I carried out this master thesis on my own, and only with the cited sources, literature and other professional sources. I understand that my work relates to the rights and obligations under the Act No. 121/2000 Sb., the Copyright Act, as amended, in particular the fact that the Charles University has the right to conclude a license agreement on the use of this work as a school work pursuant to Section 60 subsection 1 of the Copyright Act.

In ..... date ....

Author's signature

I am deeply grateful to my supervisor, Mgr. Richard Wünsch, Ph.D., for his wisdom, patience, and unwavering support throughout this journey. I would not have come this far without his guidance. I would also like to thank my advisor, Dr. Sergio Martínez-González, for his help with this project. A huge thanks goes to my family, especially my parents and brothers, for their constant love and support. You provided me with everything I needed to focus on this work. Thank you.

The software used in this work was developed in part by the DOE NNSA- and DOE Office of Science-supported Flash Center for Computational Science at the University of Chicago and the University of Rochester.

Title: Re-accretion of wind and supernova matter onto a central black hole

Author: David Kománek

Institute: Astronomical Institute of Charles University

Supervisor: Mgr. Richard Wünsch, Ph.D., Astronomical Institute, Academy of Sciences of the Czech Republic

Abstract: Massive stars which end their life as stellar mass black holes significantly reshape their surrounding interstellar medium (ISM) through fast stellar winds, ultraviolet ionizing radiation, and supernova ejecta. The black holes subsequently form within this modified environment. In this thesis, we explore whether black holes can accrete a significant amount of gas from this environment to explain the origin of relatively massive black holes that have been recently observed by gravitational waves. We present hydrodynamic simulations that incorporate key physical processes, including thermal conduction, radiative cooling, gravity, and radiation transport. We model the properties of interstellar bubbles across a broad parameter space, considering both scenarios where the progenitor star ends its life in a core-collapse supernova and those involving direct collapse into a black hole. Our results demonstrate that a supernova explosion heats the bubble interior so strongly that its cooling time becomes prohibitively long, making substantial accretion onto the black hole unlikely. The scenario with direct collapse seems to be, according to our results, more favorable for gas accretion from the stellar wind bubble. However, even in this case the models we were able to calculate did not result in a significant increase of the black hole mass.

Keywords: ISM: bubbles, stars: black holes, supernovae: general, hydrodynamics, methods: numerical

Název práce: Reakrece hmoty hvězdných větrů a supernov na černou díru.

Autor: David Kománek

Ústav: Astronomický ústav UK

Vedoucí bakalářské práce: Mgr. Richard Wünsch, Ph.D., Astronomický ústav Akademie věd České republiky, Oddělení galaxií

Abstrakt: Hmotné hvězdy, které končí svůj život jako černé díry, zásadně přetvářejí své mezihvězdné okolí prostřednictvím rychlého hvězdného větru, ionizujícího ultrafialového záření a výbuchů supernov. Černé díry tak vznikají v prostředí pozměněném jejich předchůdci. V této práci zkoumáme, zda nově vzniklé černé díry mohou v tomto prostředí akreovat dostatek plynu k vysvětlení vzniku relativně hmotných černých děr nedávno pozorovaných pomocí gravitačních vln. Představujeme hydrodynamické simulace zahrnující klíčové fyzikální procesy, jako je vedení tepla, chlazení vyzařováním, gravitace a přenos záření. Modelujeme vlastnosti mezihvězdných bublin napříč širokým spektrem parametrů. Uvažujeme dva scénáře: hvězdu, která končí svůj život supernovou, a hvězdu, která kolabuje přímo do černé díry. Naše výsledky ukazují, že výbuch supernovy natolik zahřeje vnitřek bubliny, že je její časová škála chlazení dlouhá a významná akrece nepravděpodobná. Scénář s přímým kolapsem se podle našich výsledků zdá být příznivější pro akreci plynu z mezihvězdné bubliny. Avšak ani v tomto případě modely, které jsme byli schopni vypočítat, nevedly k výraznému nárůstu hmotnosti černé díry.

Klíčová slova: mezihvězdné bubliny, černé díry, supernovy, hydrodynamika, numerické metody

Contents

1 Introduction

1.1 Stellar-mass black holes

The existence of black holes has long been established in the theoretical literature. Schwarzschild (1916) found the first exact solution of Einstein's equations of general relativity, which describes spacetime outside of a spherical, non-rotating, uncharged mass. This laid the foundation for black hole physics. Chandrasekhar (1931) calculated the upper limit to the mass of a white dwarf. When its mass exceeds about $1.4\,\mathrm{M}_\odot$[1], the electron degeneracy pressure cannot support the star against gravity, and it must collapse. Oppenheimer and Snyder (1939) studied the collapse of spherically symmetric dust clouds and showed that a sufficiently massive star must collapse indefinitely after it has exhausted all its nuclear fuel. This is the first modern model of black hole formation. Penrose (1965) showed that black holes must form singularities under general conditions without the need for spherical symmetry. From then on, black holes were no longer seen as mere artifacts of special solutions, but as real objects that could exist.

1.1.1 Overview of observations

The first observed stellar-mass black hole candidates were black hole X-ray binaries (BH-XRBs). They consist of a donor star and a compact object. As the star evolves, it overflows its Roche lobe and transfers gas to its companion, forming an accretion disk. The accretion disk heats up to very high temperatures ($\sim 10^9\,\mathrm{K}$) due to its viscosity and produces strong X-ray emission. The first widely accepted BH-XRB was the famous Cygnus X-1. The X-ray source was identified with a massive blue supergiant star (Bolton, 1972). The mass of the compact object is estimated to be $12.7\,\mathrm{M}_\odot$–$17.8\,\mathrm{M}_\odot$ (Ramachandran et al., 2025), which is far beyond the $3\,\mathrm{M}_\odot$ upper limit for neutron stars (Bombaci, 1996). Since then, there have been about 20 other confirmed cases of BH-XRBs (McClintock; Remillard, 2006; Corral-Santana et al., 2016), with many more candidates without sufficient mass measurements to confirm the presence of a black hole. A number of BH-XRBs show relativistic jets, confirming black hole presence. An example of such a system is GRS 1915+105 (I. F. Mirabel; Rodríguez, 1994).

Interferometric measurements from the Advanced LIGO (Aasi et al., 2015) and Advanced Virgo (Acernese et al., 2015) gravitational wave observatories have revolutionized the way we observe black holes. During the first three observing runs between September 2015 and March 2020, ninety binary mergers have been detected and published in the Gravitational-Wave Transient Catalog 3 (Abbott et al., 2023). An event is included in the catalog if it has at least a 50 % probability of being of astrophysical origin. Most of the events are mergers of two black holes, but there have also been a few detections of mergers of two neutron stars and of mergers of a neutron star with a black hole. Whether the component is a black

[1]The maximum mass published in the original paper was $0.91\,\mathrm{M}_\odot$. This would be for a white dwarf composed of heavier elements with a mean molecular mass per electron of $\mu = 2.5$. The value of $1.4\,\mathrm{M}_\odot$ is calculated with $\mu = 2.0$, which is for a white dwarf composed mostly of carbon and oxygen.

hole or a neutron star is determined by its mass. The individual masses of the components range from a few solar masses up to a hundred solar masses. The total mass of the binary can be up to $150\,\mathrm{M}_\odot$.

Black hole binaries without mass transfer cannot be detected via X-rays. The precise astrometry of Gaia (Gaia Collaboration et al., 2016) has allowed the detection of three stellar-mass black holes by the motion of their companions (El-Badry; Rix; Quataert, et al., 2023; El-Badry; Rix; Cendes, et al., 2023; Panuzzo et al., 2024). The latest, Gaia BH3, is the most massive, with $M = (32.70 \pm 0.82)\,\mathrm{M}_\odot$ (Panuzzo et al., 2024). Gaia Data Release 4 will contain a much larger number of binary systems than the currently available data releases and is expected to greatly increase the number of known systems with stellar-mass black holes.

OGLE-2011-BLG-0462 is the first confirmed isolated stellar-mass black hole (Sahu et al., 2022). It has been detected by microlensing with the Hubble Space Telescope and its mass is $6.0^{+1.2}_{-1.0}\,\mathrm{M}_\odot$ (Lam; Lu, 2023).

1.1.2 Formation mechanism

Stellar-mass black holes can form through several distinct pathways: the core-collapse supernova of a massive star, the direct collapse of a stellar core without a visible explosion, or the merger of compact objects, such as two neutron stars or lower-mass black holes (F. Mirabel, 2017; Gerosa; Fishbach, 2021). Recent observations have placed constraints on the masses and spins of black holes, giving us valuable insight into their formation. To explain the formation of stellar-mass black holes, we must first understand the evolution of single stars, including the mass-loss rate due to stellar wind and supernova explosions. In addition, we need to consider mergers in multiple systems and dense environments such as globular clusters and nuclear star clusters (Mapelli et al., 2021; Antonini; Romero-Shaw, et al., 2025). All of these processes introduce large uncertainties, making it difficult to draw confident conclusions about the formation of stellar-mass black holes.

Black holes formed from a single star

Single massive stars end their lives with either a core-collapse supernova, a direct collapse into a black hole, or a pair-instability supernova, depending on initial mass and metallicity (A. Heger; C. L. Fryer, et al., 2003).

The masses of black holes formed by the collapse of a single star are limited by the upper mass limit of stars. Figer (2005), Koen (2006), and Martins et al. (2008) suggest that there is an upper mass limit to the initial mass of stars at $150\,\mathrm{M}_\odot$. However, there is limited observational evidence that stars with initial masses up to $300\,\mathrm{M}_\odot$ may exist in the local universe (Crowther et al., 2010). Another possible formation channel could be from Population III stars (Kinugawa et al., 2021), which may have been much more massive than any of the stars observed today.

Massive stars experience significant mass loss due to their stellar wind. The mass-loss rate increases with the metallicity of the star (A. Heger; C. L. Fryer, et al., 2003; Vink; Sander, 2021). The mass ejected by the supernova further decreases the mass of the black hole.

Several studies have investigated whether massive stars will explode as supernovae and what will be the mass of the resulting compact objects (Ugliano et al.,

2012; Pejcha; Thompson, 2015; Ertl et al., 2016; Sukhbold et al., 2016; Müller et al., 2016; Ebinger et al., 2019). These studies show that the explosion properties can vary dramatically with the initial mass of the progenitor star. There is usually no upper or lower mass limit for a successful supernova explosion. Instead, a complex pattern emerges, with so-called islands of explodability, surrounded by regions of stars that collapse directly into a black hole. A comparison of the results of different studies can be found in figure 1.1. Most of the studies used supernova models calibrated to the Crab Nebula and SN 1987A. It remains unclear whether these events represent typical supernovae. The observational uncertainties and biases could affect the models used and their results.

Figure 1.2 shows the masses of compact remnants as a function of the zero-age main-sequence mass of the solar metallicity progenitors calculated by Sukhbold et al. (2016). The predicted black hole masses are below $15\,M_\odot$.

The cores of massive stars can undergo a process called pair instability. The creation of electron-positron pairs can lead to the partial or complete collapse of a star, placing constraints on the masses of black holes formed from single stars. If the temperature inside a star is sufficiently high ($> 10^9\,K$) while the density is relatively low, electron-positron pairs can be created (Fowler; Hoyle, 1964). The internal energy of the gas is converted into the rest mass of the created particles. This reduces the pressure and can lead to the collapse of the star.

If the mass of the helium core is greater than $133\,M_\odot$, nuclear burning is unable to reverse the collapse, and a black hole forms (C. L. Fryer et al., 2001; A. Heger; S. E. Woosley, 2002). Helium cores above $60\,M_\odot$–$65\,M_\odot$ will experience a pair instability supernova (PISN)—a single pulse strong enough to completely disrupt the star, with no compact remnant left. A lighter helium core with mass above $40\,M_\odot$–$45\,M_\odot$ will experience multiple pulsations until it loses enough mass to get out of that mass range. This is called a pulsating pair instability supernova (PPISN). The mass ejected in the pulsations can be up to $20\,M_\odot$, the energy of each pulse up to $10^{51}\,erg$ (Stan. E. Woosley; Alexander Heger, 2015).

The mass loss due to PPISNe and the complete destruction of stars by PISNe can cause a $\sim 50\,M_\odot$–$133\,M_\odot$ gap in the mass spectrum of black holes (Stevenson et al., 2019). However, if a star manages to retain its hydrogen envelope, the mass of the black hole formed by the star after the pulsations can be up to $70\,M_\odot$ (Belczynski et al., 2016). The heat deposited in the star during a PPISN can cause it to expand to over $100\,R_\odot$, which can trigger Roche lobe overflow or common envelope events in close binaries, and significantly modify the masses and spins of future black hole mergers (Marchant et al., 2019).

Studying the orbits of black holes could provide evidence for successful supernova explosions or direct collapse into a black hole. Several of the observed X-ray black holes have high peculiar velocities relative to their local environment. This can be due to a sudden mass loss of a high-mass component in a binary (Blaauw, 1961), dynamical interaction in dense stellar environments (Poveda et al., 1967; Allen, 2011), asymmetric supernova explosion (Shklovskii, 1970; Janka, 2013; Wongwathanarat et al., 2013), and black hole natal kicks (Bonnell; Pringle, 1995; Christopher L. Fryer; Kusenko, 2006). Natal kicks can be imparted to a black hole at birth by asymmetric gravitational waves (Bonnell; Pringle, 1995) or asymmetric neutrino emission (Gourgoulhon; Haensel, 1993; Christopher L. Fryer; Kusenko, 2006) during core collapse. Natal kicks have been proposed to explain the peculiar

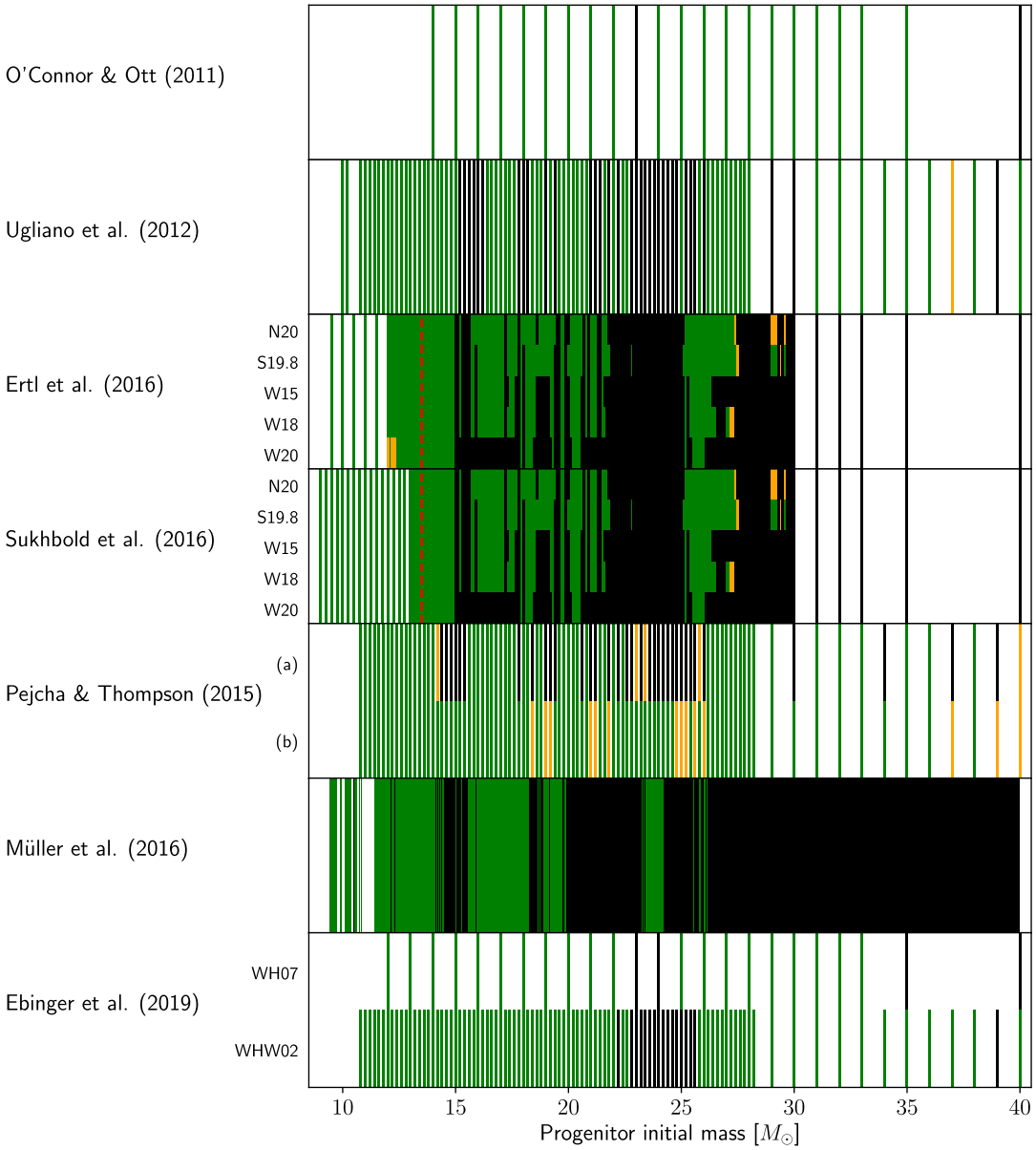

Figure 1.1 Comparison of different models of stellar core-collapse as a function of the initial mass of the star. All models are for stars of solar metallicity. Black bars show direct collapse to a black hole, green bars show successful supernova explosions and orange bars show supernova explosions with significant fallback. Reprinted from Pejcha (2020).

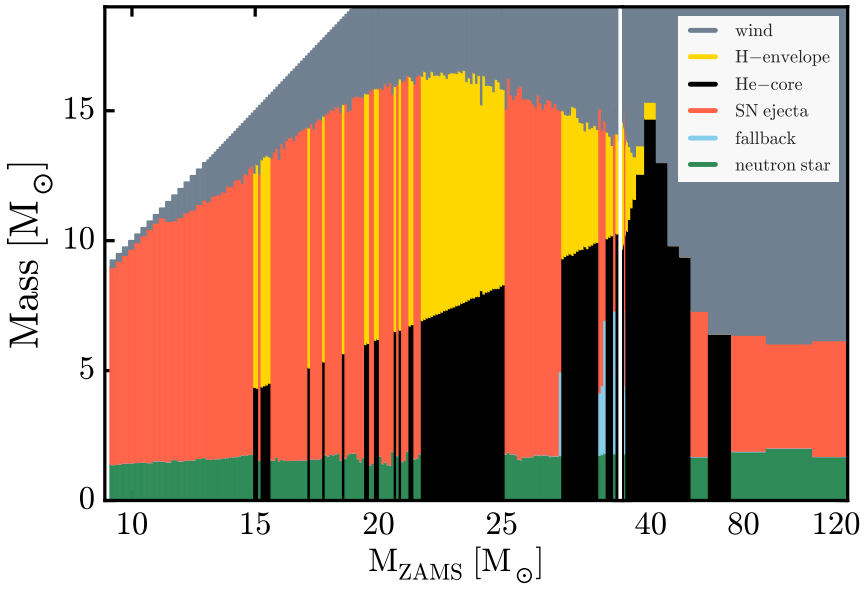

Figure 1.2 Mass budget of compact remnants as a function of the zero-age main-sequence mass of the progenitor star. The gray area shows the mass lost to the stellar wind. In the case of a supernova explosion, the green bars show the mass of the neutron star and the orange bars show the mass lost due to the supernova explosion. In the case of a failed supernova, the black hole retains the mass of the helium core, shown as black bars. In addition, the black hole may or may not retain the mass of the helium envelope, shown by the yellow bars. The blue bars show black holes formed by fallback. Reprinted from Sukhbold et al. (2016).

velocities and distances from the galactic disk of X-ray black holes (Repetto et al., 2012). However, due to the limited number of observations, it is not possible to confirm the existence of high natal kicks received by black holes at birth (Mandel, 2016).

GRO J1655-40 was found in a highly eccentric galactic orbit with a high runaway velocity (I. F. Mirabel; Mignani, et al., 2002). Israelian et al. (1999) found evidence of an overabundance of oxygen, magnesium, silicon, and sulfur in the atmosphere of the donor star, suggesting a supernova explosion with a portion of the ejecta captured by the companion star. An asymmetric supernova explosion combined with a black hole natal kick would explain the high peculiar velocity of the system (Willems et al., 2005). Similar evidence for an asymmetric supernova explosion and possibly a natal kick has been found for XTE J1118+480 (I. F. Mirabel; Dhawan, et al., 2001; González Hernández; Rebolo, et al., 2006; Gualandris et al., 2005; Fragos et al., 2009).

V404 Cyg has a peculiar velocity only 2 times higher than expected in its environment (Miller-Jones; Jonker; Nelemans, et al., 2009). A symmetric supernova explosion has been proposed to explain this velocity (Miller-Jones; Jonker; Dhawan, et al., 2009). This is further supported by evidence of enhanced oxygen abundances in the companion star (González Hernández; Casares, et al., 2011). Burdge et al. (2024) found a third component more than 3500 au away from the inner binary. This makes a strong natal kick very unlikely, as it would unbind the tertiary in the majority of configurations.

Cygnus X-1 is comoving with the Cygnus OB3 association of massive stars (Mel'nik; Dambis, 2009; Rao et al., 2020). It has been suggested that the black hole formed without a natal kick or mass loss in a supernova (I. Félix Mirabel; Rodrigues, 2003; Mark J. Reid et al., 2011). Furthermore, there is no observational evidence for supernova ejecta. All the evidence is consistent with the formation by direct collapse into a black hole. A similar case can be made for GRS 1915+105, which has a low peculiar velocity (M. J. Reid et al., 2014) consistent with no natal kick (Dhawan et al., 2007).

There is a lack of observed high-mass progenitors of red supergiants, the so-called RSG problem, which could be explained by the direct collapse of these stars into black holes. Theoretical models predict that red supergiants with masses in the range of $8\,M_\odot$–$25\,M_\odot$ should explode as Type IIP supernovae (Ekström et al., 2012). Using archival data, a deficit of progenitors was found above $16.5\,M_\odot$–$18.5\,M_\odot$. It has been proposed that these stars collapse into a black hole without a visible supernova (Smartt, 2015). However, the RSG problem could also be explained by an underestimation of absorption in the data used, or a higher than expected mass loss in the late stages of the red supergiant phase (Beasor; Davies, 2016).

Another indication that stars may collapse directly into a black hole is the disappearance of luminous massive stars without an optically bright supernova in nearby galaxies (Kochanek et al., 2008; Gerke et al., 2015). Some of these failed supernova candidates show faint infrared emission after their disappearance (Adams et al., 2016). This could be radiation from dust ejected by an outburst or accretion of the fallback onto a black hole (Adams et al., 2016).

Black holes formed by mergers

LIGO Scientific Collaboration et al. (2023) have studied the mass distribution of the individual components of mergers in the GWTC-3 catalog. It shows a monotonic decrease for the masses $> 50\,M_\odot$, which could indicate an upper mass limit. This could be explained by stellar models that predict a $\sim 50\,M_\odot$–$133\,M_\odot$ mass gap due to pair instability (Belczynski et al., 2016), but the evidence is inconclusive. In addition, they found peaks in the mass distribution around $10\,M_\odot$ and $35\,M_\odot$[2]. Another conclusion drawn by LIGO Scientific Collaboration et al. (2023) is that the merger rate increases with redshift. Whether the mass distribution depends on redshift cannot be determined from the available data.

The majority of massive stars are found in multiple stellar systems (Duchêne; Kraus, 2013; Sota et al., 2014). A black hole could accrete mass from a stellar companion, potentially increasing its mass into the pair instability gap. Son et al. (2020) used a population synthesis code to study the evolution of isolated binaries. They allowed for super-Eddington accretion during the common envelope and stable mass transfer phases of evolution. They suggest that a substantial population of systems with a black hole in the pair instability gap should form; however, the components are typically too far apart to merge within a Hubble time. They conclude that even under the most optimistic assumptions, their model predicts that only 2 % of merging binaries will contain a black hole in the pair instability mass gap. Moreover, only 0.5 % of the systems would contain

[2]The peak around $35\,M_\odot$ could also be just a transition to a decreasing merger rate.

a black hole larger than $90\,M_\odot$, none exceeding $100\,M_\odot$.

To circumvent the mass budget constraints imposed by the formation from a single star, one might consider hierarchical mergers. The individual high-mass components observed by gravitational waves could be products of previous mergers. Such mergers could play an important role in dense stellar environments such as globular clusters (Portegies Zwart; McMillan, 2002; Gültekin et al., 2006) or active galactic nuclei (McKernan et al., 2012; Bartos et al., 2017; Yang et al., 2019). Mass segregation in clusters could increase the merger rate by accumulating black holes in the cluster center.

Mergers of spinning black holes produce asymmetric gravitational wave emission, giving the merged black holes large kicks on the order of a few thousand $\mathrm{km\,s^{-1}}$ (González et al., 2007; Campanelli et al., 2007). Environments with high escape velocities, such as nuclear star clusters, would be required for hierarchical mergers if black holes form with high spins (Antonini; Rasio, 2016). Rodriguez et al. (2019) suggests that the merger rates in dense clusters are very sensitive to the initial spin of black holes formed from single stars. If black holes form with zero spin, hierarchical mergers could account for more than 10 % of mergers from clusters. On the other hand, if black holes form spinning, only 1 % of the detections from clusters would contain a component formed by a previous merger.

There is emerging evidence that the spin properties from the GWTC catalog change around $40\,M_\odot$–$50\,M_\odot$ (Pierra et al., 2024; Li et al., 2024; Antonini; Romero-Shaw, et al., 2025). This could suggest the existence of a low-mass population of black holes formed from single stars, with a high-mass population of black holes formed by hierarchical mergers populating the pair instability mass gap.

Doctor et al. (2020) modeled the collisions in a population of black holes using the effective cross section. They compared their results with the observations in the GWTC catalog and concluded that hierarchical mergers are disfavored. Kimball et al. (2020) also suggest that hierarchical mergers are unlikely in globular clusters.

Arca Sedda (2020) studied the formation and evolution of binary black holes in the vicinity of supermassive black holes. He showed that the Kozai–Lidov mechanism can greatly reduce the inspiral time and accelerate the mergers.

It is likely that a single formation model cannot explain the entire landscape of binary black hole observations (Zevin et al., 2021; Broekgaarden et al., 2022). Contributions from multiple formation pathways should be considered.

1.2 Interstellar bubbles

Massive stars lose significant mass by fast stellar winds (Sander; Vink, 2020) that interact with the surrounding interstellar medium and create two shock structures called interstellar bubbles. Additionally, they emit UV ionizing radiation which further modifies the ambient medium by creating an H II region. Interstellar bubbles are usually tens of parsecs in size and expand at a speed of several kilometers per second (Cappa et al., 2003). They encode the history of stellar wind and can provide key insights into stellar evolution. In addition, they play a significant role in regulating star formation.

1.2.1 Structure and evolution

Theoretical studies have extensively explored the structure and evolution of interstellar bubbles (Avedisova, 1972; Castor et al., 1975; Weaver et al., 1977; Koo; Christopher F. McKee, 1992; Toalá; Arthur, 2011; Geen; Rosdahl, et al., 2015; El-Badry; Ostriker, et al., 2019). A bubble can be described by a set of concentric shells as shown in figure 1.3. The innermost region consists of stellar wind escaping the star at thousands of $\mathrm{km\,s^{-1}}$. We call this the *free wind region*. At some point, the wind reaches the *reverse shock* (sometimes also called the *wind termination shock*). It loses most of its kinetic energy, which is converted into the thermal energy of the gas. The *shocked wind region* surrounds the free wind region and contains most of the thermalized stellar wind with temperatures of the order of $10^7\,\mathrm{K}$. The high pressure in the shocked wind region causes the bubble to expand, collecting gas from the interstellar medium in a *dense shell* at the edge of the bubble. The shell is separated from the shocked wind by a *contact discontinuity*. Both regions are in pressure equilibrium. A *shock front* separates the shell from the ambient interstellar medium. The ionizing UV radiation from the star can ionize part of the shell, creating an H II region between the shocked wind and the shell (Arthur, 2007; V. V. Dwarkadas; Rosenberg, 2013). If the interstellar medium is not homogeneous, the bubble may not be spherically symmetrical, but the general structure remains the same.

Massive stars start their life as O stars. During the main-sequence phase, they eject mass at thousands of $\mathrm{km\,s^{-1}}$ through radiation-driven winds. The mass-loss rate is usually below $10^{-5}\,\mathrm{M_\odot/yr}$ (Krtička et al., 2021). The structure of the resulting bubbles can be described by the classical model (Weaver et al., 1977). The ionization front is trapped inside the dense shell of the swept-up interstellar medium (Freyer et al., 2003).

Massive stars evolve into red supergiants. Solar metallicity stars with an initial mass exceeding $25\,\mathrm{M_\odot}$ end their lives in a Wolf–Rayet phase, but at lower metallicities stars must be more massive or do not even go through this phase. The most massive stars go through a luminous blue variable stage. During the red supergiant and luminous blue variable phases, the mass-loss rate is around $10^{-4}\,\mathrm{M_\odot/yr}$ (Nieuwenhuijzen; Jager, 1990), while the velocity of the wind decreases by an order of magnitude (Vink, 2018). Luminous blue variables can have a mass-loss rate of up to $10^{-3}\,\mathrm{M_\odot/yr}$ during their eruptive phase (Vink, 2012). This can lead to the formation of additional shells in the inner parts of the bubble (Garcia-Segura; Mac Low, et al., 1996; Garcia-Segura; Langer, et al., 1996). The ionization rate drops significantly.

During the Wolf–Rayet phase, the mass-loss rate decreases but can remain above $10^{-5}\,\mathrm{M_\odot/yr}$ while the velocity increases to thousands of $\mathrm{km\,s^{-1}}$ (Sander; Vink, 2020). An increased number of UV photons reionizes the surrounding gas. The fast wind can interact with the inner shell(s) and move the material further into the bubble. If there are multiple shells, the wind can make them collide and merge.

The size of the bubble is given by the main-sequence wind, even though most of the material comes from the red supergiant wind. The Wolf–Rayet wind plays a significant role in the mixing of the different phases.

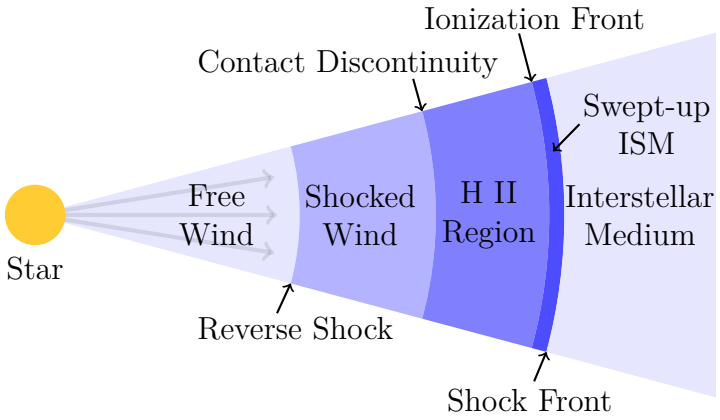

Figure 1.3 Schematic of the structure of an interstellar wind-blown bubble around a massive star.

1.2.2 Thermal conduction

The effects of thermal conduction on the structure and evolution of interstellar bubbles have been included in classical analytical and semi-analytical solutions (Cowie; C. F. McKee, 1977; Weaver et al., 1977), but they are often neglected even in recent studies.

Thermal conduction causes a heat flux from the shocked wind region into the cold dense shell of the swept-up interstellar medium. Due to energy conservation, this heat flux causes a mechanical energy flux in the opposite direction (Cowie; C. F. McKee, 1977). As a result, the gas from the shell evaporates into the shocked wind region, which loses thermal energy. The mass of the evaporated gas can be an order of magnitude greater than the mass of the stellar wind (Weaver et al., 1977).

Toalá and Arthur (2011) have done 1D and 2D simulations of interstellar bubbles including thermal conduction. They argue that thermal conduction is not important since it only slightly reduces the bubble size and changes the X-ray luminosity. Sharma et al. (2014) and Yadav et al. (2017) have included thermal conduction in simulations of superbubbles. They show that thermal conduction can lower the temperature in the shocked wind by more than an order of magnitude, smooth out the temperature and density gradients at the contact discontinuity, increasing the radiative cooling, and significantly increase the density and the total mass inside the bubble. Considering the above results, we argue that thermal conduction plays an important role and should not be neglected, especially if the models are used for comparison with observations.

Magnetic field can suppress thermal conduction in the direction perpendicular to the field lines (Balsara et al., 2008). Meyer, Mignone, et al. (2017) shows that even a modest magnetic field can suppress the effect of thermal conduction in interstellar bubbles. However, observational evidence is limited (Boroson et al., 1997; Chu; Martín A. Guerrero, et al., 2003), and it is not clear whether suppression of thermal conduction by magnetic fields plays a significant role.

1.2.3 Cooling

The radiative cooling rate is proportional to the density squared and a complex function of temperature and chemical composition (see section 2.3.3 for more details), which peaks around 10^5 K.

Cooling is very effective in the dense shell of the swept-up interstellar matter. As a result, the shell cools rapidly below 10^4 K and becomes very thin and dense. In addition, the gas passes through the peak of the cooling function at the interface of the shell with the hot shocked wind region, reducing the temperature and pressure inside the bubble. Thermal conduction increases radiative losses by smoothing out the gradients so that more of the gas has a temperature near the peak of the cooling function.

During the main-sequence phase of the stellar evolution, the fast wind injects a considerable amount of thermal energy into the bubble, and evaporation by thermal conduction dominates the cooling. However, in later stages, the amount of hot gas inside the bubble may decrease as thermal conduction becomes less important compared to cooling.

1.2.4 Observations

Interstellar bubbles produce a rich variety of observational signatures. Infrared observations can be used to trace dust heated by shocks. Optical emission lines and the radio continuum reveal regions of dense ionized gas. Neutral and molecular gas show up in the HI and CO lines. UV observations help probe gas ionized by stellar radiation and the properties of stellar wind. Meanwhile, hot, shocked gas emits X-rays.

Optical surveys have long been used to study ring nebulae around O and Wolf–Rayet stars (Lozinskaia, 1982; Chu; Treffers, et al., 1983; Marston et al., 1994), with observations in narrow-band filters such as Hα and OIII sensitive to dense ionized gas.

Bubbles with multiple concentric shells corresponding to stages of stellar evolution have been observed in both IR and radio (Marston, 1996). The outer shells, sometimes spanning hundreds of parsecs, are thought to be formed by the winds of O stars. The dense inner shells—visible in optical images—consist of slower red supergiant or luminous blue variable wind.

Radio observations have also been used to estimate the masses of ring nebulae. A number of shells around Wolf–Rayet stars were found to contain hundreds to thousands of solar masses of material (Cappa et al., 2003).

Churchwell et al. (2006) used infrared observations to identify over 300 rings around bubbles, many linked to OB stars. The Milky Way project (Simpson et al., 2012; Jayasinghe et al., 2019) leveraged the power of citizen science to identify more than 7500 IR bubbles. Toalá, M. A. Guerrero, et al. (2015) detected signatures of thermal IR emission from dust in thin shells in Wolf–Rayet nebulae.

Despite the high temperatures of gas in interstellar bubbles, exceeding millions of Kelvin, X-ray detection has proven elusive. X-ray luminosity scales with the square of the density, which is typically quite low. Many processes have been proposed that can reduce the energy inside the bubble or shorten the hot phase, including adiabatic expansion, thermal conduction, and turbulent mixing (Toalá; Arthur, 2011; Toalá; Arthur, 2018). X-rays were first detected in bubbles around

Wolf–Rayet stars (M. Wrigge et al., 1994; Matthias Wrigge et al., 2005; Zhekov, 2014) originating mostly from hot gas at $(1\text{–}2) \times 10^6$ K. To date, the only detection of X-rays in a bubble driven by a single main-sequence star has been made within the bow shock of ζ Ophiuchi (Toalá; Oskinova, et al., 2016; Green et al., 2022).

2 Model

2.1 Model overview

We present two models that focus on the interaction of a massive star ($M_* \geq 40 M_\odot$) with its surrounding medium. Both cases start with a young massive star in the center of a homogeneous spherical cloud. This star loses a significant amount of mass due to stellar wind. The interaction of the stellar wind with the surrounding ISM leads to the formation of an interstellar bubble. At the end of its life, the star may either explode as a core-collapse supernova, leaving behind a neutron star or a black hole as a remnant, or collapse directly into a black hole. We follow the evolution of the compact stellar remnant inside the bubble and calculate how much matter can be accreted onto it.

We will limit our study to single stars. A companion could significantly alter the evolutionary tracks of the star studied and even cause additional explosions. This could considerably alter the structure of the bubble.

SN inside a pre-blown bubble

In this case, the star explodes as a core-collapse supernova, forming a compact remnant. The supernova ejecta interact with the bubble in a complex way, creating a shock that propagates through the bubble. When this shock reaches an interface where the density changes, a transmitted and a reflected wave are created (Tenorio-Tagle; Bodenheimer, et al., 1990; Vikram V. Dwarkadas, 2005). Many waves undergoing numerous reflections and transmissions can interact with each other, depending on the structure of the bubble and the properties of the supernova ejecta.

Our goal is to model the interaction of the supernova ejecta with the pre-blown interstellar bubble and see if a portion of the supernova ejecta, stellar wind, or even the ISM could be accreted onto the compact stellar remnant.

Direct collapse and H II region accretion

In this case, the star ends its life by collapsing directly into a black hole without an explosion. Depending on the parameters of the star, an H II region can form between the hot interior and the shell of the bubble (Arthur, 2007; Geen; Koter, 2022). The H II region consists of gas at $T = 10^4\,\mathrm{K}$ with a density lower than that of the shell but much higher than that of the hot interior of the bubble. After the star dies, the H II region can cool to 100 K and begin to fall onto the interior of the bubble. Thermal conduction will transfer heat from the hot interior of the bubble to the former H II region, where the higher density will allow efficient radiative cooling. In this way, the hot interior of the bubble can cool to $10^4\,\mathrm{K}$ with denser parts cooling to 100 K. The cold dense gas can be effectively accreted onto the black hole.

Our goal is to model the evolution of the bubble after the star collapses into a black hole and see how much of the wind and ISM can be accreted onto the black hole.

2.2 Existing research

Tenorio-Tagle, Bodenheimer, et al. (1990) made numerical calculations of the evolution of supernova ejecta inside a wind-driven bubble. They assumed 1D spherical symmetry and neglected the effects of thermal conduction. The supernova explosion causes a shock that propagates through the bubble. This heats the interior of the bubble to $10^8\,\mathrm{K}$–$10^9\,\mathrm{K}$. When the shock reaches the shell of the bubble, a transmitted shock and a reflected shock are created. The reflected shock travels back through the hot wind. It may be reflected several times from the center of the simulation and the shell until the conditions inside the bubble are equalized. Tenorio-Tagle, Bodenheimer, et al. (1990) studied two different cases. If the mass of the shell is comparable to the mass of the supernova ejecta, the transmitted shock will propagate through the shell into the surrounding medium. If the mass of the shell is at least 50 times greater than the mass of the supernova ejecta, the transmitted shock will not be able to traverse the shell, but will only compress and accelerate it. Bubbles driven by the winds of massive stars can have shells that are significantly more massive than the supernova ejecta (Cappa et al., 2003); therefore, we are mostly interested in the second case, where the transmitted shock cannot escape the bubble.

Tenorio-Tagle, Rozyczka, et al. (1991) performed more sophisticated simulations in 2D. The general interaction of the supernova ejecta with the bubble remains the same as in 1D. In contrast to the 1D case, the mixing of wind and ejecta leads to a non-radial velocity field, which prevents multiple reflections of the reflected wave.

Rozyczka et al. (1993) consider a case with an off-center explosion inside a spherical bubble. They found that the shock hitting the parts of the shell closest to and furthest from the origin of the explosion is normal to the shell and therefore transfers more momentum and energy than the shock hitting the shell to the sides. This can result in barrel-shaped remnants.

Vikram V. Dwarkadas (2005) did 1D simulations similar to Tenorio-Tagle, Bodenheimer, et al. (1990), but with a steeper profile and a higher mass of the supernova ejecta. They found their results consistent with Tenorio-Tagle, Bodenheimer, et al. (1990) in the case where the shell mass is much larger than the ejecta mass. Vikram V. Dwarkadas (2007) studied in both 1D and 2D a more realistic case of a supernova explosion within a bubble formed by a $35\,\mathrm{M}_\odot$ star. They found that the bubble has multiple shells as a result of the changing wind parameters as the star evolves. The interaction of the supernova ejecta with these shells leads to a complex structure with many reflected and transmitted shocks. In 2D simulations, they found that the changing position of the reverse shock creates turbulence inside the bubble. This slows down the wind, which now has to find a way around the denser clumps, and also affects the shape of the inner shells caused by the wind from the red supergiant and Wolf–Rayet phases of the evolution. The turbulence inside the bubble makes the supernova ejecta aspherical. It takes longer for the supernova ejecta to reach the outer shell of the bubble than in the 1D case. In addition, the ejecta reaches different parts of the shell at different times. This causes the final structure to be significantly aspherical.

Haid et al. (2016) used an efficient 1D model to study supernova explosions in different types of interstellar media. They found that their results were comparable

to other, much more resolved, but also much more computationally expensive simulations.

Martínez-González et al. (2019) studied in 3D the collision of supernova ejecta with a pre-existing bubble formed by a $60\,M_\odot$ star. The mass of the shell was significantly higher than the mass of the supernova ejecta, so all of the ejecta were trapped inside the bubble. The paper focuses mostly on the destruction of pre-existing dust and dust in the ejecta. Their results are consistent with previous studies of the evolution of supernova remnants inside pre-blown bubbles. They also found that most of the dust in the supernova ejecta can survive. This means that core-collapse supernovae can be an efficient source of dust.

Meyer, Petrov, et al. (2020) performed 2D axisymmetric hydrodynamical simulations of supernovae that explode inside bubbles formed by massive stars that move at supersonic velocities relative to the interstellar medium. The motion of the star creates elongated asymmetric bubbles. The supernova interacting with such features can lead to structures similar to the Cygnus Loop.

From an observational point of view, several cases of supernovae interacting with a medium modified by a stellar wind have been observed. The Cygnus Loop is a supernova remnant with strong evidence of interaction with dense structures in the surrounding medium. Levenson et al. (1997) presented evidence that the supernova ejecta propagate inside the cavity of an interstellar bubble and interact with its dense shell. Borkowski et al. (1996) modeled the Cassiopeia A supernova remnant and showed that the supernova ejecta interact with a wind-blown bubble. Similar scenarios have been proposed for the N49 (Shull et al., 1985) and N132D (Hughes, 1987) supernova remnants.

2.3 Hydrodynamic model based on Flash code

We perform hydrodynamic simulations of the stellar wind bubble using the three-dimensional adaptive mesh refinement code Flash 4.6.2 (Fryxell et al., 2000). Flash is written in Fortran 90 and C, uses the Paramesh library (Olson et al., 1999), and is parallelized using the Message Passing Interface library (Message Passing Interface Forum, 2021). Flash uses a modified version of the piecewise parabolic method (Colella; Woodward, 1984) to solve the following hydrodynamic equations

$$\frac{\partial \rho}{\partial t} + \nabla \cdot \rho \boldsymbol{v} = q_\mathrm{m}\,, \tag{2.1}$$

$$\frac{\partial \rho \boldsymbol{v}}{\partial t} + \nabla \cdot \rho \boldsymbol{v}\boldsymbol{v} = \rho \boldsymbol{g} - \nabla P - q_\mathrm{m} \boldsymbol{v}\,, \tag{2.2}$$

$$\frac{\partial \rho E}{\partial t} + \nabla \cdot (\rho E + P) \boldsymbol{v} = \rho \boldsymbol{v} \cdot \boldsymbol{g} - Q + q_\mathrm{e} - \nabla \cdot \boldsymbol{q}_\mathrm{c}\,, \tag{2.3}$$

where t is the time, ρ, $\boldsymbol{v}$, and P are the fluid density, velocity, and pressure, respectively; $\boldsymbol{g}$ is the acceleration due to gravity, Q is the cooling rate, q_m is the mass deposition rate, q_e is the energy deposition rate, $\boldsymbol{q}_\mathrm{c}$ is the heat conduction flux, and E is the sum of internal and kinetic energy per unit mass defined as

$$E = \frac{P}{(\gamma - 1)\rho} + \frac{v^2}{2}\,, \tag{2.4}$$

where γ is the ratio of specific heats. The pressure is given by the ideal gas equation of state

$$P = \frac{k_\mathrm{B}\rho T}{\mu m_\mathrm{H}}\,, \tag{2.5}$$

where μm_H is the mean mass per particle, T is the temperature, and k_B is the Boltzmann constant. The chemical composition is calculated from the temperature of the gas. We consider gas with $T > 9700\,\mathrm{K}$ to be fully ionized, $9300\,\mathrm{K} > T > 700\,\mathrm{K}$ atomic, and $T < 300\,\mathrm{K}$ molecular. In the transitions between the intervals, we calculate μ by linear interpolation. For example, fully ionized gas with the chemical composition of the Sun has $\mu = 0.609$. The time step is calculated using the Courant–Friedrichs–Lewy condition (Courant et al., 1928).

2.3.1 Wind

Stellar winds are implemented by continuously inserting mass and thermal energy into the simulation. This leads to the formation of the wind, i.e. the conversion of thermal energy into kinetic energy on a scale comparable to the radius of the insertion sphere. The mass density profile follows the generalized Schuster profile (Ninkovic, 1998)

$$\rho_\mathrm{S}(r) = N\left(1 + \frac{r}{R_\mathrm{c}}\right)^{-\beta} \quad \text{for} \quad r < R_\mathrm{cut}\,, \tag{2.6}$$

where R_c is the core radius, R_cut is the cut-off radius (the radius of the insertion sphere), β is a constant, and N is a normalization constant calculated from the condition $\int_0^{R_\mathrm{c}} 4\pi r^2 \rho_\mathrm{S}(r) dr = 1$. We use $\beta = 1.5$ and $R_\mathrm{c} = R_\mathrm{cut}/3$. All of the mass and energy is inserted within the radius R_cut, which is always chosen to be at least the size of 9 cells in the simulation. This ensures that the profiles are resolved. The mass deposition rate follows

$$q_\mathrm{m}(r) = \rho_\mathrm{S}(r)\dot{m}_\mathrm{w}\,, \tag{2.7}$$

where $\dot{m}_\mathrm{w}$ is the mass-loss rate of the star. The energy deposition rate is given by

$$q_\mathrm{e}(r) = \rho_\mathrm{S}(r)L_\mathrm{w}\,, \tag{2.8}$$

where L_w is the power of the wind.

We used the Bonn Optimized Stellar Tracks (Szécsi et al., 2022) to follow the properties of the wind throughout the life of a star. The tracks include the star's effective temperature T_eff, radius R_*, mass M_*, and mass-loss rate $\dot{m}$. The power of the wind is calculated from

$$L_\mathrm{wind} = \frac{1}{2}\dot{m}v_\infty^2\,, \tag{2.9}$$

where v_∞ is the terminal velocity of the wind. If the star is on the main sequence, v_∞ is calculated from a relation by Krtička et al. (2021)

$$v_\infty = \frac{1}{2}\left[(v_+ - v_-)\frac{t}{1+|v|} + v_+ + v_-\right] v_\mathrm{esc} \quad \text{where} \quad t = \frac{T_\mathrm{eff} - T_0}{\Delta T}\,, \tag{2.10}$$

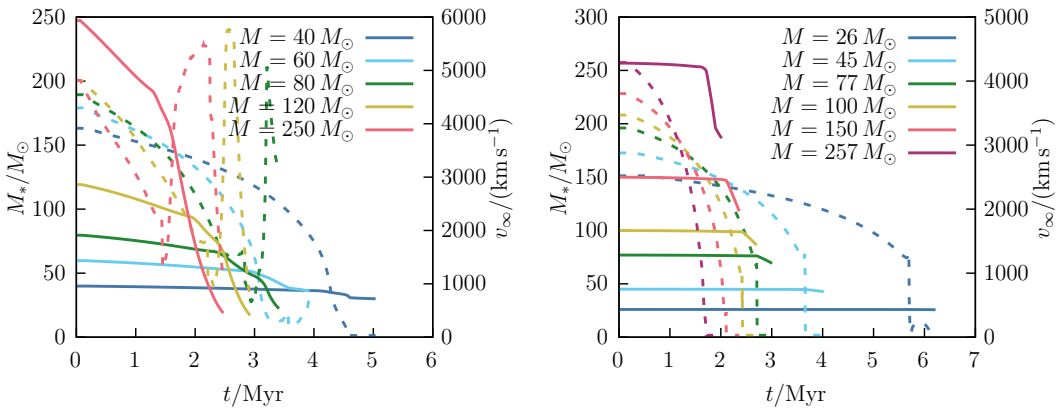

Figure 2.1 Mass of the stars M_* and terminal velocity of their wind v_∞ as a function of time calculated from the Bonn Optimized Stellar Tracks (Szécsi et al., 2022). Left panel shows stars with $Z = 0.66\,\mathrm{Z}_\odot$ and right panel stars with $Z = 0.016\,\mathrm{Z}_\odot$. M is the zero-age main sequence mass of a star.

$v_+ = 3.0$, $v_- = 0.7$, $T_0 = 20\,700\,\mathrm{K}$, $\Delta T = 3300\,\mathrm{K}$, and v_esc is the escape velocity calculated from the tracks as

$$v_\mathrm{esc}^2 = \frac{2GM_*}{R_*}\,, \tag{2.11}$$

where G is the gravitational constant. Equation 2.10 holds for Milky Way metallicity. To account for the different chemical compositions of the stars, we scale the terminal velocity as $v_\infty \propto Z^{0.13}$ (Leitherer et al., 1992), where Z is the metallicity of the star. In this work, we use two different chemical compositions of stars. The high-metallicity mean composition of the Milky Way and the low-metallicity composition of I Zwicky 18, which is thought to be a local equivalent of a primitive galaxy.

The terminal velocity of the wind is set to a constant value of $30\,\mathrm{km\,s^{-1}}$ for red supergiants (Airapetian et al., 2010) and $200\,\mathrm{km\,s^{-1}}$ for luminous blue variable stars (Vink, 2018). For Wolf–Rayet stars, we use a relation by Sander and Vink (2020)

$$\log\frac{\dot{m}}{v_\infty} = k\log[-\log(1-\Gamma_\mathrm{e})] + l\,, \tag{2.12}$$

where $k = 2.5$ and $l = -6.3$ are constants, and Γ_e is the Eddington factor, which describes the ratio of radiation pressure to the gravitational force and is given in the stellar evolution tracks.

The time evolution of the masses of the stars and the terminal velocities of their wind are shown in figure 2.1.

2.3.2 Supernova

Supernovae cause shock waves to propagate into the interstellar medium. A two-shock structure is formed, with a forward shock, a contact discontinuity, and a reverse shock. The envelope of the ejecta can be approximately described by a power-law profile $\rho \propto r^{-n}$. Initially, the mass of the ejecta is much greater than the mass of the swept-up ambient medium. The shock front and the contact discontinuity expand freely. The mass of the shell increases as the shock collects

the ambient medium. When the mass of the shell becomes significantly greater than the mass of the ejecta, the shock can no longer expand freely and follows the self-similar solution given by Taylor (1946) and Sedov (1959). In this work, we describe the initial supernova ejecta density profile as a power law with a flat core (Truelove; Christopher F. McKee, 1999; Tang; Chevalier, 2017).

In FLASH, the supernova explosion is achieved by inserting mass and kinetic energy into the simulation. We used the density and velocity profiles from Truelove and Christopher F. McKee (1999)

$$\rho_{\rm ej}(r,t) = \frac{M_{ej}}{R_{\rm ej}^3} f\left(\frac{r}{R_{\rm ej}}\right), \tag{2.13}$$

where $\rho_{\rm ej}$ is the density profile of the inserted gas. All mass and energy is inserted within the radius of the SN ejecta $R_{\rm ej}$. $M_{\rm ej}$ is the total mass of the SN ejecta, and f is a function of r defined as

$$f(r) = \begin{cases} f_0 & \text{for} \quad 0 \le r \le R_{\rm core} \\ f_0 (R_{\rm core}/r)^n & \text{for} \quad R_{\rm core} \le r \le R_{\rm ej}\,, \end{cases} \tag{2.14}$$

where f_0 is a constant, $R_{\rm core}$ is the core radius of the profile, and n is the steepness of the profile. We tried different values of n up to $n = 11$ without seeing any significant changes in the results of our simulations. We also tried simulations without the flat core ($R_{\rm core} = 0$) without seeing any differences. We used $R_{\rm core} = R_{\rm ej}/3$ and $n = 2$ for most of our simulations. We set $R_{\rm ej}$ to span at least 5 cells of the simulation to ensure that the profile is resolved.

Using equations 2.13 and 2.14 together with the condition that the total inserted mass is $M_{\rm ej}$, we obtain the normalized density profile

$$\rho_{\rm ej} = \begin{cases} \frac{M_{\rm ej}}{4\pi R_{\rm ej}^{3-n} R_{\rm core}^n} \frac{3-n}{1-\frac{n}{3}\left(\frac{R_{\rm core}}{R_{\rm ej}}\right)^{3-n}} & \text{for} \quad 0 \le r \le R_{\rm core} \\ \frac{M_{\rm ej}}{4\pi R_{\rm ej}^{3-n} r^n} \frac{3-n}{1-\frac{n}{3}\left(\frac{R_{\rm core}}{R_{\rm ej}}\right)^{3-n}} & \text{for} \quad R_{\rm core} \le r \le R_{\rm ej}\,. \end{cases} \tag{2.15}$$

The velocity profile of the SN ejecta is as follows

$$v_{\rm ej}(r) = \begin{cases} v_0 R_{\rm core} & \text{for} \quad 0 \le r \le R_{\rm core} \\ v_0 r & \text{for} \quad R_{\rm core} \le r \le R_{\rm ej}\,, \end{cases} \tag{2.16}$$

where v_0 is a normalization constant that can be calculated from the total kinetic energy of the ejecta $E_{\rm SN}$ as

$$v_0^2 = \frac{6 E_{\rm SN} R_{\rm ej}^{3-n} R_{\rm core}^{n-5}}{M_{\rm ej}} \frac{1 - \frac{n}{3}\left(\frac{R_{\rm core}}{R_{\rm ej}}\right)^{3-n}}{2 - n + 3\frac{R_{\rm core}^{n-5}}{R_{\rm ej}^{n-5}}} \frac{5-n}{3-n}\,. \tag{2.17}$$

2.3.3 Cooling

We consider the energy loss from gas due to electromagnetic radiation and assume that the gas is optically thin, so all of the energy is radiated away. We also assume that the number density of electrons and ions is equal and given by

$$n_\mathrm{i} = n_\mathrm{e} = \frac{\rho}{\mu_\mathrm{i} m_\mathrm{H}}\,, \tag{2.18}$$

where $\mu_\mathrm{i} m_\mathrm{H}$ is the mean mass per ion. For simplicity, the chemical composition of the gas is determined from its temperature. This is described in detail in section 2.3. The mean mass per ion is calculated from the chemical composition. For example, a fully ionized gas with solar chemical composition has $\mu_\mathrm{i} = 1.273$. For subsolar metallicities, μ_i is lower. The cooling rate is given by the equation

$$Q = n_\mathrm{H}^2 \frac{n_\mathrm{e}}{n_\mathrm{H}} \Lambda_N(T, Z)\,, \tag{2.19}$$

where n_H is the number density of hydrogen nuclei, Z is the metallicity of the gas, the electron to proton ratio $n_\mathrm{e}/n_\mathrm{H}$ is provided in the cooling table, and $\Lambda_N(T, Z)$ is the cooling function normalized to $n_\mathbf{e} n_\mathrm{H} V = 1\,\mathrm{cm}^{-3}$. The table provides element-by-element cooling rates assuming solar metallicity. For subsolar metallicities, we scale down each element's contribution to the total cooling rate proportionally to its reduced abundance. Figure 2.2 shows the cooling table calculated by Schure et al. (2009) for gas with $T \geq 15\,800\,\mathrm{K}$. We can see that the cooling function peaks around $10^5\,\mathrm{K}$. We use the cooling table by Dalgarno and McCray (1972) for $T \leq 10\,000\,\mathrm{K}$. For $10\,000\,\mathrm{K} < T < 15\,800\,\mathrm{K}$, we interpolate between the tables.

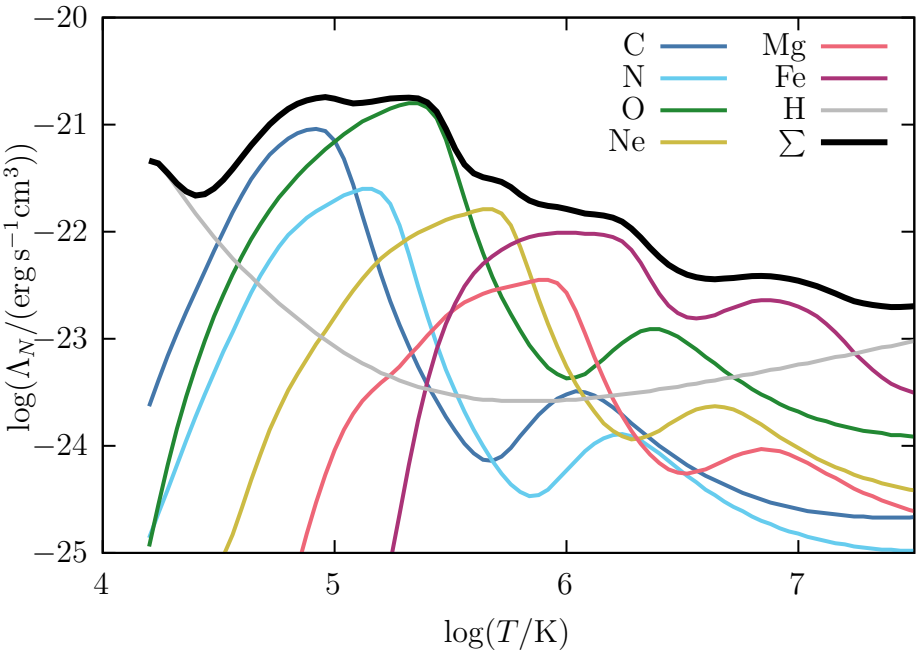

Figure 2.2 Cooling rate as a function of temperature given by Schure et al. (2009). Individual contributions from different elements are indicated by colored lines. The black line is the sum of all the contributions for solar metallicity.

2.3.4 Thermal conduction

When dealing with thermal conduction, we need to solve the following equation

$$\frac{\partial T}{\partial t} = -\nabla \cdot \mathbf{q}_{\mathrm{c}} = \nabla \cdot \kappa \nabla T \,, \tag{2.20}$$

where κ is the coefficient of conductivity. The coefficient for hydrogen plasma is given by Spitzer (1962)

$$\kappa \approx 4.5 \times 10^{13} \left(\frac{T}{10^8\,\mathrm{K}}\right)^{\frac{5}{2}} \left(\frac{\ln\Lambda}{40}\right)^{-1} \mathrm{erg\,s^{-1}cm^{-1}K^{-1}} \approx K T^{\frac{5}{2}} \,, \tag{2.21}$$

where $\ln\Lambda$ is the Coulomb logarithm. This is true only if the gas is ionized. At lower temperatures, conductivity is caused by neutral atomic collisions rather than electrons. Conductivity at lower temperatures does not play a significant role in our simulations, so we will only consider electron conductivity. The Coulomb logarithm is a weak function of density and temperature. We assumed $\ln\Lambda \approx 30$ to be constant, so $\kappa \approx K T^{\frac{5}{2}}$ where $K \approx 6 \times 10^{-7}\,\mathrm{erg\,s^{-1}cm^{-1}K^{-\frac{7}{2}}}$.

Equation 2.20 can overestimate the conduction flux if the temperature gradient is very steep (Campbell, 1984). The maximum energy that can be transported by the electrons is given by the saturated flux (Cowie; C. F. McKee, 1977; Balbus; C. F. McKee, 1982)

$$q_{\max} \approx \frac{3}{2} \rho c_{\mathrm{s,iso}}^3 \,, \tag{2.22}$$

where $c_{\mathrm{s,iso}} = \sqrt{k_{\mathrm{B}} T / (\mu m_{\mathrm{H}})}$ is the isothermal sound speed. To limit the flux, we replace the value of K with the effective value K_{eff}. To have a smooth transition between the saturated and normal modes, we use harmonic interpolation

$$\frac{1}{K_{\mathrm{eff}} T^{\frac{5}{2}}} = \frac{1}{K T^{\frac{5}{2}}} + \frac{\partial T}{\partial x} \frac{2}{3 \rho c_{\mathrm{s}}^3} \,. \tag{2.23}$$

Flash includes several diffusion solvers. The flux-based solver is an explicit solver. It requires time steps that are many orders of magnitude slower than the time steps required by the hydro solver to satisfy the Courant condition. Therefore, it is only useful for very low-resolution 1D simulations.

Flash also includes a general implicit solver[1]. This solver uses the hypre library (*hypre: High Performance Preconditioners*, [n.d.]; Falgout et al., 2006), is stable for longer time steps, but can be inaccurate. In this work, we used the implicit solver. In the case of thermal conduction, the solver advances the temperature using the following equation

$$\frac{T^{n+1} - T^n}{\delta t} = \theta \nabla \cdot \kappa^n \nabla T^{n+1} + (1-\theta) \nabla \cdot \kappa^n \nabla T^n \,, \tag{2.24}$$

where δt is the time step, θ determines the integration scheme, $^{n+1}$ means that a quantity is evaluated at the end of the time step and ^{n} means that it is evaluated at the beginning of the time step.

[1]The solver is not strictly implicit. The coefficients in the diffusion equation are evaluated only at the beginning of a time step, while the fluxes are evaluated at both the beginning and the end of the time step. This can lead to inaccurate results if the temperature and therefore the conductivity constant change significantly during a single time step.

There are three different schemes in this solver. There is an explicit forward scheme ($\theta = 0.0$) that uses only gradients at the beginning of each integration step. This scheme has the same limitations as the flux-based solver. There is the backward Euler scheme ($\theta = 1.0$), which uses only the gradients at the end of each integration step. Finally, there is the Crank–Nicholson scheme ($\theta = 0.5$), which uses the gradients at both the beginning and the end of the integration step.

The Crank–Nicholson method is second-order; it should preserve sharp features better than the first-order backward Euler method. However, the Crank–Nicholson method can overshoot with large time steps and cause oscillations. In our simulations, we did not find any significant differences in the results with backward Euler and Crank–Nicholson. We used backward Euler for all simulations because it was more stable compared to Crank–Nicholson.

2.3.5 Gravity

We consider two components contributing to the gravitational acceleration $g = g_{\rm ext} + g_{\rm self}$, an external potential causing $g_{\rm ext}$ and the self-gravity of the gas $g_{\rm self}$.

The gravitational field of the star or compact object is implemented as a prescribed gravitational potential

$$g_{\rm ext} = -\frac{GM}{r^2 + r_{\rm soft}^2}\,, \tag{2.25}$$

where M is the mass of the object and r is the distance from the object. We use the softening factor $r_{\rm soft}$ to prevent singular values of $g_{\rm ext}$ at $r = 0$. We set $r_{\rm soft} = 10^{-6} x_{\rm max}$, where $x_{\rm max}$ is the distance from the object to the edge of the computational domain.

In 1D spherically symmetric simulations, we use a simple spherical integrator (Kourniotis et al., 2023) to compute the mass of gas under a given cell contributing to self-gravity $g_{\rm self}$. Let us enumerate the cells in a 1D simulation using the index i such that $r_{i+1} > r_i$, where r_i is the distance from the center of the simulation to the i-th cell. The mass enclosed in a sphere with radius r_j is

$$M_j = \sum_{i=0}^{j} = \rho_i \Delta V_i\,, \tag{2.26}$$

where ρ_i is the density and ΔV_i is the volume of the i-th cell.

In 3D simulations, we use the parallel octal-tree based solver developed for Flash by Wünsch et al. (2018).

2.3.6 Accretion

The resolution of our simulations is much lower than what would be needed to resolve the accretion onto a stellar-mass black hole. Instead, we used a simple spherical accretion model to obtain an upper limit on the mass that could be transferred to an accretion disk and eventually accreted onto the black hole. The characteristic scale of the gravitational capture of gas is given by the Bondi radius

$$R_{\rm B} = \frac{2GM}{c_{\rm s}^2}\,, \tag{2.27}$$

where M is the mass of the accreting body. The gas flow transitions from subsonic outside the radius to supersonic inside the radius. $R_{\rm B}$ is usually smaller than the resolution of our simulations. The accretion rate is given by the formula

$$\dot{M} \approx \frac{4\pi\lambda(GM)^2\rho}{c_{\rm c}^3}\,, \tag{2.28}$$

where the constant $\lambda = 1/4$ for gas with $\gamma = 5/3$. During each time step in Flash, mass is removed from the center of the simulation and added to the mass of the black hole. The accretion rate is limited by the density of the gas ρ and the Bondi–Hoyle accretion rate $\dot{M}$.

In Flash we use mass scalars—tracer fields that are advected with the fluid—to trace the origin of the gas. This allows us to calculate how much of the accreted mass is from the ISM, the stellar wind, or the supernova ejecta.

2.3.7 Radiation transport

We assume that the star radiates as a black body with effective temperature $T_{\rm eff}$. The number of ionizing photons emitted by the star per second can be estimated from Planck's law

$$n_{\rm UV} = 4\pi R_*^2 \int_{\nu_{\rm min}}^{\infty} \frac{2\pi\nu^2}{c^2} \frac{1}{e^{\frac{h\nu}{k_{\rm B}T_{\rm eff}}} - 1} d\nu\,, \tag{2.29}$$

where R_* is the radius of the star, ν is the frequency of the radiation, h is the Planck's constant, and $\nu_{\rm min} = 13.6\,{\rm eV}/h \doteq 3.3\times10^{15}\,{\rm Hz}$ is the minimum frequency of ionizing photons. Figure 2.3 shows $n_{\rm UV}$ as a function of time for the stars used in this work.

We used a simple spherical integrator in 1D spherically symmetric simulations (Kourniotis et al., 2023) to calculate the ionization caused by UV photons. We assume that the photons created by recombination are immediately reabsorbed (on-the-spot approximation; Osterbrock, 1988). We define the attenuation of the ionizing radiation

$$\phi(r) = 1 - \int_0^r \frac{1}{n_{\rm UV}} \alpha_B n^2 4\pi r'^2 dr'\,, \tag{2.30}$$

where $\alpha_{\rm B} = 2.6\times10^{-13}\,{\rm cm^3 s^{-1}}$ is the recombination coefficient to the excited states, n is the number density of the gas, and r is the distance from the star. The ionization front is at $\phi = 0$. The temperature must not drop below $10^4\,{\rm K}$ when $\phi > 0$.

We neglect the effects of ionizing photons in 3D simulations; therefore, we only run 3D simulations after the star stops emitting a significant amount of UV photons. The first part of the wind bubble evolution is always calculated in 1D (with the ionizing radiation), and subsequently, the 3D simulation is initiated by remapping the 1D distribution of quantities onto the 3D Cartesian grid.

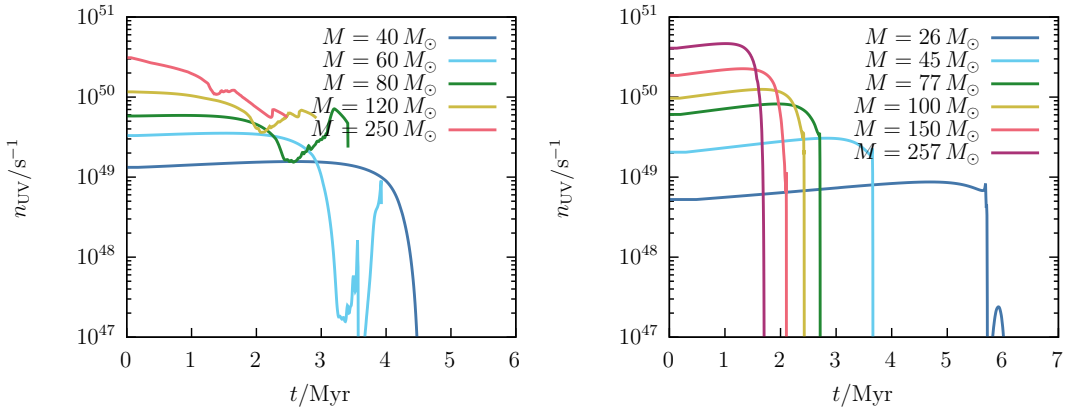

Figure 2.3 The number of ionizing photons n_{UV} emitted by a star per second as a function of time calculated from the Bonn Optimized Stellar Tracks (Szécsi et al., 2022) using equation 2.29. Left panel shows stars with $Z = 0.66\,\mathrm{Z}_\odot$ and right panel stars with $Z = 0.016\,\mathrm{Z}_\odot$. M is the zero-age main sequence mass of a star.

2.4 Simulation setup

In 1D, we simulate a spherically symmetric system using a uniform radial grid in spherical coordinates. We use reflecting boundary conditions at $r = 0$ and diode boundary conditions at the outer edge. In 3D, we use a Cartesian grid with diode boundary conditions. The reflecting condition maintains symmetry and ensures that no flux crosses through the center. The diode condition is a zero-gradient condition, which allows matter to leave the simulation domain but does not allow matter to enter. For thermal conduction, we use Neumann boundary conditions with $\mathbf{q}_{\mathrm{c}} \cdot \mathbf{n} = 0$, where $\mathbf{n}$ is a vector normal to the boundary and $\mathbf{q}_{\mathrm{c}}$ is the thermal flux. For gravity, we used isolated boundary conditions. This means that only the matter inside the domain contributes to the gravitational potential.

The initial conditions are a homogeneous cloud of a given mass with the particle density n_{ISM} and the pressure $p_{\mathrm{ISM}} = 1.3807 \times 10^{-13}\,\mathrm{Pa}$. A cloud with $n_{\mathrm{ISM}} = 100\,\mathrm{cm}^{-3}$ will have the temperature $T_{\mathrm{ISM}} = 100\,\mathrm{K}$. The ISM pressure is negligible compared to the pressure inside the bubble, and its exact value does not significantly affect the results. The pressure and density outside the cloud are 1000 times less than inside the cloud. There is no initial velocity.

Wind-driven interstellar bubbles inside homogeneous ISM are spherically symmetric, so we only do 1D simulations before the supernova explosion. This allows us to have a much higher resolution and better resolve the contact discontinuity. This is crucial to get the correct bubble parameters. After the supernova explosion, we either continue with a 1D simulation or use the 1D simulation as initial conditions for a 3D simulation. If the shell in the higher-resolution 1D simulation is too thin to be resolved in the lower-resolution 3D simulation, we increase the thickness of the shell to be at least 3 cells across, conserving its mass and energy.

2.5 The Hector code

We created the Hector (HEat Conduction correcTOR) code to better understand the effects of thermal conduction and cooling at contact discontinuities. Hector is able to find stationary 1D solutions of the hydrodynamic equations. We use Cartesian coordinates, which is possible if the bubble is large enough. Despite these approximations, Hector can give us useful insight into the processes that take place at the contact discontinuity, which significantly modify the energetics and mass of the bubble. The 1D stationary form of the hydrodynamic conservation laws can be expressed as

$$\frac{\partial}{\partial x}(\rho v) = 0\,, \tag{2.31}$$

$$\rho v \frac{dv}{dx} = -\frac{dp}{dx}\,, \tag{2.32}$$

$$\frac{\partial}{\partial x}\left(\rho v\left(\frac{1}{2}v^2 + \frac{5}{2}c_\mathrm{s}^2\right)\right) + \frac{\partial q_\mathrm{c}}{\partial x} + n^2\Lambda(T,Z) = 0\,, \tag{2.33}$$

where the pressure is given by the ideal gas equation of state

$$p = \frac{k_\mathrm{B}\rho T}{\mu m_H}\,, \tag{2.34}$$

c_s is the speed of sound defined as

$$c_\mathrm{s}^2 = \frac{\gamma k_\mathrm{B} T}{\mu m_H}\,, \tag{2.35}$$

and the thermal conduction flux is

$$q_\mathrm{c} = -K_\mathrm{eff} T^{\frac{5}{2}} \frac{dT}{dx}\,, \tag{2.36}$$

where K_eff is calculated in the same way as in section 2.3.4.

Equations 2.31–2.36 can be expressed as a system of four first-order partial differential equations

$$\frac{d\rho}{dx} = -\frac{\rho}{v}\frac{dv}{dx}\,, \tag{2.37}$$

$$\frac{dv}{dx} = \frac{k_\mathrm{B} v}{k_\mathrm{B} T - v^2 \mu m_H} U\,, \tag{2.38}$$

$$\frac{dT}{dx} = U\,, \tag{2.39}$$

$$\frac{dU}{dx} = \frac{\rho v}{K_\mathrm{eff} T^{\frac{5}{2}}}\left(\frac{k_\mathrm{B} v^2}{k_\mathrm{B} T - v^2 \mu m_H} + \frac{5\gamma k_\mathrm{B}}{2\mu m_H}\right) U - \frac{5}{2T}U^2 + \frac{n^2\Lambda(T,Z)}{K_\mathrm{eff} T^{\frac{5}{2}}}\,. \tag{2.40}$$

The coordinate x is defined so that $x = 0$ at the contact discontinuity and $x > 0$ inside the bubble. We solve equations 2.37–2.40 numerically. We start with the boundary conditions ρ_0, v_0, T_0, and U_0. These values are the conditions in the ionized part of the shell at $x = 0$. We assume that the pressure is constant throughout the hot gas region and the shell. From equation 2.31 we see that $\rho v = \rho_0 v_0$, that is, the mass flux must be constant in a stationary solution.

We numerically integrate from the contact discontinuity at $x = 0$ to the reverse shock at $x_{\mathrm{RS}} > 0$. Although the expected profiles of ρ, v, T, and U are smooth, we need very small spatial steps to obtain the correct solution. A system of such equations is called stiff. Certain numerical methods are unstable when applied to stiff equations. The gradients near the contact discontinuity are very steep. Even a small error in the calculation of the gradients can cause a significant difference in the values at the reverse shock. For example, the third- and fifth-order Runge–Kutta methods either overestimate or underestimate the temperature at the reverse shock.

The integration was implemented using the SciPy library (Virtanen et al., 2020). We used the explicit 8th-order Runge–Kutta method (DOP853 scheme; Hairer; Wanner; Nørsett, 1993), which uses a 5th-order method to estimate errors and to automatically set the integration step. This scheme is only suitable for non-stiff and mildly stiff problems. Nevertheless, we found it to be faster with the same accuracy compared to the implicit Runge–Kutta method of the Radau IIA family of order 5 (Hairer; Wanner, 1996) and an implicit method based on backward differentiation formulas with the order automatically varying between 1 and 5 (Byrne; Hindmarsh, 1975). Both of these implicit methods are suitable for highly stiff problems.

3 Results

3.1 Stationary solutions at contact discontinuity

To verify that the solutions given by the FLASH code are correct, we used the HECTOR code (described in more detail in section 2.5) to find detailed stationary 1D solutions of the hydrodynamic equations at contact discontinuities. Fixing the values of ρ_0, v_0, T_0, and U_0 in the shell fully determines a stationary solution in the shocked wind region, if such a solution exists. We expect the inner part of the shell to be ionized by the star, so we always use the value $T_0 = 10^4\,\mathrm{K}$. The temperature in the ionized part of the shell is constant, so we start the integration with $U_0 = \frac{dT}{dx}\Big|_{x=0} = 0$. Equation 2.31 implies that $\rho v = \text{const}$. By choosing a value of ρ_0 and v_0, we set the evaporation rate for the entire solution. The pressure in the shell and the hot gas are equal and constant.

Figure 3.1 shows solutions with different evaporation rates. The evaporation rate can be negative, which means that the hot wind loses mass by cooling faster than it gains mass by evaporation as a result of thermal conduction. For each value of ρ_0, there is a maximum and a minimum value of the evaporation rate, beyond which there is no stationary solution. Thermal flux can become saturated at high evaporation rates. This happens only at sufficiently high temperatures, usually further away from the shell.

Weaver et al. (1977) show that a similarity solution can be used in the hot region near the contact discontinuity when the conductive and mechanical energy fluxes dominate the energy losses. The temperature can be described by the power law

$$T \propto \left(\frac{x}{R_{\mathrm{CD}}}\right)^{\alpha}, \tag{3.1}$$

where R_{CD} is the radius of the contact discontinuity and $\alpha = 0.4$ is a constant. They calculate the cooling by integrating the cooling rate over the given temperature profile. Using HECTOR, we found that α is about 0.4 for the stationary solution with the highest temperature and evaporation rate in the hot region. For lower temperatures, we found profiles with values as low as $\alpha = 0.2$. The hotter solution is also steeper, the conductivity constant increases with temperature; therefore, the energy fluxes dominate the cooling losses and the solution is closer to the idealized one given by equation 3.1. Solutions with the highest and lowest possible temperatures sometimes do not fully follow the power law.

Care must be taken when comparing with fully spherical bubble simulations. HECTOR assumes 1D Cartesian geometry. This is a reasonable approximation near the contact discontinuity, but the solutions may differ closer to the reverse shock. Furthermore, HECTOR assumes that the solution is stationary and that the mass flux does not change with the distance from the contact discontinuity. In reality, the mass inside the hot region changes over time. Additionally, stellar wind carries mass through the reverse shock. Weaver et al. (1977) shows a sharp increase in temperature near the reverse shock compared to the profile given by equation 3.1. This feature is also present in the FLASH simulations.

Figure 3.2 shows a comparison of the temperature and density profiles calculated with FLASH and HECTOR. In FLASH, a bubble blown by a $60\,\mathrm{M}_\odot$ Milky Way

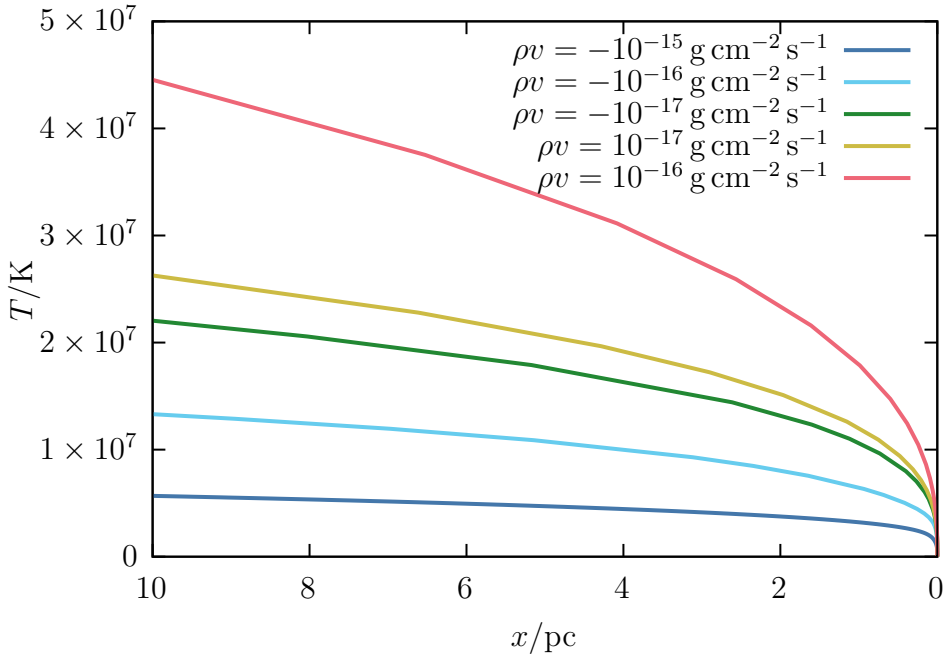

Figure 3.1 Temperature profiles of solutions for different evaporation rates ρv. All of the solutions have $\rho_0 = 5 \times 10^{-20}\,\mathrm{g\,cm^{-3}}$ and Milky Way metallicity of $Z = 0.66\,\mathrm{Z}_\odot$. The contact discontinuity is at $x = 0$.

metallicity star expanding into a cloud with $n_{\mathrm{ISM}} = 100\,\mathrm{cm^{-3}}$ was used. We chose a snapshot at 1.97 Myr, which is halfway through the life of the star. HECTOR is not capable of solving the evolution of the bubble over time. Instead, density in the H II region and temperature inside the hot region from the FLASH simulation were used as boundary conditions. Both profiles are similar until we get close to the reverse shock. The pressure is also the same in both solutions except for small sound waves in the FLASH simulation. We were unable to compare the evaporation rates because the bubble in FLASH expands with a velocity of orders of magnitude higher than the velocity caused by mass evaporation.

Figure 3.3 shows a detailed view of the temperature and cooling rate profiles near the contact discontinuity for the same case as in Figure 3.2. The cooling rate was calculated using equation 2.19. There are two visible peaks, first in the H II region as a result of the high density and a second around $T = 10^5\,\mathrm{K}$ due to the maximum in the cooling function (see figure 2.2). Individual cells in FLASH are shown using points. Despite the very high resolution of 6 mpc per cell, the cooling in FLASH is not fully resolved. This will be discussed in detail in section 3.2.1.

3.2 1D simulations of stellar wind bubbles

We performed 1D FLASH simulations of interstellar bubbles formed inside clouds with initial densities $n_{\mathrm{ISM}} \in [100, 1000]\,\mathrm{cm^{-3}}$. The cloud has a mass and radius defined by its second parameter, E_{grav}, its gravitational binding energy. We chose to parameterize the clouds in this way because E_{grav} is easily comparable to the energy of the supernova explosion and the total energy injected into the bubble by the stellar wind. Additional parameters of the simulations are the mass

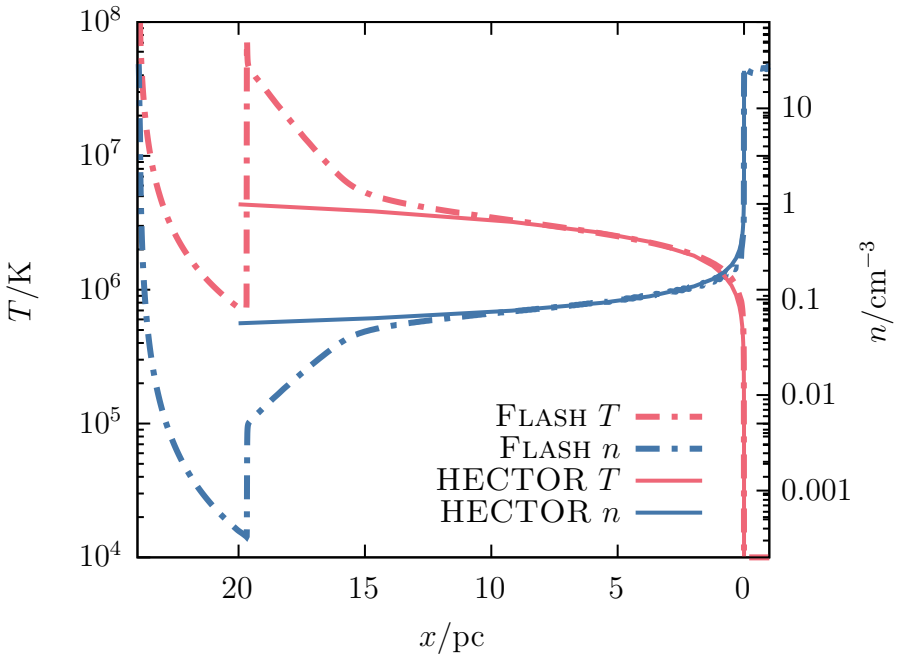

Figure 3.2 Comparison of temperature T and particle density n calculated using Flash and Hector.

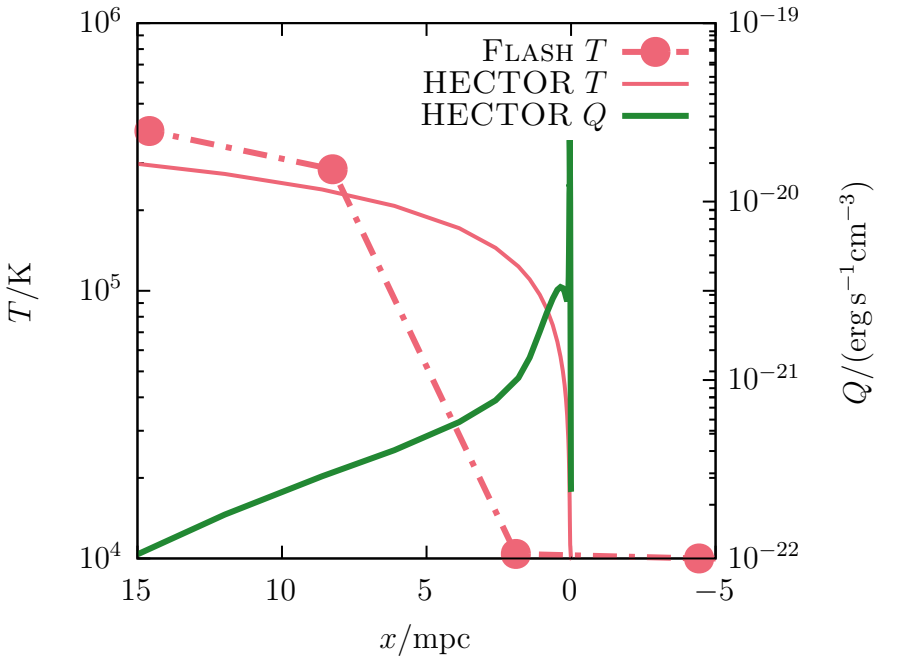

Figure 3.3 Detailed profiles of temperature T calculated using Flash and Hector at the contact discontinuity zoomed in 1000× compared to figure 3.2. Points in Flash solution represent values in the centers of individual cells. Radiative cooling rate Q was calculated using equation 2.19.

Table 3.1 Simulation parameters, ranges and number of values varied while keeping the other parameters fixed.

param.	description	range	# of vals.
n_{ISM}	particle density of the cloud	$10^2\,\mathrm{cm}^{-3}$–$10^3\,\mathrm{cm}^{-3}$	3–7
E_{grav}	grav. binding energy of the cloud	$10^{49}\,\mathrm{erg}$–$8\times10^{51}\,\mathrm{erg}$	3–9
M_*	ZAMS mass of the central star	$40\,\mathrm{M}_\odot$–$257\,\mathrm{M}_\odot$	5
Z	metallicity of the star and cloud	$0.016\,\mathrm{Z}_\odot$–$0.66\,\mathrm{Z}_\odot$	2

of the central star and the metallicity (of both the star and the cloud). If the densities were even lower, the bubble would usually be larger than 100 pc, making it difficult to follow its evolution in a simulation while resolving all its features. It would also place most of the material that could later be accreted onto black holes farther away, making the re-accretion less likely. If the mass of the cloud is too small, the bubble will be too large, regardless of the cloud density. The free fall time is proportional to $n_{\mathrm{ISM}}^{-0.5}$. A denser cloud will collapse faster. If the cloud is too dense or massive, the bubble will collapse within the lifetime of the star. The initial masses of clouds were in the range of $3\times10^4\,\mathrm{M}_\odot$–$3\times10^6\,\mathrm{M}_\odot$. Table 3.1 shows the complete list of the parameters explored.

Table 3.2 Properties of stars used in our simulations. A list of zero-age main-sequence masses M_* is given for each zero-age main-sequence metallicity Z_*.

$Z_*/Z_\odot$	$M_*/M_\odot$
0.66	40, 60, 80, 120, 250
0.016	45, 77, 100, 150, 257

We chose to run simulations for stars with zero-age main-sequence masses in the range of $M_* \in [40, 257]\,\mathrm{M}_\odot$. Less massive stars do not have enough mass loss due to a fast stellar wind to form significant bubbles. They are also less likely to form massive black holes. We decided to run our simulations for two different metallicities, as this affects the stellar evolution tracks used, the cooling function, and the equation of state. One set at $Z = 0.66\,\mathrm{Z}_\odot$ (Milky Way) and another at $Z = 0.016\,\mathrm{Z}_\odot$ (I Zwicky 18). Stars with lower metallicity experience less mass loss through their stellar wind, which is slower. They also have higher surface temperatures, resulting in more UV ionizing radiation. The complete list of all stars used in our simulations is in table 3.2.

3.2.1 Resolution study

In section 3.1 we show that the cooling rate changes rapidly at the interface of the hot gas with the H II region. Even in 1D, it would be very computationally expensive to fully resolve this in Flash. Figure 3.4 shows the mass of the hot gas ($T > 3.5\times10^5\,\mathrm{K}$, $p > 10^{-18}\,\mathrm{Pa}$) inside a bubble blown by a $60\,\mathrm{M}_\odot$ Milky Way metallicity star expanding into a cloud with $n_{\mathrm{ISM}} = 100\,\mathrm{cm}^{-3}$. The cooling is turned off for the first 0.5 Myr. This is done to prevent excessive cooling of the wind before the bubble develops. The right panel shows the mass as a function of time for different resolutions. We can see that the mass is underestimated at lower

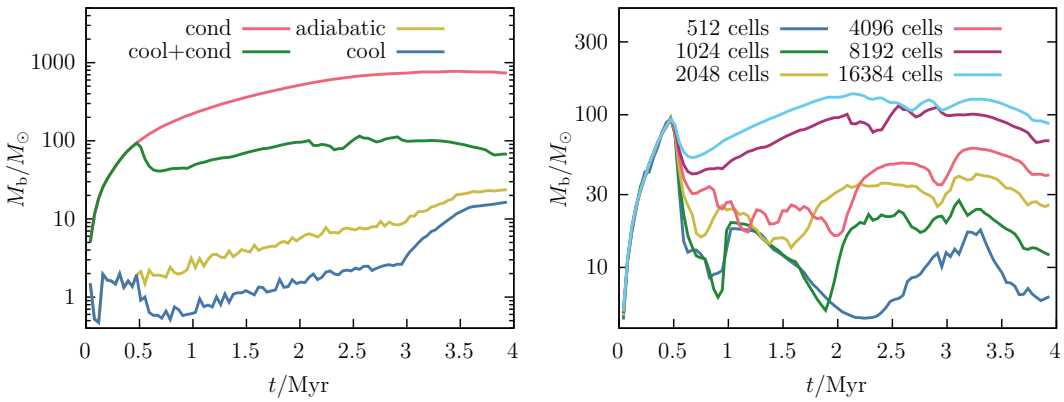

Figure 3.4 Mass of the hot ($T > 3.5 \times 10^5\,\mathrm{K}$, $p > 10^{-18}\,\mathrm{Pa}$) gas M_b inside a bubble as a function of time. Cooling is turned off for the first 0.5 Myr in all simulations. Left panel shows a comparison of simulations with 8192 cells with: thermal conduction only, radiative cooling and thermal conduction, no cooling or conduction, radiative cooling only. The right panel shows a comparison of simulations with thermal conduction and cooling at different resolutions.

resolutions. This is due to overcooling at the unresolved contact discontinuity. The cooling rate peaks in a region much smaller than the size of a cell in the simulation. When the gas density and temperature pass through the point of maximum cooling rate, the entire cell cools instead of just a small part of it, and this leads to the unphysically large cooling.

The left panel of figure 3.4 shows a comparison of simulations at the resolution of 8192 cells with: thermal conduction only, radiative cooling and thermal conduction, no cooling or conduction, radiative cooling only. Thermal conduction significantly increases the mass of the hot gas inside the bubble. Even though the highest resolution simulation is not fully converged and overestimates the cooling, the bubble still contains much more mass compared to the case with cooling but no thermal conduction. We argue that the correction due to thermal conduction is in the right direction at high resolution; therefore, we include thermal conduction in all of our simulations.

3.2.2 Black hole formation with direct collapse

Here we show the case of a star collapsing directly into a black hole without a supernova explosion. We have calculated 187 models differing in the following parameters: n_ISM, E_grav, Z (2 values–Milky Way and I Zwicky 18), and M_* (5 values per metallicity). For each metallicity, we describe in detail one less massive and one more massive star in order to cover all qualitatively different outcomes.

Milky Way metallicity

Figure 3.5 shows two snapshots from a simulation of a $120\,\mathrm{M}_\odot$ star evolving inside a cloud with initial particle density $n_\mathrm{ISM} = 100\,\mathrm{cm}^{-3}$ and mass $E_\mathrm{grav} = 2 \times 10^{51}$ erg. We find that stars with $M_* \gtrsim 80\,\mathrm{M}_\odot$ exhibit similar bubble structures and post-collapse behavior.

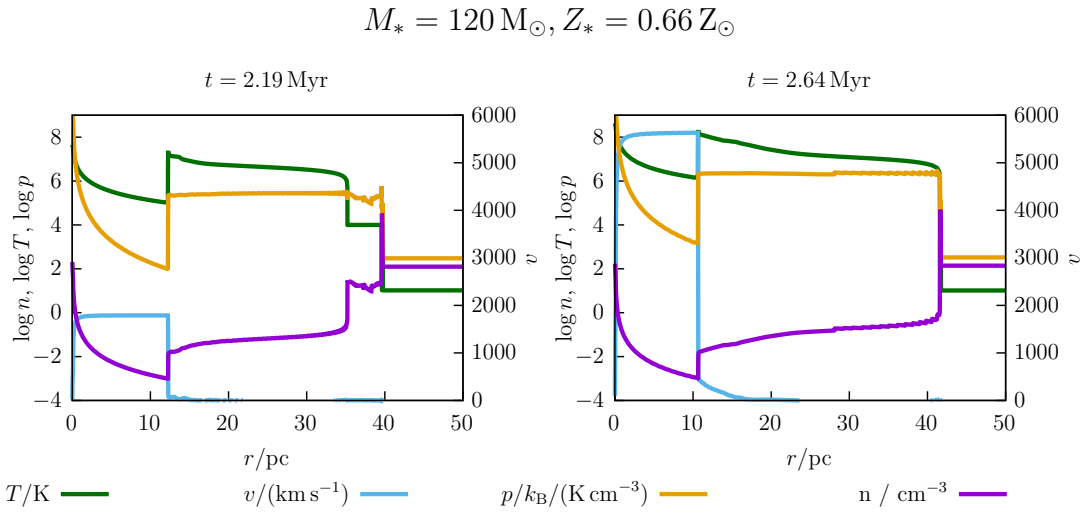

Figure 3.5 Profiles of temperature T, velocity v, pressure p, and particle density n of an interstellar bubble driven by stellar wind from a $120\,\mathrm{M}_\odot$ Milky Way metallicity star. The bubble expands into a cloud with $n_\mathrm{ISM} = 100\,\mathrm{cm}^{-3}$ and $E_\mathrm{grav} = 2 \times 10^{51}$ erg. The star collapses into a black hole after 2.93 Myr.

The left panel shows the bubble when the star is at the end of the main sequence. We can see a typical structure with a fast free wind region, a shocked wind region, an H II region, and a dense shell. The right panel shows the bubble near the end of the star's life as it goes through the Wolf–Rayet phase. The mass-loss rate increases over $10^{-4}\,\mathrm{M}_\odot$/yr and the velocity of the wind exceeds $5000\,\mathrm{km\,s}^{-1}$. The stellar wind injects considerable energy into the bubble and increases the pressure of the hot gas, which expands and compresses the HII region into a thin layer at the inner edge of the dense cold shell.

After the star undergoes direct collapse, the bubble contains only a low-density gas surrounded by the dense shell. The high pressure and low density of the bubble interior prevent efficient cooling and inhibit accretion onto the resulting black hole. We did not get any significant accretion in any of our simulations with more massive ($\gtrsim 80\,\mathrm{M}_\odot$) Milky Way metallicity stars.

If the initial mass of the star is $M_* \lesssim 60\,\mathrm{M}_\odot$, there is no phase of fast stellar wind near the end of the star's life, and the mass-loss rate is only of the order of $10^{-5}\,\mathrm{M}_\odot$/yr.

Figure 3.6 shows the evolution of a bubble blown by a $60\,\mathrm{M}_\odot$ star inside a cloud with $n_\mathrm{ISM} = 100\,\mathrm{cm}^{-3}$ and $E_\mathrm{grav} = 2 \times 10^{50}$ erg. The first panel shows the bubble near the end of the star's life. We can see a typical structure with two additional inner shells created by the slow wind of the late star. The hot region pushes the inner shells towards the center, they merge into a single dense shell and are accreted onto the black hole.

The second panel shows that the hot gas is cooling to $10^4\,\mathrm{K}$ and the much denser H II region is falling and moving closer to the black hole. In the third panel, the entire bubble has cooled to $10^4\,\mathrm{K}$. The density in the center is increasing, allowing the gas to cool even further. A portion of the material falling onto the black hole is reflected from the center; a wave propagating away is created and reflected back from the dense shell of the bubble. The waves propagate back and

$$M_* = 60\,\mathrm{M}_\odot, Z_* = 0.66\,\mathrm{Z}_\odot$$

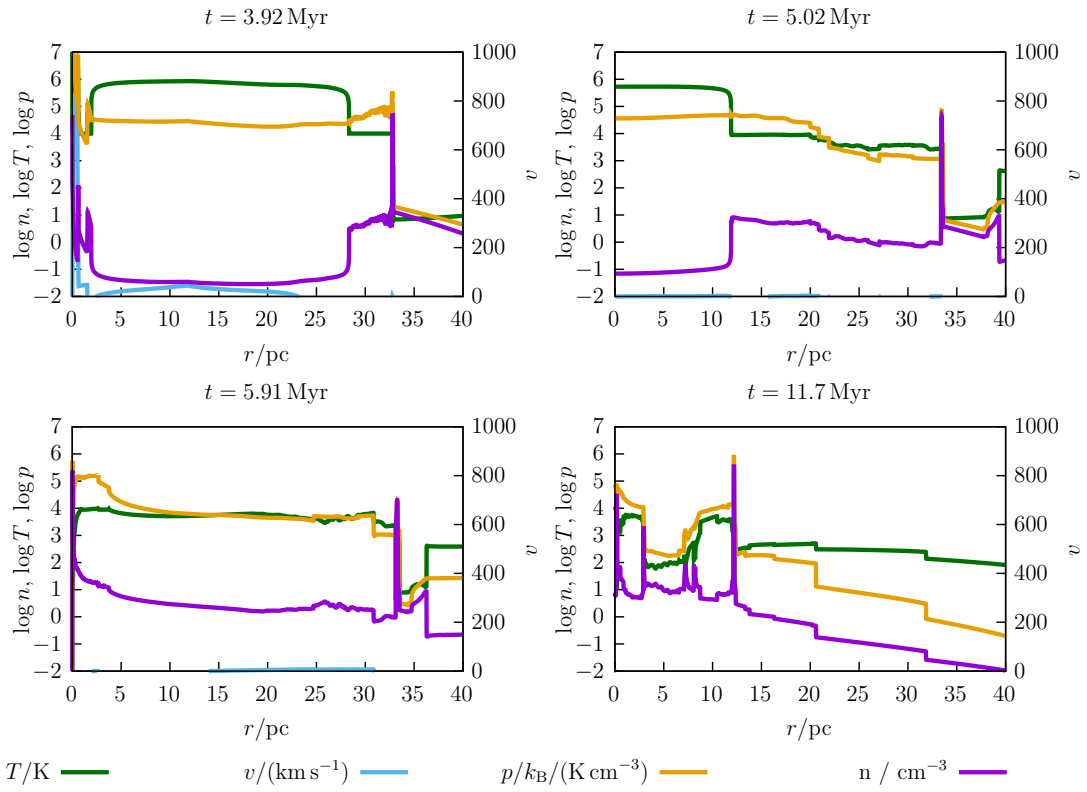

Figure 3.6 Profiles of temperature T, velocity v, pressure p, and particle density n of an interstellar bubble driven by stellar wind from a $60\,\mathrm{M}_\odot$ Milky Way metallicity star. The bubble expands into a cloud with $n_\mathrm{ISM} = 100\,\mathrm{cm}^{-3}$ and $E_\mathrm{grav} = 2 \times 10^{50}$ erg. The star collapses into a black hole after 3.94 Myr.

forth through the bubble multiple times. Most of the accretion occurs in short bursts when a density wave reaches the center of the simulation.

The last panel shows the bubble before it collapses completely. About $9\,\mathrm{M}_\odot$ of the gas have been accreted onto the black hole, the rest being collected by the falling shell. However, the shell is outside the scope of our simulations, since it is dense enough to form stars. We cannot say whether there is any gas left in the falling shell that could be accreted onto the black hole.

Low metallicity

Lowering the stellar metallicity from Milky Way values to those typical of I Zwicky 18 has a significant impact on stellar evolution and wind properties. Main-sequence low-metallicity stars have a lower mass-loss rate due to the stellar wind, which is also slower. They have higher surface temperatures and emit more ionizing photons. Since they lose significantly less mass to the radiation-driven wind, they remain much more massive during the late evolutionary stages (mostly red supergiants), even though slow-wind mass-loss rates are much higher.

Figure 3.7 shows the case of a $150\,\mathrm{M}_\odot$ star inside a cloud with $n_\mathrm{ISM} = 100\,\mathrm{cm}^{-3}$ and $E_\mathrm{grav} = 4 \times 10^{50}$ erg. The first panel shows the bubble when the star is near the

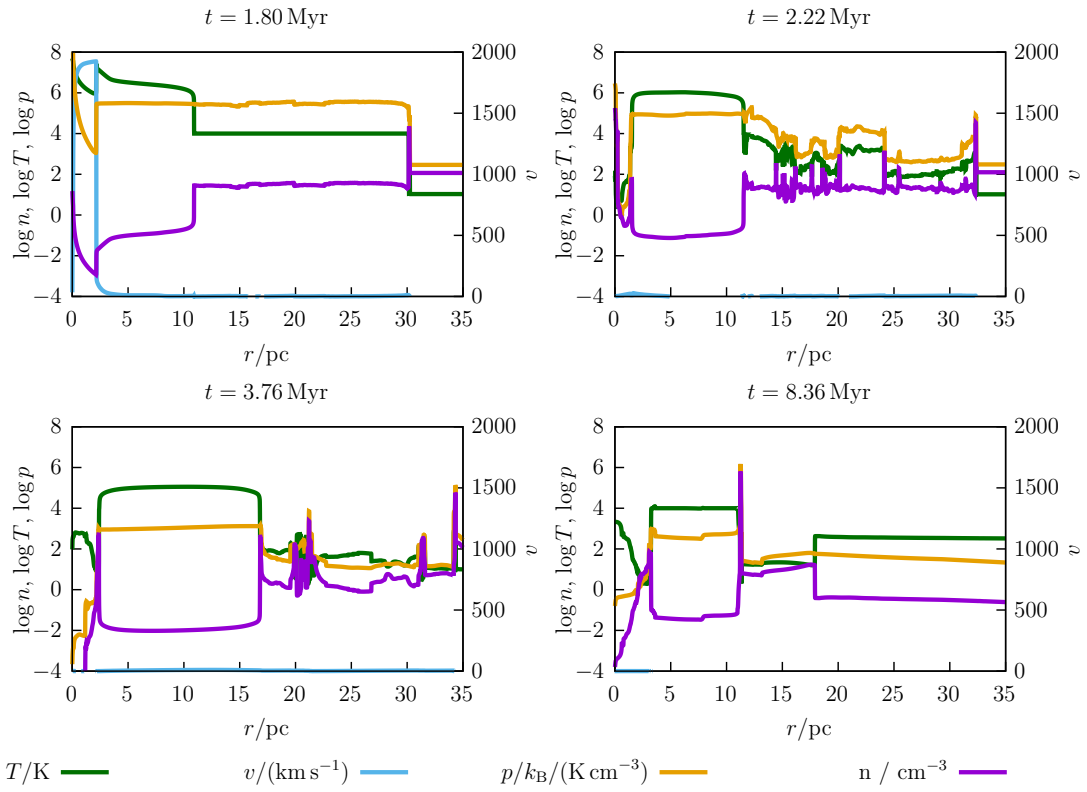

Figure 3.7 Profiles of temperature T, velocity v, pressure p, and particle density n of an interstellar bubble driven by stellar wind from a $150\,\mathrm{M}_\odot$ star with the metallicity of I Zwicky 18. The bubble expands into a cloud with $n_\mathrm{ISM} = 100\,\mathrm{cm^{-3}}$ and $E_\mathrm{grav} = 4 \times 10^{50}\,\mathrm{erg}$. The star collapses into a black hole after 2.36 Myr.

end of its main sequence phase. Compared to the $120\,\mathrm{M}_\odot$ Milky Way metallicity star in figure 3.5, there is a larger H II region due to the increased ionizing radiation; however, the hot region of the bubble is smaller, as a result of the weaker stellar wind.

The second panel shows the bubble near the end of the star's life. The wind is slow, but with a significant mass-loss rate exceeding $10^{-4}\,\mathrm{M}_\odot/\mathrm{yr}$. The late wind creates a dense inner shell that slowly moves away from the star. The amount of ionizing radiation from the star is greatly reduced, and the H II region begins to cool below $10^4\,\mathrm{K}$.

The third panel shows the bubble 400 kyr after the star has collapsed into a black hole. The inner shell has enough mass to not be stopped by the high pressure of the hot region supporting the former H II region. The last panel shows that even 5 Myr after the star has collapsed into the black hole, the bubble is still supported by the inner shell, preventing any material from falling towards the black hole and being accreted. This happens in all cases of stars with initial masses $M_* \gtrsim 77\,\mathrm{M}_\odot$ and the metallicity of I Zwicky 18.

In the case of a low-mass, low-metallicity star, the evolution of the bubble is

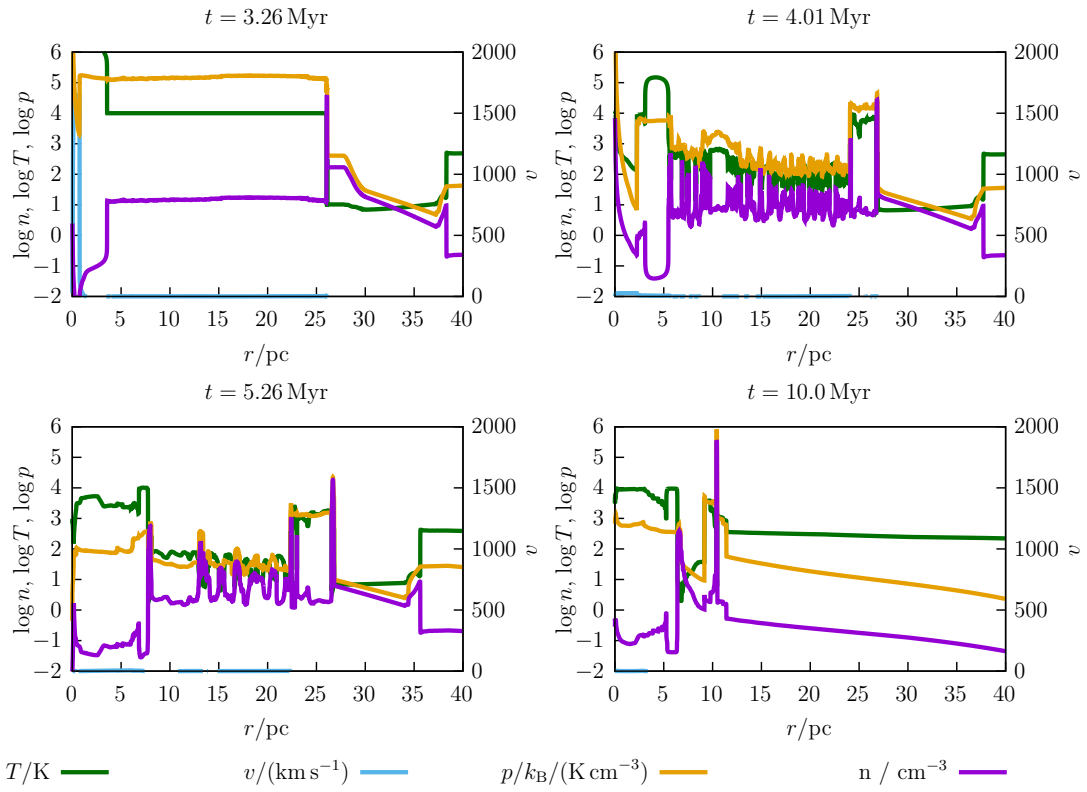

Figure 3.8 Profiles of temperature T, velocity v, pressure p, and particle density n of an interstellar bubble driven by stellar wind from a $45\,\mathrm{M}_\odot$ star with the metallicity of I Zwicky 18. The bubble expands into a cloud with $n_\mathrm{ISM} = 100\,\mathrm{cm}^{-3}$ and $E_\mathrm{grav} = 10^{50}\,\mathrm{erg}$. The star collapses into a black hole after 4.02 Myr.

similar to that of the higher-mass star. The star has a lower mass-loss rate that does not exceed $10^{-5}\,\mathrm{M}_\odot/\mathrm{yr}$. Figure 3.8 shows a $45\,\mathrm{M}_\odot$ star inside a cloud with $n_\mathrm{ISM} = 100\,\mathrm{cm}^{-3}$ and $E_\mathrm{grav} = 10^{50}\,\mathrm{erg}$. The first two panels are similar to the case in figure 3.7.

In the third panel, we can see that the inner shell is much less massive and its temperature stays around $10^4\,\mathrm{K}$. The pressure in the warm gas is too high for any significant accretion onto the black hole. The last panel shows that the gas does not cool even 6 Myr after the star has collapsed into a black hole.

Bubble properties

Another result of our simulations, in addition to the accreted mass, is a set of bubble properties. In this section, we describe the trends that we observed in the properties of interstellar bubbles.

Two competing processes govern the structure of the bubbles. On the one hand, radiative cooling reduces the amount of mass and energy within a bubble: a more massive or denser cloud leads to a smaller, denser bubble that cools much more effectively. On the other hand, a denser bubble has a higher internal energy and

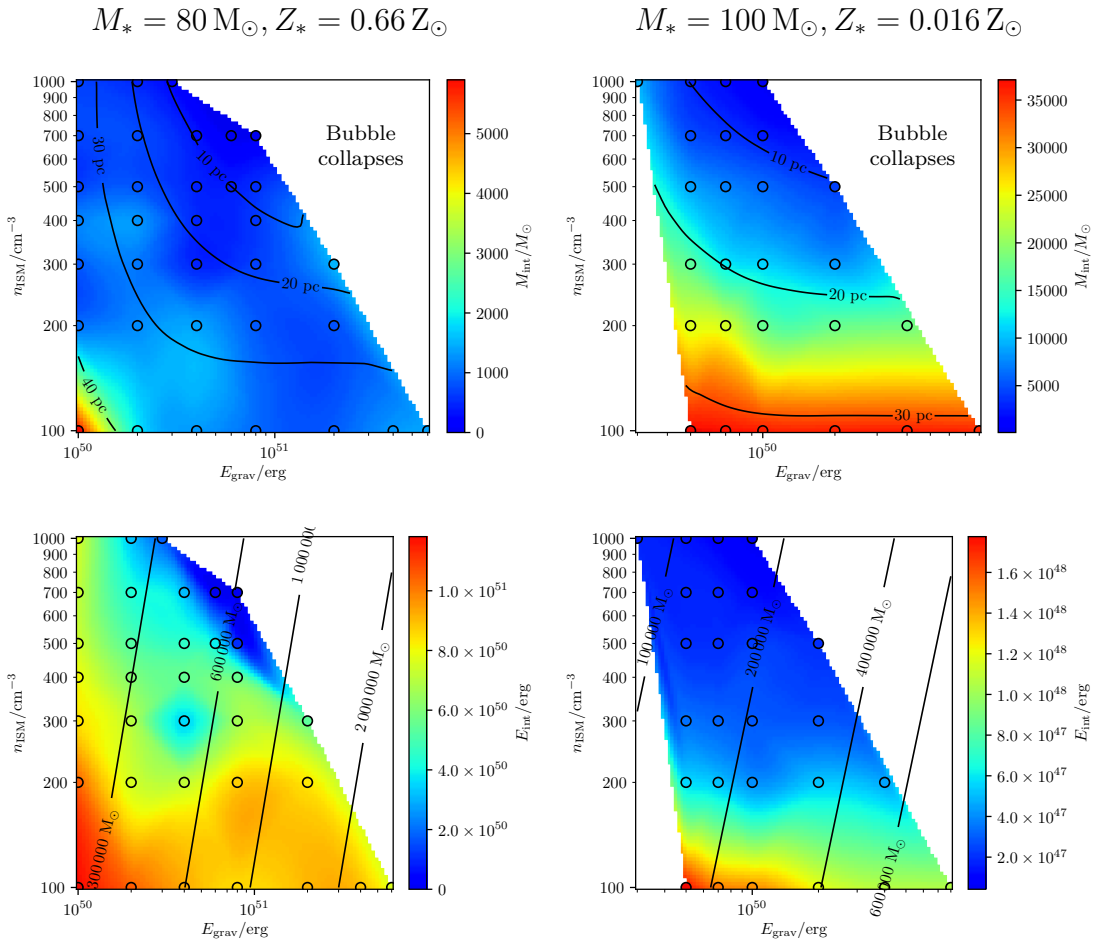

Figure 3.9 Properties of the bubble 50 kyr after the star collapses into a black hole as a function of the gravitational energy of the initial cloud E_{grav} and the initial particle density of the cloud n_{ISM}. The top panels show the mass M_{int} of the gas under the dense shell. The bottom panels show the internal energy E_{int} of all the gas under the shell at the same time as the top panels. Contours show the radius of the shell and the mass of the initial cloud. The left column shows a $80\,\mathrm{M}_\odot$ Milky Way metallicity star, the right column shows a $100\,\mathrm{M}_\odot$ star with the metallicity of I Zwicky 18. Black circles show individual simulations. Color maps and contours were calculated using cubic interpolation in logarithmic space from the individual simulations.

pressure, which allows for a higher evaporation rate because of thermal conduction, thereby increasing the mass inside the bubble.

The top panels in figure 3.9 show the mass M_{int} of the gas inside a bubble interior (under the dense shell) 50 kyr after the star undergoes direct collapse. We do not measure the mass immediately after the star collapses to let the final stages of the wind interact with the bubble. In the case of the Milky Way metallicity star, the H II region is small with relatively low mass. The pressure of the gas inside the bubble pushes the gas from the former H II region into the shell at the end of the star's life, significantly reducing the mass under the shell. However, if the initial cloud has a low density and a low mass, the bubble is large with low pressure, and the gas from the former H II region is not pushed into the shell.

This leads to a much higher mass under the shell in comparison with the other cases and can be seen in the bottom left corner of the top left panel. In the case of the low-metallicity star, the bubble retains a significant amount of mass from the (former) H II region created by the ionizing radiation from the star; therefore, the mass inside the bubble is much larger compared to the high-metallicity case.

The bottom panels in figure 3.9 show the internal energy $E_{\rm int}$ of the bubble interior at the same time as the top panels. When the initial mass of the cloud or its density increases, the bubble becomes smaller and denser, making radiative cooling much more effective; therefore, the internal energy decreases. However, in a handful of cases, the energy can also grow with increasing initial mass and density of the cloud. This may be because the smaller bubble does less work by not expanding as far into the ambient medium.

The clouds in the white areas in the top right corners of the plots are too massive, and the bubble collapses during the lifetime of the star. The white areas in the bottom left corner of the second column are the cases where the gravitational energy of the initial cloud is small compared to the energy injected by the stellar wind. The bubble continues to expand rapidly, reaching radii too large for accretion because of the low density inside the bubble. In addition, the growing size of the bubble makes it difficult to resolve all its features over the entire evolution with a fixed Eulerian grid.

The size of the bubble is shown using contours which approximately follow both the distribution of the mass and the internal energy of the bubble interior. This indicates that the first of the two competing processes considered above dominates. The plots for other stars (see section 3.2 for the full range of explored parameters) are qualitatively the same.

3.2.3 Black hole formation with supernova

In this section, we investigate the case with the massive star ending its life with a supernova explosion. We calculated most of the cases with a supernova that ejects $M_{\rm ej} = 5.58\,{\rm M}_\odot$ with the energy of $E_{\rm ej} = 9.12 \times 10^{50}\,{\rm erg}$. We also explored simulations with $E_{\rm ej} = 5 \times 10^{50}\,{\rm erg}$ that correspond to a case in which the material cools shortly after ejection. In addition, we conducted a small number of simulations with $M_{\rm ej} = 10\,{\rm M}_\odot$, $M_{\rm ej} = 15\,{\rm M}_\odot$, $E_{\rm ej} = 9.12 \times 10^{50}\,{\rm erg}$, and $E_{\rm ej} = 10^{52}\,{\rm erg}$. We found that the exact parameters of the supernova do not significantly alter the outcome.

We have calculated 276 models differing in the following parameters: $n_{\rm ISM}$, $E_{\rm grav}$, Z (2 values–Milky Way and I Zwicky 18), and M_* (5 values per metallicity). We illustrate the evolution after the supernova explosion by showing the example of a bubble created by the wind of a $77\,{\rm M}_\odot$ star with the metallicity of I Zwicky 18. The bubble was created inside a cloud with $n_{\rm ISM} = 100\,{\rm cm}^{-3}$ and $E_{\rm grav} = 10^{50}\,{\rm erg}$. The star explodes as a supernova after 3 Myr. This is one of the more optimistic cases for accretion. The low-metallicity star emits a large number of UV photons, creating a vast H II region between the hot gas and the dense shell of the swept-up ISM. The H II region is much denser than the hot gas and less than 10 pc far from the star at the end of the star's life. However, the results are qualitatively the same for the whole range of bubble and star parameters described in section 3.2.

Figure 3.10 shows gas profiles inside the bubble after the supernova explosion.

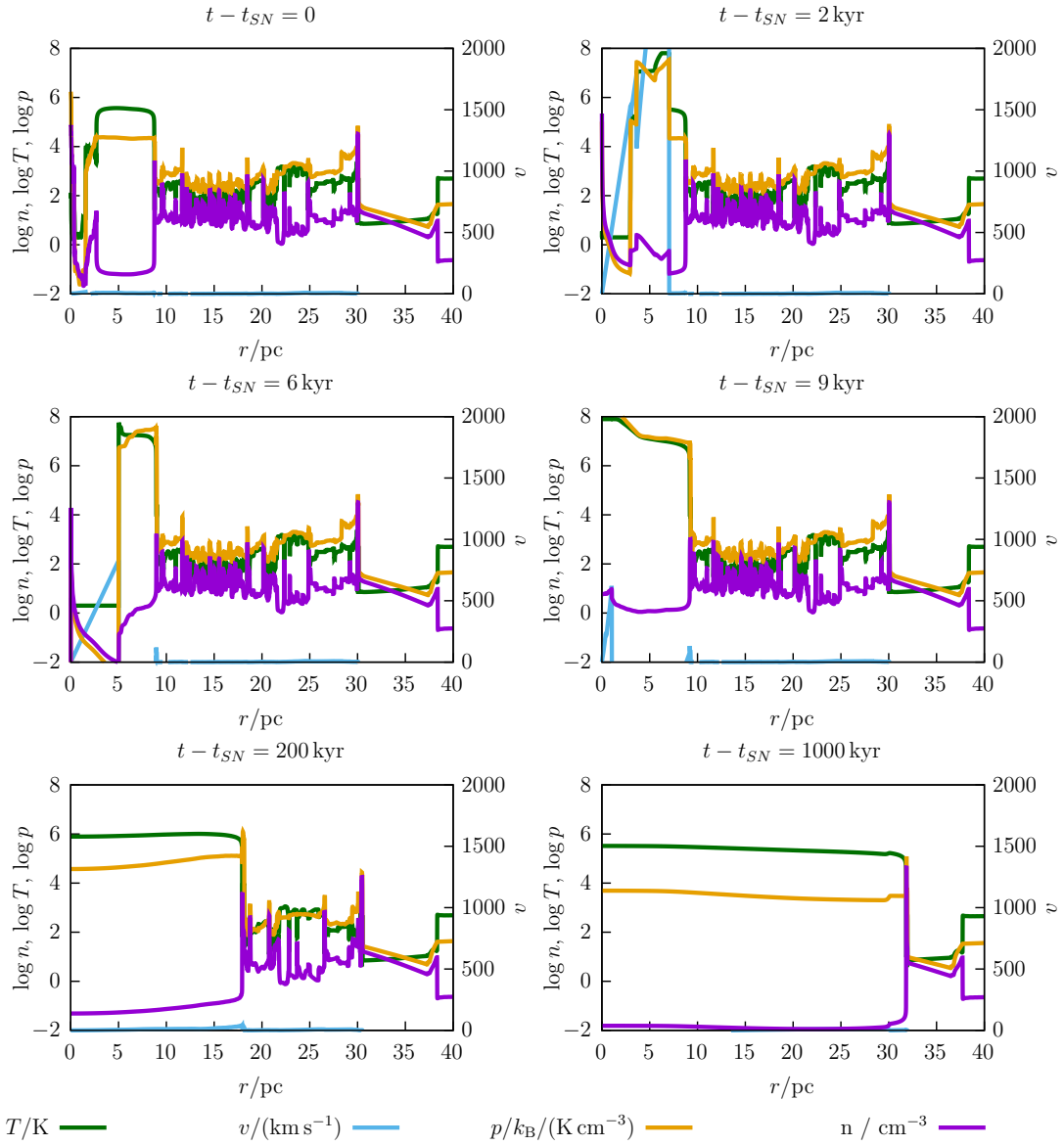

Figure 3.10 Profiles of temperature T, velocity v, pressure p, and particle density n after a supernova explodes inside an interstellar bubble. The bubble formed due to the wind from a $77\,\mathrm{M}_\odot$ star with the metallicity of I Zwicky 18 inside a cloud with $n_\mathrm{ISM} = 100\,\mathrm{cm}^{-3}$ and $E_\mathrm{grav} = 10^{50}\,\mathrm{erg}$.

The first panel depicts the bubble just before the insertion of the supernova ejecta. The H II region has already cooled. There is a small inner shell created by the slow wind during the final stages of the star's evolution. The second panel shows the shock wave from the supernova explosion propagating through the bubble interior. The shock wave interacts with the inner shell but mostly goes through. When the ejecta reaches the edge of the former H II region, two waves are created. A reflected wave can be seen in the third panel going back towards the black hole. A second, transmitted wave slowly goes through the former H II region, collecting all of its material. When the reflected wave gets to the center, its density is too low to cool efficiently. The pressure around the black holes is high and the wave

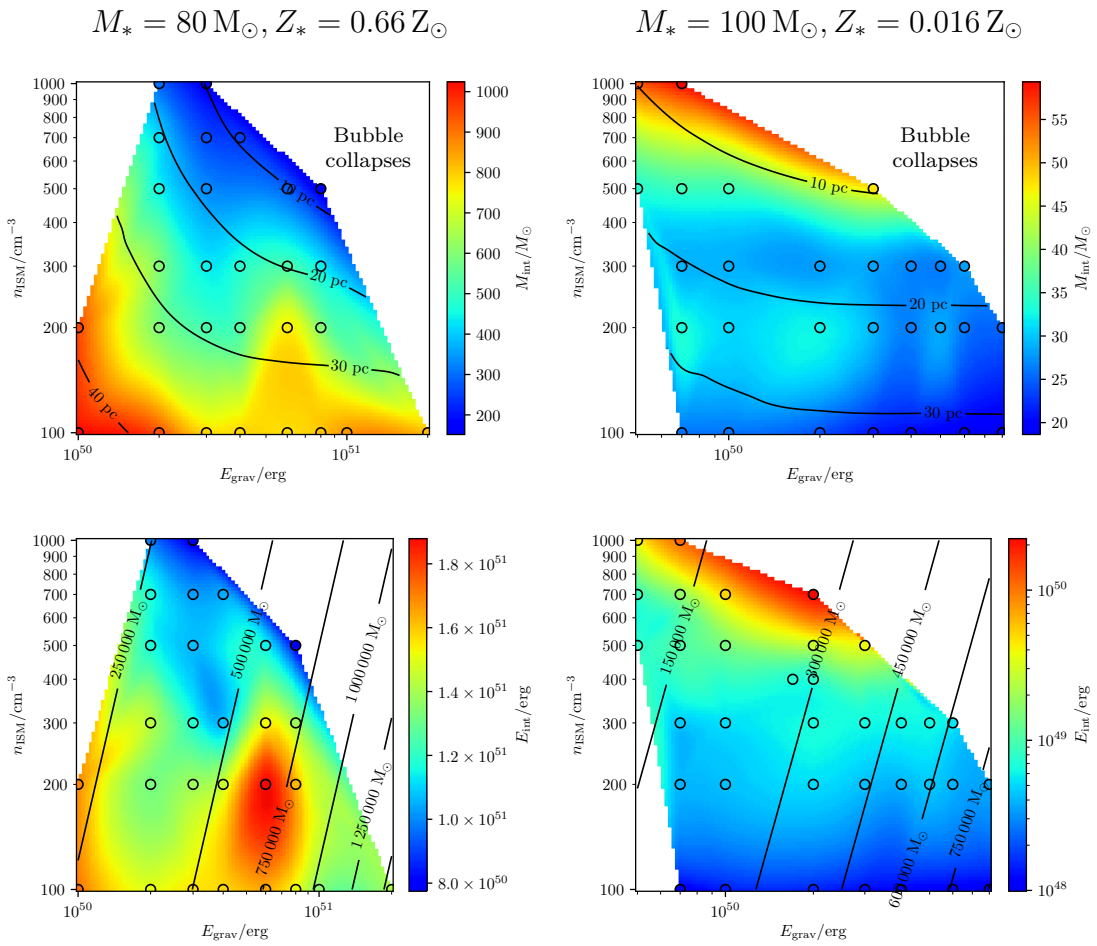

Figure 3.11 Properties of the bubble when the supernova ejecta reflects from the dense shell as a function of the gravitational energy of the initial cloud E_grav and the initial particle density of the cloud n_ISM. The top panels show the mass M_int of the gas under the dense shell. The bottom panels show the internal energy E_int of the gas under the shell. Contours show the radius of the shell and the mass of the initial cloud. The left column shows a $80\,\mathrm{M}_\odot$ Milky Way metallicity star, the right column shows a $100\,\mathrm{M}_\odot$ star with the metallicity of I Zwicky 18. Black circles show individual simulations. Color maps and contours were calculated using cubic interpolation in logarithmic space from the individual simulations.

reflects again with no significant accretion. The moment immediately following the reflection from the center can be seen in the fourth panel. The fifth panel shows the transmitted wave collecting all the gas from the former H II region. The shock eventually goes through the entire bubble and moves most of the material into the dense shell. A weak wave reflects off of the shell, the transmitted wave is not able to go through the shell. The final state of the bubble can be seen in the last panel.

The outcome is the same in all the simulations we explored regardless of the parameters of the star, supernova, or initial cloud of gas. The supernova ejecta remove all of the dense structure from the bubble interior and prevent any significant accretion onto the black hole. If the initial cloud is massive and dense

enough, the whole bubble can collapse. However, the shell is sufficiently massive to form stars. This is not included in our model. The shell would most likely be heavily modified by the feedback from the new stars; therefore, we cannot make any conclusions about the possibility of accreting gas from the shell onto the black hole.

The top panels in figure 3.11 show the mass $M_{\rm int}$ of the gas inside the bubble (under the dense shell) after the supernova ejecta reflects from the shell. The bottom panels show the internal energy $E_{\rm int}$ of the gas under the shell at the same time.

In the case of the Milky Way metallicity star in the left column, the results are similar to those of direct collapse (see figure 3.9) with the difference that the supernova destroys the former H II region in all cases and increases the internal energy of the gas inside the bubble.

In the case of the star with the metallicity of I Zwicky 18, it takes a much longer time for the supernova ejecta to transverse the vast H II region and reflect from the shell. This time strongly depends on the size of the bubble; it can take up to a Myr in the case of a larger bubble. The larger bubble has more time to cool; therefore, there is less mass and energy.

As in the case of direct collapse in Section 3.2.2, the empty spaces in the top right corners of the plots are there because the clouds are too massive and collapse during the lifetime of the star. The white areas on the left sides of the plots are cases where the gravitational energy of the cloud is low, the bubble is large, it takes too long for the supernova ejecta to reach the shell, and the density is too low for accretion.

Figure 3.11 shows only a subset of simulations for two selected parameters of stars. The plots are qualitatively the same for the other cases.

3.3 3D simulations of stellar wind bubbles

We took the most optimistic cases from the 1D parameter space study to see if the results changed in 3D. Running the whole simulation in 3D is computationally expensive; therefore, we start the simulation in 1D and remap it to a 3D Cartesian grid when we expect higher-dimensional effects to become important, which is near the end of the massive star's life. The dense shell of the swept-up ISM is usually much thinner than what could be resolved in 3D. We rescale the shell during the remapping, making sure that mass and energy are conserved. In addition, we add perturbations in the form of spherical harmonics to overshadow the uncontrolled noise coming from the discretization. In 3D, we can realistically have 16× less spatial resolution than in 1D. Anything higher is prohibitively expensive. This can lead to an overestimation of cooling.

3.3.1 Black hole formation with direct collapse

We chose the case of the low-mass ($60\,\mathrm{M}_\odot$) Milky Way metallicity star described in section 3.2.2. In 1D, we saw about $9\,\mathrm{M}_\odot$ of mass accreted onto the black hole in short bursts each time a density wave reflected off of the center of the simulation.

Figure 3.12 shows the density and temperature cuts in the $z = 0$ plane as a function of time since the star collapsed. The first panel is at the moment the

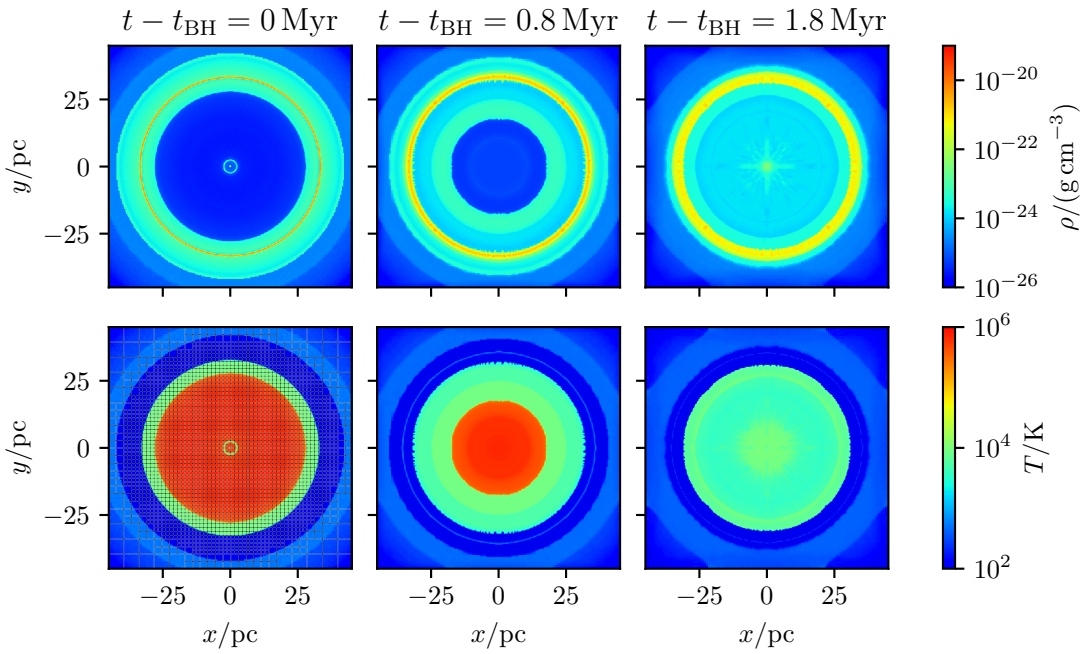

Figure 3.12 Density ρ and temperature T of an interstellar bubble driven by stellar wind from a $60\,{\rm M}_\odot$ Milky Way metallicity star. The bubble expands into a cloud with $n_{\rm ISM} = 100\,{\rm cm^{-3}}$ and $E_{\rm grav} = 2 \times 10^{50}\,{\rm erg}$. The structure of the AMR blocks is shown as an overlay in the first column of the bottom row. Each block consists of $8 \times 8 \times 8$ individual cells.

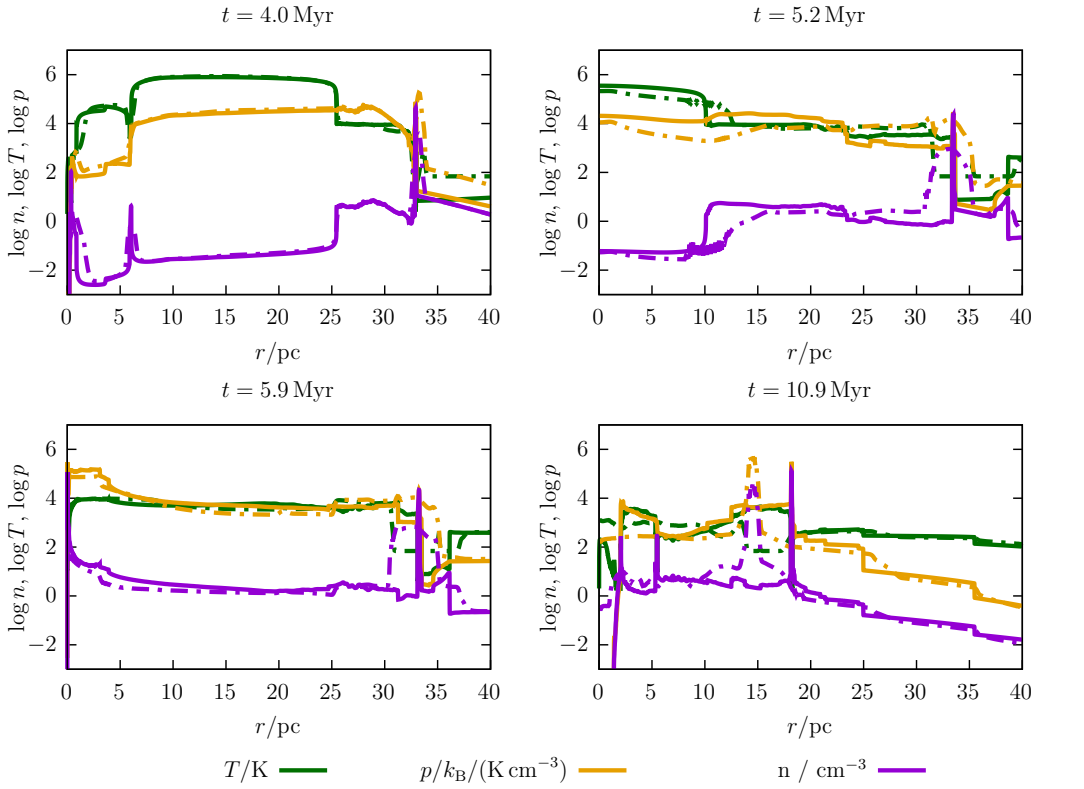

Figure 3.13 Comparison of a 1D simulation (solid lines) and a radially averaged 3D simulation (dashed lines) in the case of direct collapse into a black hole. Profiles of temperature T, pressure p and particle density n are shown.

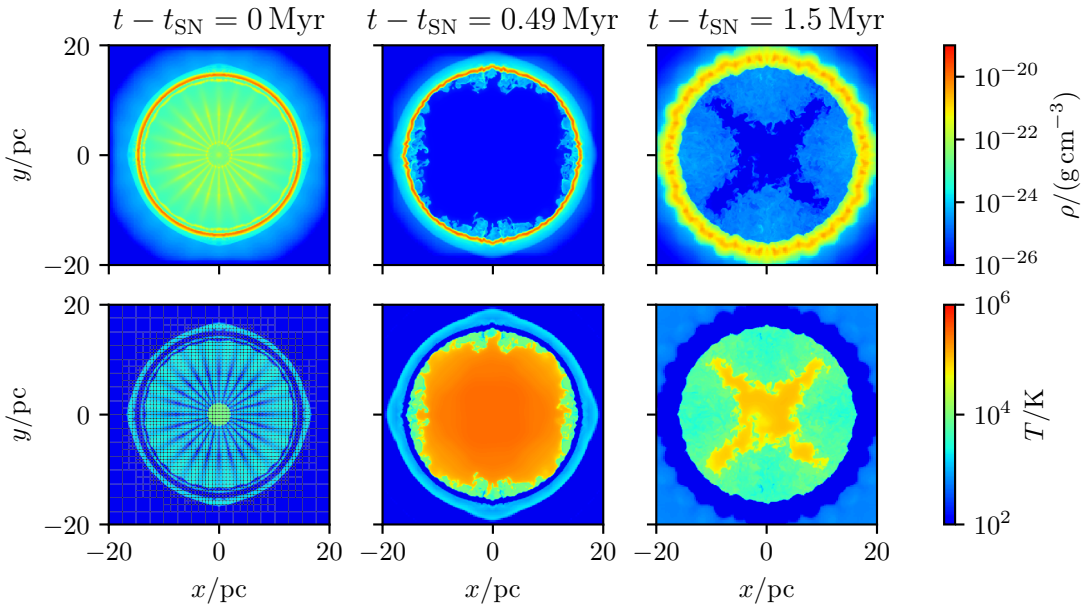

Figure 3.14 Density ρ and temperature T after a supernova explosion inside an interstellar bubble. The bubble was formed by the wind from a $77\,\mathrm{M}_\odot$ star with the metallicity of I Zwicky 18 inside a cloud with $n_{\mathrm{ISM}} = 500\,\mathrm{cm}^{-3}$ and $E_{\mathrm{grav}} = 5 \times 10^{49}\,\mathrm{erg}$. The structure of the AMR blocks is shown as an overlay in the first column of the bottom row. Each block consists of $8 \times 8 \times 8$ individual cells.

star collapses into a black hole, and the simulation is remapped from 1D to 3D. The second panel shows the hot region cooling and the H II region falling towards the black hole. This is consistent with the 1D simulation.

The last panel shows the bubble as the hot region cools completely and the density in the center increases. However, the simulation is not perfectly spherical and the density in the exact center never gets high enough for effective accretion. This would probably be an even bigger issue in a more realistic simulation with an aspherical bubble forming inside an inhomogeneous cloud.

Figure 3.13 shows a comparison of the radially averaged 3D simulation with the high-resolution 1D simulation. The first panel shows the profiles after the grid was remapped from 1D to 3D. The second panel shows the bubble interior cooling faster in 1D. In addition, the shell in 3D is much thicker. The third panel shows the bubble after the interior cools bellow $10^4\,\mathrm{K}$. The profiles look similar; however, the density in the center is much higher in the 1D simulation. The fourth panel shows the whole bubble collapsing 6.9 Myr after the black hole formed. The cooling in the 3D simulation is overestimated, so the bubble collapses faster.

3.3.2 Black hole formation with supernova

For the case of a supernova explosion, we chose a simulation with a $77\,\mathrm{M}_\odot$ star with the metallicity of I Zwicky 18 that is evolving inside a cloud with $n_{\mathrm{ISM}} = 500\,\mathrm{cm}^{-3}$ and $E_{\mathrm{grav}} = 5 \times 10^{49}\,\mathrm{erg}$. The simulation was done in 1D for the first 90 % of the star's evolution and remapped to a 3D grid 300 kyr before the supernova explosion.

Figure 3.14 shows the density and temperature cuts in the $z = 0$ plane as

a function of time since the supernova explosion. The first panel shows the structure of the bubble just before the supernova explosion. The concentric rays are the result of perturbations in the form of spherical harmonics added to the 3D grid when remapping from 1D. The H II region is already cooling below 10^4 K.

The second panel shows the bubble after the supernova ejecta push all of the dense material from the former H II region into the shell and reionizes the inside of the bubble. The third panel shows that the hot gas is slowly cooling. However, the density inside the bubble is still low and there is no significant accretion even after the whole bubble cools. This is in agreement with the 1D spherically-symmetric simulations.

4 Conclusions

We performed state-of-the-art 1D and 3D hydrodynamic simulations of interstellar bubbles driven by the winds of massive stars. The simulations include thermal conduction, radiative cooling, ionizing UV radiation from the star, gravity, stellar wind, supernova explosions, and gas accretion onto newly formed black holes.

We tracked the evolution of these bubbles from the main-sequence phase of the progenitor stars to millions of years after their collapse into stellar-mass black holes. Two scenarios were investigated: one where the star undergoes a direct collapse without an explosion, and one where it ends in a core-collapse supernova. For each scenario, we explored two different metallicities—Milky Way and I Zwicky 18. Our goal was to find out how much gas from the pre-blown bubble can be accreted by the black hole. Our key findings are as follows:

1. We examined a wide range of stellar and interstellar medium parameters and found that thermal conduction, radiative cooling, and ionizing radiation play a key role in determining the bubble structure and evolution. These processes are essential for realistic simulations.

2. A supernova explosion within the bubble strongly suppresses the accretion of gas to the black hole for both metallicities. The ejecta pushes any dense gas into the shell of the swept-up interstellar medium. The gas left inside the bubble is not dense enough to cool below $10^4\,\mathrm{K}$, making its pressure too high for accretion.

3. Even without a supernova, strong winds from massive ($\gtrsim 80\,\mathrm{M}_\odot$) high-metallicity stars prevent accretion. These late-stage winds act on the bubble in a way similar to a supernova by evacuating the bubble of dense gas.

4. Lower-mass ($\lesssim 60\,\mathrm{M}_\odot$) high-metallicity stars allow the bubbles to cool. The dense gas from a former H II region can fall toward the black hole. However, we only saw significant accretion in 1D spherically symmetric simulations. In 3D, the gas around the black hole never gets dense enough for it to cool below $10^4\,\mathrm{K}$, and the high pressure prevents any significant accretion.

5. Bubbles blown by low-metallicity stars remain too hot and overpressurized for accretion. In addition, high-mass stars ($\gtrsim 77\,\mathrm{M}_\odot$) with strong late-stage winds form dense inner shells that act as barriers, isolating the black hole from potential infall.

The full range of outcomes depending on the collapse mechanism, metallicity, and progenitor mass is summarized in table 4.1.

Our model omits other stars surrounding the progenitor and star formation in the dense shell of the swept-up ISM, which could introduce additional feedback and redistribute mass in the bubble. More sophisticated models would be needed to see whether this would enhance or suppress the accretion onto the black hole.

Another possible topic for future research would be to consider more realistic inhomogeneous turbulent clouds. This would break up the spherical symmetry and could alter the results by introducing turbulence and instabilities.

Table 4.1 Summary of all possible outcomes depending on the black hole formation mechanism (DC = direct collapse, SN = core-collapse supernova), metallicity Z (MW = Milky Way, IZw18 = I Zwicky 18), and zero-age main-sequence mass of the star $M*$.

	Z	$M_*/\mathrm{M}_\odot$	Resulting environment / Accretion outcome
DC	MW	$\lesssim$60	Modest accretion of gas from H II region in 1D, no accretion in 3D
		$\gtrsim 80$	Hot rarefied bubble interior, no accretion
	IZw18	$\lesssim 45$	Warm rarefied bubble interior, no accretion
		$\gtrsim 77$	Inner shell of slow late wind preventing accretion
SN	MW	$\lesssim 60$	Small low mass H II region, SN erases all dense structures, no accretion
		$\gtrsim 80$	
	IZw18	$\lesssim 45$	Large massive H II region, SN takes longer to transverse the bubble, but eventually erases all dense structures, no accretion
		$\gtrsim 77$	

Although our simulations show little accretion of gas from interstellar bubbles onto newly formed black holes under the conditions explored, they lay essential groundwork for more advanced future studies. In addition, this work presents the most comprehensive parameter space study to date of bubbles blown by massive stars and the evolution of supernovae within them.

Bibliography

Aasi, J. et al., 2015. Advanced LIGO. *Classical and Quantum Gravity* [online]. Vol. 32, p. 074001 [visited on 2025-03-11]. ISSN 0264-9381. Available from DOI: 10.1088/0264-9381/32/7/074001. Publisher: IOP ADS Bibcode: 2015CQGra..32g4001L.

Abbott, R. et al., 2023. GWTC-3: Compact Binary Coalescences Observed by LIGO and Virgo during the Second Part of the Third Observing Run. *Physical Review X* [online]. Vol. 13, p. 041039 [visited on 2025-03-11]. Available from DOI: 10.1103/PhysRevX.13.041039. Publisher: APS ADS Bibcode: 2023PhRvX..13d1039A.

Acernese, F. et al., 2015. Advanced Virgo: a second-generation interferometric gravitational wave detector. *Classical and Quantum Gravity* [online]. Vol. 32, p. 024001 [visited on 2025-03-11]. ISSN 0264-9381. Available from DOI: 10.1088/0264-9381/32/2/024001. Publisher: IOP ADS Bibcode: 2015CQGra..32b4001A.

Adams, S. M.; Kochanek, C. S.; Prieto, J. L.; Dai, X.; Shappee, B. J.; Stanek, K. Z., 2016. Almost gone: SN 2008S and NGC 300 2008OT-1 are fainter than their progenitors. *Monthly Notices of the Royal Astronomical Society* [online]. Vol. 460, pp. 1645–1657 [visited on 2025-03-30]. ISSN 0035-8711. Available from DOI: 10.1093/mnras/stw1059. Publisher: OUP ADS Bibcode: 2016MNRAS.460.1645A.

Airapetian, V.; Carpenter, K. G.; Ofman, L., 2010. Winds from Luminous Late-type Stars. II. Broadband Frequency Distribution of Alfvén Waves. *The Astrophysical Journal* [online]. Vol. 723, pp. 1210–1218 [visited on 2025-04-21]. ISSN 0004-637X. Available from DOI: 10.1088/0004-637X/723/2/1210. Publisher: IOP ADS Bibcode: 2010ApJ...723.1210A.

Allen, C., 2011. Overview and current relevance of "Run-away stars as the result of the gravitational collapse of proto-stellar clusters" by Poveda, Ruiz, & Allen (1967) [online]. Vol. 39, pp. 21–25 [visited on 2025-03-30]. Available from: https://ui.adsabs.harvard.edu/abs/2011RMxAC..39...21A. Conference Name: Revista Mexicana de Astronomia y Astrofisica Conference Series ADS Bibcode: 2011RMxAC..39...21A.

Antonini, Fabio; Rasio, Frederic A., 2016. MERGING BLACK HOLE BINARIES IN GALACTIC NUCLEI: IMPLICATIONS FOR ADVANCED-LIGO DETECTIONS. *The Astrophysical Journal* [online]. Vol. 831, no. 2, p. 187 [visited on 2025-03-29]. ISSN 0004-637X. Available from DOI: 10.3847/0004-637X/831/2/187. Publisher: The American Astronomical Society.

Antonini, Fabio; Romero-Shaw, Isobel M.; Callister, Thomas, 2025. Star Cluster Population of High Mass Black Hole Mergers in Gravitational Wave Data. *Physical Review Letters* [online]. Vol. 134, no. 1, p. 011401 [visited on 2025-03-12]. Available from DOI: 10.1103/PhysRevLett.134.011401. Publisher: American Physical Society.

Arca Sedda, Manuel, 2020. Birth, Life, and Death of Black Hole Binaries around Supermassive Black Holes: Dynamical Evolution of Gravitational Wave Sources. *The Astrophysical Journal* [online]. Vol. 891, p. 47 [visited on 2025-03-29]. ISSN 0004-637X. Available from DOI: 10.3847/1538-4357/ab723b. Publisher: IOP ADS Bibcode: 2020ApJ...891...47A.

Arthur, S. J., 2007. Wind-Blown Bubbles and HII Regions around Massive Stars [online]. Vol. 30, pp. 64–71 [visited on 2025-03-04]. Available from: https://ui.adsabs.harvard.edu/abs/2007RMxAC..30...64A. Conference Name: Revista Mexicana de Astronomia y Astrofisica Conference Series ADS Bibcode: 2007RMxAC..30...64A.

Avedisova, V. S., 1972. Formation of Nebulae by Wolf-Rayet Stars. *Soviet Astronomy* [online]. Vol. 15, p. 708 [visited on 2025-04-03]. ISSN 0038-5301. Available from: https://ui.adsabs.harvard.edu/abs/1972SvA....15..708A. ADS Bibcode: 1972SvA....15..708A.

El-Badry, Kareem; Ostriker, Eve C.; Kim, Chang-Goo; Quataert, Eliot; Weisz, Daniel R., 2019. Evolution of supernovae-driven superbubbles with conduction and cooling. *Monthly Notices of the Royal Astronomical Society* [online]. Vol. 490, pp. 1961–1990 [visited on 2025-01-22]. ISSN 0035-8711. Available from DOI: 10.1093/mnras/stz2773. Publisher: OUP ADS Bibcode: 2019MNRAS.490.1961E.

El-Badry, Kareem; Rix, Hans-Walter; Cendes, Yvette, et al., 2023. A red giant orbiting a black hole. *Monthly Notices of the Royal Astronomical Society* [online]. Vol. 521, pp. 4323–4348 [visited on 2025-03-11]. ISSN 0035-8711. Available from DOI: 10.1093/mnras/stad799. Publisher: OUP ADS Bibcode: 2023MNRAS.521.4323E.

El-Badry, Kareem; Rix, Hans-Walter; Quataert, Eliot, et al., 2023. A Sun-like star orbiting a black hole. *Monthly Notices of the Royal Astronomical Society* [online]. Vol. 518, pp. 1057–1085 [visited on 2025-03-11]. ISSN 0035-8711. Available from DOI: 10.1093/mnras/stac3140. Publisher: OUP ADS Bibcode: 2023MNRAS.518.1057E.

Balbus, S. A.; McKee, C. F., 1982. The evaporation of spherical clouds in a hot gas. III - Suprathermal evaporation. *The Astrophysical Journal* [online]. Vol. 252, pp. 529–552 [visited on 2025-02-05]. ISSN 0004-637X. Available from DOI: 10.1086/159581. Publisher: IOP ADS Bibcode: 1982ApJ...252..529B.

Balsara, Dinshaw S.; Tilley, David A.; Howk, J. Christopher, 2008. Simulating anisotropic thermal conduction in supernova remnants - I. Numerical methods. *Monthly Notices of the Royal Astronomical Society* [online]. Vol. 386, pp. 627–641 [visited on 2025-04-25]. ISSN 0035-8711. Available from DOI: 10.1111/j.1365-2966.2008.13085.x. Publisher: OUP ADS Bibcode: 2008MNRAS.386..627B.

Bartos, Imre; Kocsis, Bence; Haiman, Zoltán; Márka, Szabolcs, 2017. Rapid and Bright Stellar-mass Binary Black Hole Mergers in Active Galactic Nuclei. *The Astrophysical Journal* [online]. Vol. 835, p. 165 [visited on 2025-03-29]. ISSN 0004-637X. Available from DOI: 10.3847/1538-4357/835/2/165. Publisher: IOP ADS Bibcode: 2017ApJ...835..165B.

Beasor, Emma R.; Davies, Ben, 2016. The evolution of red supergiants to supernova in NGC 2100. *Monthly Notices of the Royal Astronomical Society* [online]. Vol. 463, pp. 1269–1283 [visited on 2025-03-30]. ISSN 0035-8711. Available from DOI: 10.1093/mnras/stw2054. Publisher: OUP ADS Bibcode: 2016MNRAS.463.1269B.

Belczynski, K.; Heger, A.; Gladysz, W.; Ruiter, A. J.; Woosley, S.; Wiktorowicz, G.; Chen, H. -Y.; Bulik, T.; O'Shaughnessy, R.; Holz, D. E.; Fryer, C. L.; Berti, E., 2016. The effect of pair-instability mass loss on black-hole mergers. *Astronomy and Astrophysics* [online]. Vol. 594, A97 [visited on 2024-11-29]. ISSN 0004-6361. Available from DOI: 10.1051/0004-6361/201628980. ADS Bibcode: 2016A&A...594A..97B.

Blaauw, A., 1961. On the origin of the O- and B-type stars with high velocities (the "run-away" stars), and some related problems. *Bulletin of the Astronomical Institutes of the Netherlands* [online]. Vol. 15, p. 265 [visited on 2025-03-30]. ISSN 0365-8910. Available from: https://ui.adsabs.harvard.edu/abs/1961BAN....15..265B. ADS Bibcode: 1961BAN....15..265B.

Bolton, C. T., 1972. Identification of Cygnus X-1 with HDE 226868. *Nature* [online]. Vol. 235, pp. 271–273 [visited on 2025-03-11]. ISSN 0028-0836. Available from DOI: 10.1038/235271b0. ADS Bibcode: 1972Natur.235..271B.

Bombaci, I., 1996. The maximum mass of a neutron star. *Astronomy and Astrophysics* [online]. Vol. 305, p. 871 [visited on 2025-03-11]. ISSN 0004-6361. Available from: https://ui.adsabs.harvard.edu/abs/1996A&A...305..871B. ADS Bibcode: 1996A&A...305..871B.

Bonnell, I. A.; Pringle, J. E., 1995. Gravitational radiation from supernovae. *Monthly Notices of the Royal Astronomical Society* [online]. Vol. 273, pp. L12–L14 [visited on 2025-03-30]. ISSN 0035-8711. Available from DOI: 10.1093/mnras/273.1.L12. Publisher: OUP ADS Bibcode: 1995MNRAS.273L..12B.

Borkowski, Kazimierz; Szymkowiak, Andrew E.; Blondin, John M.; Sarazin, Craig L., 1996. A Circumstellar Shell Model for the Cassiopeia A Supernova Remnant. *The Astrophysical Journal* [online]. Vol. 466, p. 866 [visited on 2025-03-04]. ISSN 0004-637X. Available from DOI: 10.1086/177560. Publisher: IOP ADS Bibcode: 1996ApJ...466..866B.

Boroson, Bram; McCray, Richard; Clark, Oelfke; Slavin, Jonathan; Mac Low, Mordecai-Mark; Chu, You-Hua; Van Buren, Dave, 1997. An Interstellar Conduction Front within a Wolf-Rayet Ring Nebula Observed with the Goddard High Resolution Spectrograph. *The Astrophysical Journal* [online]. Vol. 478, pp. 638–647 [visited on 2025-04-25]. ISSN 0004-637X. Available from DOI: 10.1086/303799. Publisher: IOP ADS Bibcode: 1997ApJ...478..638B.

Broekgaarden, Floor S; Berger, Edo; Stevenson, Simon; Justham, Stephen; Mandel, Ilya; Chruślińska, Martyna; Son, Lieke A C van; Wagg, Tom; Vigna-Gómez, Alejandro; Mink, Selma E de; Chattopadhyay, Debatri; Neijssel, Coenraad J, 2022. Impact of massive binary star and cosmic evolution on gravitational wave observations – II. Double compact object rates and properties. *Monthly Notices of the Royal Astronomical Society* [online]. Vol. 516, no. 4, pp. 5737–5761 [visited on 2025-03-12]. ISSN 0035-8711. Available from DOI: 10.1093/mnras/stac1677.

Burdge, Kevin B.; El-Badry, Kareem; Kara, Erin; Canizares, Claude; Chakrabarty, Deepto; Frebel, Anna; Millholland, Sarah C.; Rappaport, Saul; Simcoe, Rob; Vanderburg, Andrew, 2024. The black hole low-mass X-ray binary V404 Cygni is part of a wide triple. *Nature* [online]. Vol. 635, no. 8038, pp. 316–320 [visited on 2025-04-21]. issn 0028-0836, issn 1476-4687. Available from doi: 10.1038/s41586-024-08120-6.

Byrne, G. D.; Hindmarsh, A. C., 1975. A Polyalgorithm for the Numerical Solution of Ordinary Differential Equations. *ACM Trans. Math. Softw.* [online]. Vol. 1, no. 1, pp. 71–96 [visited on 2025-02-04]. issn 0098-3500. Available from doi: 10.1145/355626.355636.

Campanelli, Manuela; Lousto, Carlos O.; Zlochower, Yosef; Merritt, David, 2007. Maximum Gravitational Recoil. *Physical Review Letters* [online]. Vol. 98, p. 231102 [visited on 2025-03-29]. issn 0031-9007. Available from doi: 10.1103/PhysRevLett.98.231102. Publisher: APS ADS Bibcode: 2007PhRvL..98w1102C.

Campbell, P. M., 1984. Transport phenomena in a completely ionized gas with large temperature gradients. *Physical Review A* [online]. Vol. 30, pp. 365–373 [visited on 2025-02-05]. issn 1050-29470556-2791. Available from doi: 10.1103/PhysRevA.30.365. Publisher: APS ADS Bibcode: 1984PhRvA..30..365C.

Cappa, Cristina E.; Arnal, E. Marcelo; Cichowolski, Silvina; Goss, W. Miller; Pineault, Serge, 2003. Radio observations of interstellar bubbles surrounding massive stars [online]. Vol. 212, p. 596 [visited on 2025-03-04]. Available from: https://ui.adsabs.harvard.edu/abs/2003IAUS..212..596C. Conference Name: A Massive Star Odyssey: From Main Sequence to Supernova ADS Bibcode: 2003IAUS..212..596C.

Castor, J.; McCray, R.; Weaver, R., 1975. Interstellar bubbles. *The Astrophysical Journal* [online]. Vol. 200, pp. L107–L110 [visited on 2024-11-13]. issn 0004-637X. Available from doi: 10.1086/181908. Publisher: IOP ADS Bibcode: 1975ApJ...200L.107C.

Chandrasekhar, S., 1931. The Maximum Mass of Ideal White Dwarfs. *The Astrophysical Journal* [online]. Vol. 74, p. 81 [visited on 2025-04-14]. issn 0004-637X. Available from doi: 10.1086/143324. Publisher: IOP ADS Bibcode: 1931ApJ....74...81C.

Chu, You-Hua; Guerrero, Martín A.; Gruendl, Robert A.; García-Segura, Guillermo; Wendker, Heinrich J., 2003. Hot Gas in the Circumstellar Bubble S308. *The Astrophysical Journal* [online]. Vol. 599, pp. 1189–1195 [visited on 2025-04-25]. issn 0004-637X. Available from doi: 10.1086/379607. Publisher: IOP ADS Bibcode: 2003ApJ...599.1189C.

Chu, You-Hua; Treffers, R. R.; Kwitter, K. B., 1983. Galactic ring nebulae associated with Wolf-Rayet stars. VIII. Summaryand atlas. *The Astrophysical Journal Supplement Series* [online]. Vol. 53, pp. 937–944 [visited on 2025-04-23]. issn 0067-0049. Available from doi: 10.1086/190914. Publisher: IOP ADS Bibcode: 1983ApJS...53..937C.

Churchwell, E. et al., 2006. The Bubbling Galactic Disk. *The Astrophysical Journal* [online]. Vol. 649, pp. 759–778 [visited on 2025-04-23]. ISSN 0004-637X. Available from DOI: 10.1086/507015. Publisher: IOP ADS Bibcode: 2006ApJ...649..759C.

Colella, Phillip; Woodward, Paul R, 1984. The Piecewise Parabolic Method (PPM) for gas-dynamical simulations. *Journal of Computational Physics* [online]. Vol. 54, no. 1, pp. 174–201 [visited on 2025-01-22]. ISSN 0021-9991. Available from DOI: 10.1016/0021-9991(84)90143-8.

Corral-Santana, J. M.; Casares, J.; Muñoz-Darias, T.; Bauer, F. E.; Martínez-Pais, I. G.; Russell, D. M., 2016. BlackCAT: A catalogue of stellar-mass black holes in X-ray transients. *Astronomy and Astrophysics* [online]. Vol. 587, A61 [visited on 2025-03-15]. ISSN 0004-6361. Available from DOI: 10.1051/0004-6361/201527130. Publisher: EDP ADS Bibcode: 2016A&A...587A..61C.

Courant, R.; Friedrichs, K.; Lewy, H., 1928. Über die partiellen Differenzengleichungen der mathematischen Physik. *Mathematische Annalen* [online]. Vol. 100, no. 1, pp. 32–74 [visited on 2025-01-23]. ISSN 1432-1807. Available from DOI: 10.1007/BF01448839.

Cowie, L. L.; McKee, C. F., 1977. The evaporation of spherical clouds in a hot gas. I. Classical and saturated mass loss rates. *The Astrophysical Journal* [online]. Vol. 211, pp. 135–146 [visited on 2025-01-30]. ISSN 0004-637X. Available from DOI: 10.1086/154911. Publisher: IOP ADS Bibcode: 1977ApJ...211..135C.

Crowther, Paul A.; Schnurr, Olivier; Hirschi, Raphael; Yusof, Norhasliza; Parker, Richard J.; Goodwin, Simon P.; Kassim, Hasan Abu, 2010. The R136 star cluster hosts several stars whose individual masses greatly exceed the accepted 150Msolar stellar mass limit. *Monthly Notices of the Royal Astronomical Society* [online]. Vol. 408, pp. 731–751 [visited on 2025-03-13]. ISSN 0035-8711. Available from DOI: 10.1111/j.1365-2966.2010.17167.x. Publisher: OUP ADS Bibcode: 2010MNRAS.408..731C.

Dalgarno, A.; McCray, R. A., 1972. Heating and Ionization of HI Regions. *Annual Review of Astronomy and Astrophysics* [online]. Vol. 10, p. 375 [visited on 2025-01-22]. ISSN 0066-4146. Available from DOI: 10.1146/annurev.aa.10.090172.002111. ADS Bibcode: 1972ARA&A..10..375D.

Dhawan, V.; Mirabel, I. F.; Ribó, M.; Rodrigues, I., 2007. Kinematics of Black Hole X-Ray Binary GRS 1915+105. *The Astrophysical Journal* [online]. Vol. 668, pp. 430–434 [visited on 2025-03-30]. ISSN 0004-637X. Available from DOI: 10.1086/520111. Publisher: IOP ADS Bibcode: 2007ApJ...668..430D.

Doctor, Z.; Wysocki, D.; O'Shaughnessy, R.; Holz, D. E.; Farr, B., 2020. Black Hole Coagulation: Modeling Hierarchical Mergers in Black Hole Populations. *The Astrophysical Journal* [online]. Vol. 893, no. 1, p. 35 [visited on 2025-03-12]. ISSN 0004-637X. Available from DOI: 10.3847/1538-4357/ab7fac. Publisher: The American Astronomical Society.

Duchêne, Gaspard; Kraus, Adam, 2013. Stellar Multiplicity. *Annual Review of Astronomy and Astrophysics* [online]. Vol. 51, pp. 269–310 [visited on 2025-03-29]. ISSN 0066-4146. Available from DOI: 10.1146/annurev-astro-081710-102602. ADS Bibcode: 2013ARA&A..51..269D.

Dwarkadas, V. V.; Rosenberg, D. L., 2013. Simulated X-ray spectra from ionized wind-blown nebulae around massive stars. *High Energy Density Physics* [online]. Vol. 9, pp. 226–230 [visited on 2025-02-27]. Available from doi: 10.1016/j.hedp.2012.12.003. ADS Bibcode: 2013HEDP....9..226D.

Dwarkadas, Vikram V., 2005. The Evolution of Supernovae in Circumstellar Wind-Blown Bubbles. I. Introduction and One-Dimensional Calculations. *The Astrophysical Journal* [online]. Vol. 630, pp. 892–910 [visited on 2025-02-26]. issn 0004-637X. Available from doi: 10.1086/432109. Publisher: IOP ADS Bibcode: 2005ApJ...630..892D.

Dwarkadas, Vikram V., 2007. The Evolution of Supernovae in Circumstellar Wind Bubbles. II. Case of a Wolf-Rayet Star. *The Astrophysical Journal* [online]. Vol. 667, pp. 226–247 [visited on 2025-02-26]. issn 0004-637X. Available from doi: 10.1086/520670. Publisher: IOP ADS Bibcode: 2007ApJ...667..226D.

Ebinger, Kevin; Curtis, Sanjana; Fröhlich, Carla; Hempel, Matthias; Perego, Albino; Liebendörfer, Matthias; Thielemann, Friedrich-Karl, 2019. PUSHing Core-collapse Supernovae to Explosions in Spherical Symmetry. II. Explodability and Remnant Properties. *The Astrophysical Journal* [online]. Vol. 870, p. 1 [visited on 2025-03-13]. issn 0004-637X. Available from doi: 10.3847/1538-4357/aae7c9. Publisher: IOP ADS Bibcode: 2019ApJ...870....1E.

Ekström, S.; Georgy, C.; Eggenberger, P.; Meynet, G.; Mowlavi, N.; Wyttenbach, A.; Granada, A.; Decressin, T.; Hirschi, R.; Frischknecht, U.; Charbonnel, C.; Maeder, A., 2012. Grids of stellar models with rotation. I. Models from 0.8 to 120 M at solar metallicity (Z = 0.014). *Astronomy and Astrophysics* [online]. Vol. 537, A146 [visited on 2025-03-30]. issn 0004-6361. Available from doi: 10.1051/0004-6361/201117751. Publisher: EDP ADS Bibcode: 2012A&A...537A.146E.

Ertl, T.; Janka, H. -Th.; Woosley, S. E.; Sukhbold, T.; Ugliano, M., 2016. A Two-parameter Criterion for Classifying the Explodability of Massive Stars by the Neutrino-driven Mechanism. *The Astrophysical Journal* [online]. Vol. 818, p. 124 [visited on 2025-03-13]. issn 0004-637X. Available from doi: 10.3847/0004-637X/818/2/124. Publisher: IOP ADS Bibcode: 2016ApJ...818..124E.

Falgout, Robert D.; Jones, Jim E.; Yang, Ulrike Meier, 2006. The Design and Implementation of hypre, a Library of Parallel High Performance Preconditioners. In: Bruaset, Are Magnus; Tveito, Aslak (eds.). *Numerical Solution of Partial Differential Equations on Parallel Computers*. Berlin, Heidelberg: Springer Berlin Heidelberg, pp. 267–294. isbn 978-3-540-31619-0. Available from doi: 10.1007/3-540-31619-1_8.

Figer, Donald F., 2005. An upper limit to the masses of stars. *Nature* [online]. Vol. 434, pp. 192–194 [visited on 2025-03-13]. issn 0028-0836. Available from doi: 10.1038/nature03293. ADS Bibcode: 2005Natur.434..192F.

Fowler, William A.; Hoyle, F., 1964. Neutrino Processes and Pair Formation in Massive Stars and Supernovae. *The Astrophysical Journal Supplement Series* [online]. Vol. 9, p. 201 [visited on 2025-03-12]. issn 0067-0049. Available from doi: 10.1086/190103. Publisher: IOP ADS Bibcode: 1964ApJS....9..201F.

Fragos, T.; Willems, B.; Kalogera, V.; Ivanova, N.; Rockefeller, G.; Fryer, C. L.; Young, P. A., 2009. Understanding Compact Object Formation and Natal Kicks. II. The Case of XTE J1118 + 480. *The Astrophysical Journal* [online]. Vol. 697, pp. 1057–1070 [visited on 2025-03-30]. ISSN 0004-637X. Available from DOI: 10.1088/0004-637X/697/2/1057. Publisher: IOP ADS Bibcode: 2009ApJ...697.1057F.

Freyer, Tim; Hensler, Gerhard; Yorke, Harold W., 2003. Massive Stars and the Energy Balance of the Interstellar Medium. I. The Impact of an Isolated 60 Msolar Star. *The Astrophysical Journal* [online]. Vol. 594, pp. 888–910 [visited on 2025-04-22]. ISSN 0004-637X. Available from DOI: 10.1086/376937. Publisher: IOP ADS Bibcode: 2003ApJ...594..888F.

Fryer, C. L.; Woosley, S. E.; Heger, A., 2001. Pair-Instability Supernovae, Gravity Waves, and Gamma-Ray Transients. *The Astrophysical Journal* [online]. Vol. 550, pp. 372–382 [visited on 2025-03-13]. ISSN 0004-637X. Available from DOI: 10.1086/319719. Publisher: IOP ADS Bibcode: 2001ApJ...550..372F.

Fryer, Christopher L.; Kusenko, Alexander, 2006. Effects of Neutrino-driven Kicks on the Supernova Explosion Mechanism. *The Astrophysical Journal Supplement Series* [online]. Vol. 163, pp. 335–343 [visited on 2025-03-30]. ISSN 0067-0049. Available from DOI: 10.1086/500933. Publisher: IOP ADS Bibcode: 2006ApJS..163..335F.

Fryxell, B.; Olson, K.; Ricker, P.; Timmes, F. X.; Zingale, M.; Lamb, D. Q.; MacNeice, P.; Rosner, R.; Truran, J. W.; Tufo, H., 2000. FLASH: An Adaptive Mesh Hydrodynamics Code for ModelingAstrophysical Thermonuclear Flashes. *The Astrophysical Journal Supplement Series* [online]. Vol. 131, no. 1, p. 273 [visited on 2025-01-22]. ISSN 0067-0049. Available from DOI: 10.1086/317361. Publisher: IOP Publishing.

Gaia Collaboration et al., 2016. The Gaia mission. *Astronomy and Astrophysics* [online]. Vol. 595, A1 [visited on 2025-03-11]. ISSN 0004-6361. Available from DOI: 10.1051/0004-6361/201629272. Publisher: EDP ADS Bibcode: 2016A&A...595A...1G.

Garcia-Segura, G.; Langer, N.; Mac Low, M. -M., 1996. The hydrodynamic evolution of circumstellar gas around massive stars. II. The impact of the time sequence O star -> RSG -> WR star. *Astronomy and Astrophysics* [online]. Vol. 316, pp. 133–146 [visited on 2025-04-03]. ISSN 0004-6361. Available from: https://ui.adsabs.harvard.edu/abs/1996A&A...316..133G. ADS Bibcode: 1996A&A...316..133G.

Garcia-Segura, G.; Mac Low, M. -M.; Langer, N., 1996. The dynamical evolution of circumstellar gas around massive stars. I. The impact of the time sequence Ostar -> LBV -> WR star. *Astronomy and Astrophysics* [online]. Vol. 305, p. 229 [visited on 2025-04-03]. ISSN 0004-6361. Available from: https://ui.adsabs.harvard.edu/abs/1996A&A...305..229G. ADS Bibcode: 1996A&A...305..229G.

Geen, Sam; Koter, Alex de, 2022. Bottling the champagne: dynamics and radiation trapping of wind-driven bubbles around massive stars. *Monthly Notices of the Royal Astronomical Society* [online]. Vol. 509, pp. 4498–4514 [visited on 2025-03-09]. ISSN 0035-8711. Available from DOI: 10.1093/mnras/stab3245. Publisher: OUP ADS Bibcode: 2022MNRAS.509.4498G.

Geen, Sam; Rosdahl, Joakim; Blaizot, Jeremy; Devriendt, Julien; Slyz, Adrianne, 2015. A detailed study of feedback from a massive star. *Monthly Notices of the Royal Astronomical Society* [online]. Vol. 448, pp. 3248–3264 [visited on 2025-04-03]. ISSN 0035-8711. Available from DOI: 10.1093/mnras/stv251. Publisher: OUP ADS Bibcode: 2015MNRAS.448.3248G.

Gerke, J. R.; Kochanek, C. S.; Stanek, K. Z., 2015. The search for failed supernovae with the Large Binocular Telescope: first candidates. *Monthly Notices of the Royal Astronomical Society* [online]. Vol. 450, pp. 3289–3305 [visited on 2025-03-30]. ISSN 0035-8711. Available from DOI: 10.1093/mnras/stv776. Publisher: OUP ADS Bibcode: 2015MNRAS.450.3289G.

Gerosa, Davide; Fishbach, Maya, 2021. Hierarchical mergers of stellar-mass black holes and their gravitational-wave signatures. *Nature Astronomy* [online]. Vol. 5, pp. 749–760 [visited on 2025-04-21]. ISSN 2397-3366. Available from DOI: 10.1038/s41550-021-01398-w. ADS Bibcode: 2021NatAs...5..749G.

González, José A.; Hannam, Mark; Sperhake, Ulrich; Brügmann, Bernd; Husa, Sascha, 2007. Supermassive Recoil Velocities for Binary Black-Hole Mergers with Antialigned Spins. *Physical Review Letters* [online]. Vol. 98, p. 231101 [visited on 2025-03-29]. ISSN 0031-9007. Available from DOI: 10.1103/PhysRevLett.98.231101. Publisher: APS ADS Bibcode: 2007PhRvL..98w1101G.

González Hernández, Jonay I.; Casares, Jorge; Rebolo, Rafael; Israelian, Garik; Filippenko, Alexei V.; Chornock, Ryan, 2011. Chemical Abundances of the Secondary Star in the Black Hole X-Ray Binary V404 Cygni. *The Astrophysical Journal* [online]. Vol. 738, p. 95 [visited on 2025-03-30]. ISSN 0004-637X. Available from DOI: 10.1088/0004-637X/738/1/95. Publisher: IOP ADS Bibcode: 2011ApJ...738...95G.

González Hernández, Jonay I.; Rebolo, Rafael; Israelian, Garik; Harlaftis, Emilios T.; Filippenko, Alexei V.; Chornock, Ryan, 2006. XTE J1118+480: A Metal-rich Black Hole Binary in the Galactic Halo. *The Astrophysical Journal* [online]. Vol. 644, pp. L49–L52 [visited on 2025-03-30]. ISSN 0004-637X. Available from DOI: 10.1086/505391. Publisher: IOP ADS Bibcode: 2006ApJ...644L..49G.

Gourgoulhon, E.; Haensel, P., 1993. Upper bounds on the neutrino burst from collapse of a neutron star into a black hole. *Astronomy and Astrophysics* [online]. Vol. 271, p. 187 [visited on 2025-03-30]. ISSN 0004-6361. Available from: https://ui.adsabs.harvard.edu/abs/1993A&A...271..187G. ADS Bibcode: 1993A&A...271..187G.

Green, Samuel; Mackey, Jonathan; Kavanagh, Patrick; Haworth, Thomas J.; Moutzouri, Maria; Gvaramadze, Vasilii V., 2022. Thermal emission from bow shocks. II. 3D magnetohydrodynamic models of zeta Ophiuchi. *Astronomy and Astrophysics* [online]. Vol. 665, A35 [visited on 2025-04-22]. ISSN 0004-6361. Available from DOI: 10.1051/0004-6361/202243531. ADS Bibcode: 2022A&A...665A..35G.

Gualandris, Alessia; Colpi, Monica; Portegies Zwart, Simon; Possenti, Andrea, 2005. Has the Black Hole in XTE J1118+480 Experienced an Asymmetric Natal Kick? *The Astrophysical Journal* [online]. Vol. 618, pp. 845–851 [visited on 2025-03-30]. ISSN 0004-637X. Available from DOI: 10.1086/426126. Publisher: IOP ADS Bibcode: 2005ApJ...618..845G.

Gültekin, Kayhan; Miller, M. Coleman; Hamilton, Douglas P., 2006. Three-Body Dynamics with Gravitational Wave Emission. *The Astrophysical Journal* [online]. Vol. 640, pp. 156–166 [visited on 2025-03-29]. ISSN 0004-637X. Available from DOI: 10.1086/499917. Publisher: IOP ADS Bibcode: 2006ApJ...640..156G.

Haid, S.; Walch, S.; Naab, T.; Seifried, D.; Mackey, J.; Gatto, A., 2016. Supernova blast waves in wind-blown bubbles, turbulent, and power-law ambient media. *Monthly Notices of the Royal Astronomical Society* [online]. Vol. 460, pp. 2962–2978 [visited on 2025-02-26]. ISSN 0035-8711. Available from DOI: 10.1093/mnras/stw1082. Publisher: OUP ADS Bibcode: 2016MNRAS.460.2962H.

Hairer, Ernst; Wanner, Gerhard, 1996. *Solving Ordinary Differential Equations II*. Vol. 14 [online]. Berlin, Heidelberg: Springer [visited on 2025-02-04]. Springer Series in Computational Mathematics. ISBN 978-3-642-05221-7. Available from DOI: 10.1007/978-3-642-05221-7.

Hairer, Ernst; Wanner, Gerhard; Nørsett, Syvert P., 1993. *Solving Ordinary Differential Equations I*. Vol. 8 [online]. Berlin, Heidelberg: Springer [visited on 2025-01-30]. Springer Series in Computational Mathematics. ISBN 978-3-540-78862-1. Available from DOI: 10.1007/978-3-540-78862-1.

Heger, A.; Fryer, C. L.; Woosley, S. E.; Langer, N.; Hartmann, D. H., 2003. How Massive Single Stars End Their Life. *The Astrophysical Journal* [online]. Vol. 591, pp. 288–300 [visited on 2025-03-13]. ISSN 0004-637X. Available from DOI: 10.1086/375341. Publisher: IOP ADS Bibcode: 2003ApJ...591..288H.

Heger, A.; Woosley, S. E., 2002. The Nucleosynthetic Signature of Population III. *The Astrophysical Journal* [online]. Vol. 567, pp. 532–543 [visited on 2025-03-13]. ISSN 0004-637X. Available from DOI: 10.1086/338487. Publisher: IOP ADS Bibcode: 2002ApJ...567..532H.

Hughes, John P., 1987. X-Ray Studies of the Supernova Remnant N132D. I. Morphology. *The Astrophysical Journal* [online]. Vol. 314, p. 103 [visited on 2025-03-04]. ISSN 0004-637X. Available from DOI: 10.1086/165043. Publisher: IOP ADS Bibcode: 1987ApJ...314..103H.

hypre: High Performance Preconditioners, [n.d.]. https://llnl.gov/casc/hypre, https://github.com/hypre-space/hypre.

Israelian, G.; Rebolo, R.; Basri, G.; Casares, J.; Martín, E. L., 1999. Evidence of a supernova origin for the black hole in the system GRO J1655 - 40. *Nature* [online]. Vol. 401, pp. 142–144 [visited on 2025-03-30]. ISSN 0028-0836. Available from DOI: 10.1038/43625. ADS Bibcode: 1999Natur.401..142I.

Janka, Hans-Thomas, 2013. Natal kicks of stellar mass black holes by asymmetric mass ejection in fallback supernovae. *Monthly Notices of the Royal Astronomical Society* [online]. Vol. 434, pp. 1355–1361 [visited on 2025-03-14]. ISSN 0035-8711. Available from DOI: 10.1093/mnras/stt1106. Publisher: OUP ADS Bibcode: 2013MNRAS.434.1355J.

Jayasinghe, Tharindu; Dixon, Don; Povich, Matthew S.; Binder, Breanna; Velasco, Jose; Lepore, Denise M.; Xu, Duo; Offner, Stella; Kobulnicky, Henry A.; Anderson, Loren D.; Kendrew, Sarah; Simpson, Robert J., 2019. The Milky Way Project second data release: bubbles and bow shocks. *Monthly Notices of the Royal Astronomical Society* [online]. Vol. 488, pp. 1141–1165 [visited on 2025-04-22]. ISSN 0035-8711. Available from DOI: 10.1093/mnras/stz1738. Publisher: OUP ADS Bibcode: 2019MNRAS.488.1141J.

Kimball, Chase; Talbot, Colm; L. Berry, Christopher P.; Carney, Matthew; Zevin, Michael; Thrane, Eric; Kalogera, Vicky, 2020. Black Hole Genealogy: Identifying Hierarchical Mergers with Gravitational Waves. *The Astrophysical Journal* [online]. Vol. 900, no. 2, p. 177 [visited on 2025-03-12]. ISSN 0004-637X. Available from DOI: 10.3847/1538-4357/aba518. Publisher: The American Astronomical Society.

Kinugawa, Tomoya; Nakamura, Takashi; Nakano, Hiroyuki, 2021. Formation of binary black holes similar to GW190521 with a total mass of 150 Msolar from Population III binary star evolution. *Monthly Notices of the Royal Astronomical Society* [online]. Vol. 501, pp. L49–L53 [visited on 2025-04-21]. ISSN 0035-8711. Available from DOI: 10.1093/mnrasl/slaa191. Publisher: OUP ADS Bibcode: 2021MNRAS.501L..49K.

Kochanek, Christopher S.; Beacom, John F.; Kistler, Matthew D.; Prieto, José L.; Stanek, Krzysztof Z.; Thompson, Todd A.; Yüksel, Hasan, 2008. A Survey About Nothing: Monitoring a Million Supergiants for Failed Supernovae. *The Astrophysical Journal* [online]. Vol. 684, pp. 1336–1342 [visited on 2025-03-30]. ISSN 0004-637X. Available from DOI: 10.1086/590053. Publisher: IOP ADS Bibcode: 2008ApJ...684.1336K.

Koen, Chris, 2006. On the upper limit on stellar masses in the Large Magellanic Cloud cluster R136. *Monthly Notices of the Royal Astronomical Society* [online]. Vol. 365, pp. 590–594 [visited on 2025-03-13]. ISSN 0035-8711. Available from DOI: 10.1111/j.1365-2966.2005.09739.x. Publisher: OUP ADS Bibcode: 2006MNRAS.365..590K.

Koo, Bon-Chul; McKee, Christopher F., 1992. Dynamics of Wind Bubbles and Superbubbles. I. Slow Winds and Fast Winds. *The Astrophysical Journal* [online]. Vol. 388, p. 93 [visited on 2025-04-03]. ISSN 0004-637X. Available from DOI: 10.1086/171132. Publisher: IOP ADS Bibcode: 1992ApJ...388...93K.

Kourniotis, M.; Wünsch, R.; Martínez-González, S.; Palouš, J.; Tenorio-Tagle, G.; Ehlerová, S., 2023. Simulations of pre-supernova feedback in spherical clouds. *Monthly Notices of the Royal Astronomical Society* [online]. Vol. 521, pp. 5686–5698 [visited on 2025-01-22]. ISSN 0035-8711. Available from DOI: 10.1093/mnras/stad822. Publisher: OUP ADS Bibcode: 2023MNRAS.521.5686K.

Krtička, J.; Kubát, J.; Krtičková, I., 2021. New mass-loss rates of B supergiants from global wind models. *Astronomy and Astrophysics* [online]. Vol. 647, A28 [visited on 2025-01-23]. ISSN 0004-6361. Available from DOI: 10.1051/0004-6361/202039900. ADS Bibcode: 2021A&A...647A..28K.

Lam, Casey Y.; Lu, Jessica R., 2023. A Reanalysis of the Isolated Black Hole Candidate OGLE-2011-BLG-0462/MOA-2011-BLG-191. *The Astrophysical Journal* [online]. Vol. 955, p. 116 [visited on 2025-03-11]. ISSN 0004-637X. Available from DOI: 10.3847/1538-4357/aced4a. Publisher: IOP ADS Bibcode: 2023ApJ...955..116L.

Leitherer, Claus; Robert, Carmelle; Drissen, Laurent, 1992. Deposition of Mass, Momentum, and Energy by Massive Stars into the Interstellar Medium. *The Astrophysical Journal* [online]. Vol. 401, p. 596 [visited on 2025-03-07]. ISSN 0004-637X. Available from DOI: 10.1086/172089. Publisher: IOP ADS Bibcode: 1992ApJ...401..596L.

Levenson, N. A.; Graham, J. R.; Aschenbach, B.; Blair, W. P.; Brinkmann, W.; Busser, J. -U.; Egger, R.; Fesen, R. A.; Hester, J. J.; Kahn, S. M.; Klein, R. I.; McKee, C. F.; Petre, R.; Pisarski, R.; Raymond, J. C.; Snowden, S. L., 1997. The ROSAT HRI X-Ray Survey of the Cygnus Loop. *The Astrophysical Journal* [online]. Vol. 484, pp. 304–312 [visited on 2025-03-04]. ISSN 0004-637X. Available from DOI: 10.1086/304334. Publisher: IOP ADS Bibcode: 1997ApJ...484..304L.

Li, Yin-Jie; Wang, Yuan-Zhu; Tang, Shao-Peng; Fan, Yi-Zhong, 2024. Resolving the Stellar-Collapse and Hierarchical-Merger Origins of the Coalescing Black Holes. *Physical Review Letters* [online]. Vol. 133, p. 051401 [visited on 2025-03-29]. ISSN 0031-9007. Available from DOI: 10.1103/PhysRevLett.133.051401. Publisher: APS ADS Bibcode: 2024PhRvL.133e1401L.

LIGO Scientific Collaboration; Virgo Collaboration; KAGRA Collaboration, 2023. Population of Merging Compact Binaries Inferred Using Gravitational Waves through GWTC-3. *Physical Review X* [online]. Vol. 13, p. 011048 [visited on 2025-03-11]. Available from DOI: 10.1103/PhysRevX.13.011048. Publisher: APS ADS Bibcode: 2023PhRvX..13a1048A.

Lozinskaia, T. A., 1982. Ring nebulae associated with Of stars: statistics, classification, origin. *Astrophysics and Space Science* [online]. Vol. 87, pp. 313–331 [visited on 2025-04-23]. ISSN 0004-640X. Available from DOI: 10.1007/BF00648927. Publisher: Springer ADS Bibcode: 1982Ap&SS..87..313L.

Mandel, Ilya, 2016. Estimates of black hole natal kick velocities from observations of low-mass X-ray binaries. *Monthly Notices of the Royal Astronomical Society* [online]. Vol. 456, pp. 578–581 [visited on 2025-03-30]. ISSN 0035-8711. Available from DOI: 10.1093/mnras/stv2733. Publisher: OUP ADS Bibcode: 2016MNRAS.456..578M.

Mapelli, Michela; Dall'Amico, Marco; Bouffanais, Yann; Giacobbo, Nicola; Arca Sedda, Manuel; Artale, M. Celeste; Ballone, Alessandro; Di Carlo, Ugo N.; Iorio, Giuliano; Santoliquido, Filippo; Torniamenti, Stefano, 2021. Hierarchical black hole mergers in young, globular and nuclear star clusters: the effect of metallicity, spin and cluster properties. *Monthly Notices of the Royal Astronomical Society* [online]. Vol. 505, pp. 339–358 [visited on 2025-04-21]. ISSN 0035-8711. Available from DOI: 10.1093/mnras/stab1334. Publisher: OUP ADS Bibcode: 2021MNRAS.505..339M.

Marchant, Pablo; Renzo, Mathieu; Farmer, Robert; Pappas, Kaliroe M. W.; Taam, Ronald E.; Mink, Selma E. de; Kalogera, Vassiliki, 2019. Pulsational Pair-instability Supernovae in Very Close Binaries. *The Astrophysical Journal* [online]. Vol. 882, no. 1, p. 36 [visited on 2025-03-12]. ISSN 0004-637X. Available from DOI: 10.3847/1538-4357/ab3426. Publisher: The American Astronomical Society.

Marston, A. P., 1996. Large IRAS Shells Around Galactic Wolf-Rayet Stars and the O Star Phase of Wolf-Rayet Evolution. *The Astronomical Journal* [online]. Vol. 112, p. 2828 [visited on 2025-03-08]. ISSN 0004-6256. Available from DOI: 10.1086/118223. Publisher: IOP ADS Bibcode: 1996AJ....112.2828M.

Marston, A. P.; Chu, Y. -H.; Garcia-Segura, G., 1994. A Survey of Nebulae around Galactic Wolf-Rayet Stars in the Southern Sky. I. *The Astrophysical Journal Supplement Series* [online]. Vol. 93, p. 229 [visited on 2025-04-23]. ISSN 0067-0049. Available from DOI: 10.1086/192053. Publisher: IOP ADS Bibcode: 1994ApJS...93..229M.

Martínez-González, Sergio; Wünsch, Richard; Silich, Sergiy; Tenorio-Tagle, Guillermo; Palouš, Jan; Ferrara, Andrea, 2019. Supernovae within Pre-existing Wind-blown Bubbles: Dust Injection versus Ambient Dust Destruction. *The Astrophysical Journal* [online]. Vol. 887, no. 2, p. 198 [visited on 2024-11-13]. ISSN 0004-637X. Available from DOI: 10.3847/1538-4357/ab571b. Publisher: The American Astronomical Society.

Martins, F.; Hillier, D. J.; Paumard, T.; Eisenhauer, F.; Ott, T.; Genzel, R., 2008. The most massive stars in the Arches cluster. *Astronomy and Astrophysics* [online]. Vol. 478, pp. 219–233 [visited on 2025-03-13]. ISSN 0004-6361. Available from DOI: 10.1051/0004-6361:20078469. ADS Bibcode: 2008A&A...478..219M.

McClintock, Jeffrey E.; Remillard, Ronald A., 2006. *Black hole binaries*. Vol. 39 [online]. [visited on 2025-03-11]. Available from DOI: 10.48550/arXiv.astro-ph/0306213. Pages: 157-213 Publication Title: Compact stellar X-ray sources ADS Bibcode: 2006csxs.book..157M.

McKernan, B.; Ford, K. E. S.; Lyra, W.; Perets, H. B., 2012. Intermediate mass black holes in AGN discs - I. Production and growth. *Monthly Notices of the Royal Astronomical Society* [online]. Vol. 425, pp. 460–469 [visited on 2025-03-29]. ISSN 0035-8711. Available from DOI: 10.1111/j.1365-2966.2012.21486.x. Publisher: OUP ADS Bibcode: 2012MNRAS.425..460M.

Mel'nik, A. M.; Dambis, A. K., 2009. Kinematics of OB-associations and the new reduction of the Hipparcos data. *Monthly Notices of the Royal Astronomical Society* [online]. Vol. 400, pp. 518–523 [visited on 2025-03-30]. ISSN 0035-8711. Available from DOI: 10.1111/j.1365-2966.2009.15484.x. Publisher: OUP ADS Bibcode: 2009MNRAS.400..518M.

Message Passing Interface Forum, 2021. *MPI: A Message-Passing Interface Standard Version 4.0*. Available also from: https://www.mpi-forum.org/docs/mpi-4.0/mpi40-report.pdf.

Meyer, D. M. -A.; Mignone, A.; Kuiper, R.; Raga, A. C.; Kley, W., 2017. Bow shock nebulae of hot massive stars in a magnetized medium. *Monthly Notices of the Royal Astronomical Society* [online]. Vol. 464, pp. 3229–3248 [visited on 2025-04-25]. ISSN 0035-8711. Available from DOI: 10.1093/mnras/stw2537. Publisher: OUP ADS Bibcode: 2017MNRAS.464.3229M.

Meyer, D. M. -A.; Petrov, M.; Pohl, M., 2020. Wind nebulae and supernova remnants of very massive stars. *Monthly Notices of the Royal Astronomical Society* [online]. Vol. 493, pp. 3548–3564 [visited on 2025-04-22]. ISSN 0035-8711. Available from DOI: 10.1093/mnras/staa554. Publisher: OUP ADS Bibcode: 2020MNRAS.493.3548M.

Miller-Jones, J. C. A.; Jonker, P. G.; Dhawan, V.; Brisken, W.; Rupen, M. P.; Nelemans, G.; Gallo, E., 2009. The First Accurate Parallax Distance to a Black Hole. *The Astrophysical Journal* [online]. Vol. 706, pp. L230–L234 [visited on 2025-03-30]. ISSN 0004-637X. Available from DOI: 10.1088/0004-637X/706/2/L230. Publisher: IOP ADS Bibcode: 2009ApJ...706L.230M.

Miller-Jones, J. C. A.; Jonker, P. G.; Nelemans, G.; Portegies Zwart, S.; Dhawan, V.; Brisken, W.; Gallo, E.; Rupen, M. P., 2009. The formation of the black hole in the X-ray binary system V404 Cyg. *Monthly Notices of the Royal Astronomical Society* [online]. Vol. 394, pp. 1440–1448 [visited on 2025-03-30]. ISSN 0035-8711. Available from DOI: 10.1111/j.1365-2966.2009.14404.x. Publisher: OUP ADS Bibcode: 2009MNRAS.394.1440M.

Mirabel, Félix, 2017. The formation of stellar black holes. *New Astronomy Reviews* [online]. Vol. 78, pp. 1–15 [visited on 2025-03-11]. ISSN 1387-6473. Available from DOI: 10.1016/j.newar.2017.04.002.

Mirabel, I. F.; Dhawan, V.; Mignani, R. P.; Rodrigues, I.; Guglielmetti, F., 2001. A high-velocity black hole on a Galactic-halo orbit in the solar neighbourhood. *Nature* [online]. Vol. 413, pp. 139–141 [visited on 2025-03-30]. ISSN 0028-0836. Available from DOI: 10.1038/35093060. ADS Bibcode: 2001Natur.413..139M.

Mirabel, I. F.; Mignani, R.; Rodrigues, I.; Combi, J. A.; Rodríguez, L. F.; Guglielmetti, F., 2002. The runaway black hole GRO J1655-40. *Astronomy and Astrophysics* [online]. Vol. 395, pp. 595–599 [visited on 2025-03-30]. ISSN 0004-6361. Available from DOI: 10.1051/0004-6361:20021440. ADS Bibcode: 2002A&A...395..595M.

Mirabel, I. F.; Rodríguez, L. F., 1994. A superluminal source in the Galaxy. *Nature* [online]. Vol. 371, pp. 46–48 [visited on 2025-03-11]. ISSN 0028-0836. Available from DOI: 10.1038/371046a0. ADS Bibcode: 1994Natur.371...46M.

Mirabel, I. Félix; Rodrigues, Irapuan, 2003. Formation of a Black Hole in the Dark. *Science* [online]. Vol. 300, pp. 1119–1121 [visited on 2025-03-30]. ISSN 0036-8075. Available from DOI: 10.1126/science.1083451. ADS Bibcode: 2003Sci...300.1119M.

Müller, Bernhard; Heger, Alexander; Liptai, David; Cameron, Joshua B., 2016. A simple approach to the supernova progenitor-explosion connection. *Monthly Notices of the Royal Astronomical Society* [online]. Vol. 460, pp. 742–764 [visited on 2025-03-13]. ISSN 0035-8711. Available from DOI: 10.1093/mnras/stw1083. Publisher: OUP ADS Bibcode: 2016MNRAS.460..742M.

Nieuwenhuijzen, H.; Jager, C. de, 1990. Parametrization of stellar rates of mass loss as functions of the fundamental stellar parameters M, L, and R. *Astronomy and Astrophysics* [online]. Vol. 231, pp. 134–136 [visited on 2025-04-21]. ISSN 0004-6361. Available from: https://ui.adsabs.harvard.edu/abs/1990A&A...231..134N. ADS Bibcode: 1990A&A...231..134N.

Ninkovic, S., 1998. On the Generalised Schuster Density Law. *Serbian Astronomical Journal* [online]. Vol. 158, p. 15 [visited on 2025-01-23]. Available from: https://ui.adsabs.harvard.edu/abs/1998SerAJ.158...15N. ADS Bibcode: 1998SerAJ.158...15N.

Olson, K. M.; MacNeice, P.; Fryxell, B.; Ricker, P.; Timmes, F. X.; Zingale, M., 1999. PARAMESH: A Parallel, Adaptive Mesh Refinement Toolkit and Performance of the ASCI/FLASH code [online]. Vol. 195, p. 42.03 [visited on 2025-01-22]. Available from: https://ui.adsabs.harvard.edu/abs/1999AAS...195.4203O. Conference Name: American Astronomical Society Meeting Abstracts ADS Bibcode: 1999AAS...195.4203O.

Oppenheimer, J. R.; Snyder, H., 1939. On Continued Gravitational Contraction. *Physical Review* [online]. Vol. 56, no. 5, pp. 455–459 [visited on 2025-03-11]. ISSN 0031-899X. Available from DOI: 10.1103/PhysRev.56.455.

Osterbrock, Donald E., 1988. THE PHYSICS OF GASEOUS NEBULAE. *Publications of the Astronomical Society of the Pacific* [online]. Vol. 100, no. 626, p. 412 [visited on 2025-01-23]. ISSN 1538-3873. Available from DOI: 10.1086/132188. Publisher: IOP Publishing.

Panuzzo, P. et al., 2024. Discovery of a dormant 33 solar-mass black hole in pre-release Gaia astrometry. *Astronomy & Astrophysics* [online]. Vol. 686, p. L2 [visited on 2024-11-13]. ISSN 0004-6361, ISSN 1432-0746. Available from DOI: 10.1051/0004-6361/202449763. Publisher: EDP Sciences.

Pejcha, Ondřej, 2020. *The Explosion Mechanism of Core-Collapse Supernovae and Its Observational Signatures* [online]. [visited on 2024-11-13]. Available from DOI: 10.1007/978-3-030-38509-5_7. Pages: 189-211 Publication Title: Reviews in Frontiers of Modern Astrophysics; From Space Debris to Cosmology ADS Bibcode: 2020rfma.book..189P.

Pejcha, Ondřej; Thompson, Todd A., 2015. The Landscape of the Neutrino Mechanism of Core-collapse Supernovae: Neutron Star and Black Hole Mass Functions, Explosion Energies, and Nickel Yields. *The Astrophysical Journal* [online]. Vol. 801, p. 90 [visited on 2024-11-13]. ISSN 0004-637X. Available from DOI: 10.1088/0004-637X/801/2/90. Publisher: IOP ADS Bibcode: 2015ApJ...801...90P.

Penrose, Roger, 1965. Gravitational Collapse and Space-Time Singularities. *Physical Review Letters* [online]. Vol. 14, pp. 57–59 [visited on 2025-03-11]. ISSN 0031-9007. Available from DOI: 10.1103/PhysRevLett.14.57. Publisher: APS ADS Bibcode: 1965PhRvL..14...57P.

Pierra, Grégoire; Mastrogiovanni, Simone; Perrièss, Stéphane, 2024. *The spin magnitude of stellar-mass binary black holes evolves with the mass: evidence from gravitational wave data* [online]. [visited on 2025-03-29]. Available from DOI: 10.48550/arXiv.2406.01679. Publication Title: arXiv e-prints ADS Bibcode: 2024arXiv240601679P.

Portegies Zwart, Simon F.; McMillan, Stephen L. W., 2002. The Runaway Growth of Intermediate-Mass Black Holes in Dense Star Clusters. *The Astrophysical Journal* [online]. Vol. 576, pp. 899–907 [visited on 2025-03-29]. ISSN 0004-637X. Available from DOI: 10.1086/341798. Publisher: IOP ADS Bibcode: 2002ApJ...576..899P.

Poveda, A.; Ruiz, J.; Allen, C., 1967. Run-away Stars as the Result of the Gravitational Collapse of Proto-stellar Clusters. *Boletin de los Observatorios Tonantzintla y Tacubaya* [online]. Vol. 4, pp. 86–90 [visited on 2025-03-30]. Available from: https://ui.adsabs.harvard.edu/abs/1967BOTT....4...86P. ADS Bibcode: 1967BOTT....4...86P.

Ramachandran, V.; Sander, A. A. C.; Oskinova, L. M.; Schoesser, E. C.; Pauli, D.; Hamann, W. -R.; Mahy, L.; Bernini-Peron, M.; Brigitte, M.; Kubátová, B., 2025. *Comprehensive UV and Optical spectral analysis of Cygnus X-1: Stellar and wind parameters, abundances, and evolutionary implications* [online]. arXiv [visited on 2025-04-21]. Available from DOI: 10.48550/arXiv.2504.05885. ADS Bibcode: 2025arXiv250405885R.

Rao, Anjali; Gandhi, Poshak; Knigge, Christian; Paice, John A.; Leigh, Nathan W. C.; Boubert, Douglas, 2020. Kinematic study of the association Cyg OB3 with Gaia DR2. *Monthly Notices of the Royal Astronomical Society* [online]. Vol. 495, pp. 1491–1500 [visited on 2025-03-14]. ISSN 0035-8711. Available from DOI: 10.1093/mnras/staa1217. Publisher: OUP ADS Bibcode: 2020MNRAS.495.1491R.

Reid, M. J.; McClintock, J. E.; Steiner, J. F.; Steeghs, D.; Remillard, R. A.; Dhawan, V.; Narayan, R., 2014. A Parallax Distance to the Microquasar GRS 1915+105 and a Revised Estimate of its Black Hole Mass. *The Astrophysical Journal* [online]. Vol. 796, p. 2 [visited on 2025-03-30]. ISSN 0004-637X. Available from DOI: 10.1088/0004-637X/796/1/2. Publisher: IOP ADS Bibcode: 2014ApJ...796....2R.

Reid, Mark J.; McClintock, Jeffrey E.; Narayan, Ramesh; Gou, Lijun; Remillard, Ronald A.; Orosz, Jerome A., 2011. The Trigonometric Parallax of Cygnus X-1. *The Astrophysical Journal* [online]. Vol. 742, p. 83 [visited on 2025-03-30]. ISSN 0004-637X. Available from DOI: 10.1088/0004-637X/742/2/83. Publisher: IOP ADS Bibcode: 2011ApJ...742...83R.

Repetto, Serena; Davies, Melvyn B.; Sigurdsson, Steinn, 2012. Investigating stellar-mass black hole kicks. *Monthly Notices of the Royal Astronomical Society* [online]. Vol. 425, pp. 2799–2809 [visited on 2025-03-30]. ISSN 0035-8711. Available from DOI: 10.1111/j.1365-2966.2012.21549.x. Publisher: OUP ADS Bibcode: 2012MNRAS.425.2799R.

Rodriguez, Carl L.; Zevin, Michael; Amaro-Seoane, Pau; Chatterjee, Sourav; Kremer, Kyle; Rasio, Frederic A.; Ye, Claire S., 2019. Black holes: The next generation—repeated mergers in dense star clusters and their gravitational-wave properties. *Physical Review D* [online]. Vol. 100, p. 043027 [visited on 2025-03-29]. ISSN 1550-79980556-2821. Available from DOI: 10.1103/PhysRevD.100.043027. Publisher: APS ADS Bibcode: 2019PhRvD.100d3027R.

Rozyczka, M.; Tenorio-Tagle, G.; Franco, J.; Bodenheimer, P., 1993. On the evolution of supernova remnants. III. Off-centred supernova explosions in pre-existing wind-driven bubbles. *Monthly Notices of the Royal Astronomical Society* [online]. Vol. 261, pp. 674–680 [visited on 2025-02-25]. ISSN 0035-8711. Available from DOI: 10.1093/mnras/261.3.674. Publisher: OUP ADS Bibcode: 1993MNRAS.261..674R.

Sahu, Kailash C. et al., 2022. An Isolated Stellar-mass Black Hole Detected through Astrometric Microlensing. *The Astrophysical Journal* [online]. Vol. 933, p. 83 [visited on 2025-03-11]. ISSN 0004-637X. Available from DOI: 10.3847/1538-4357/ac739e. Publisher: IOP ADS Bibcode: 2022ApJ...933...83S.

Sander, Andreas A. C.; Vink, Jorick S., 2020. On the nature of massive helium star winds and Wolf-Rayet-type mass-loss. *Monthly Notices of the Royal Astronomical Society* [online]. Vol. 499, pp. 873–892 [visited on 2025-03-07]. ISSN 0035-8711. Available from DOI: 10.1093/mnras/staa2712. Publisher: OUP ADS Bibcode: 2020MNRAS.499..873S.

Schure, K. M.; Kosenko, D.; Kaastra, J. S.; Keppens, R.; Vink, J., 2009. A new radiative cooling curve based on an up-to-date plasma emission code. *Astronomy and Astrophysics* [online]. Vol. 508, pp. 751–757 [visited on 2025-01-22]. ISSN 0004-6361. Available from DOI: 10.1051/0004-6361/200912495. ADS Bibcode: 2009A&A...508..751S.

Schwarzschild, Karl, 1916. Über das Gravitationsfeld eines Massenpunktes nach der Einsteinschen Theorie. *Sitzungsberichte der Königlich Preussischen Akademie der Wissenschaften* [online], pp. 189–196 [visited on 2025-03-11]. Available from: https://ui.adsabs.harvard.edu/abs/1916SPAW.....189S. ADS Bibcode: 1916SPAW.....189S.

Sedov, L. I., 1959. *Similarity and Dimensional Methods in Mechanics* [online]. [visited on 2025-03-04]. Available from: https://ui.adsabs.harvard.edu/abs/1959sdmm.book.....S. Publication Title: Similarity and Dimensional Methods in Mechanics ADS Bibcode: 1959sdmm.book.....S.

Sharma, Prateek; Roy, Arpita; Nath, Biman B.; Shchekinov, Yuri, 2014. In a hot bubble: why does superbubble feedback work, but isolated supernovae do not? *Monthly Notices of the Royal Astronomical Society* [online]. Vol. 443, pp. 3463–3476 [visited on 2025-04-22]. ISSN 0035-8711. Available from DOI: 10.1093/mnras/stu1307. Publisher: OUP ADS Bibcode: 2014MNRAS.443.3463S.

Shklovskii, I. S., 1970. Possible Causes of the Secular Increase in Pulsar Periods. *Soviet Astronomy* [online]. Vol. 13, p. 562 [visited on 2025-03-14]. ISSN 0038-5301. Available from: https://ui.adsabs.harvard.edu/abs/1970SvA....13..562S. ADS Bibcode: 1970SvA....13..562S.

Shull Jr., P.; Dyson, J. E.; Kahn, F. D.; West, K. A., 1985. A model for SNR evolution in a cloudy medium and its application to N49. *Monthly Notices of the Royal Astronomical Society* [online]. Vol. 212, pp. 799–808 [visited on 2025-03-04]. ISSN 0035-8711. Available from DOI: 10.1093/mnras/212.4.799. Publisher: OUP ADS Bibcode: 1985MNRAS.212..799S.

Simpson, R. J.; Povich, M. S.; Kendrew, S.; Lintott, C. J.; Bressert, E.; Arvidsson, K.; Cyganowski, C.; Maddison, S.; Schawinski, K.; Sherman, R.; Smith, A. M.; Wolf-Chase, G., 2012. The Milky Way Project First Data Release: a bubblier Galactic disc. *Monthly Notices of the Royal Astronomical Society* [online]. Vol. 424, pp. 2442–2460 [visited on 2025-04-22]. ISSN 0035-8711. Available from DOI: 10.1111/j.1365-2966.2012.20770.x. Publisher: OUP ADS Bibcode: 2012MNRAS.424.2442S.

Smartt, S. J., 2015. Observational Constraints on the Progenitors of Core-Collapse Supernovae: The Case for Missing High-Mass Stars. *Publications of the Astronomical Society of Australia* [online]. Vol. 32, e016 [visited on 2025-03-30]. ISSN 1323-3580. Available from DOI: 10.1017/pasa.2015.17. ADS Bibcode: 2015PASA...32...16S.

Son, L. A. C. van; De Mink, S. E.; Broekgaarden, F. S.; Renzo, M.; Justham, S.; Laplace, E.; Morán-Fraile, J.; Hendriks, D. D.; Farmer, R., 2020. Polluting the Pair-instability Mass Gap for Binary Black Holes through Super-Eddington Accretion in Isolated Binaries. *The Astrophysical Journal* [online]. Vol. 897, no. 1, p. 100 [visited on 2025-03-12]. ISSN 0004-637X. Available from DOI: 10.3847/1538-4357/ab9809. Publisher: The American Astronomical Society.

Sota, A.; Maíz Apellániz, J.; Morrell, N. I.; Barbá, R. H.; Walborn, N. R.; Gamen, R. C.; Arias, J. I.; Alfaro, E. J., 2014. The Galactic O-Star Spectroscopic Survey (GOSSS). II. Bright Southern Stars. *The Astrophysical Journal Supplement Series* [online]. Vol. 211, p. 10 [visited on 2025-03-29]. ISSN 0067-0049. Available from DOI: 10.1088/0067-0049/211/1/10. Publisher: IOP ADS Bibcode: 2014ApJS..211...10S.

Spitzer, L., 1962. Physics of Fully Ionized Gases. *Physics of Fully Ionized Gases* [online] [visited on 2025-01-23]. Available from: https://ui.adsabs.harvard.edu/abs/1962pfig.book.....S/abstract.

Stevenson, Simon; Sampson, Matthew; Powell, Jade; Vigna-Gómez, Alejandro; Neijssel, Coenraad J.; Szécsi, Dorottya; Mandel, Ilya, 2019. The Impact of Pair-instability Mass Loss on the Binary Black Hole Mass Distribution. *The Astrophysical Journal* [online]. Vol. 882, no. 2, p. 121 [visited on 2025-03-12]. ISSN 0004-637X. Available from DOI: 10.3847/1538-4357/ab3981. Publisher: The American Astronomical Society.

Sukhbold, Tuguldur; Ertl, T.; Woosley, S. E.; Brown, Justin M.; Janka, H.-T., 2016. CORE-COLLAPSE SUPERNOVAE FROM 9 TO 120 SOLAR MASSES BASED ON NEUTRINO-POWERED EXPLOSIONS. *The Astrophysical Journal* [online]. Vol. 821, no. 1, p. 38 [visited on 2024-11-13]. ISSN 0004-637X. Available from DOI: 10.3847/0004-637X/821/1/38. Publisher: The American Astronomical Society.

Szécsi, Dorottya; Agrawal, Poojan; Wünsch, Richard; Langer, Norbert, 2022. Bonn Optimized Stellar Tracks (BoOST). Simulated populations of massive and very massive stars for astrophysical applications. *Astronomy and Astrophysics* [online]. Vol. 658, A125 [visited on 2024-11-13]. ISSN 0004-6361. Available from DOI: 10.1051/0004-6361/202141536. ADS Bibcode: 2022A&A...658A.125S.

Tang, Xiaping; Chevalier, Roger A., 2017. Shock evolution in non-radiative supernova remnants. *Monthly Notices of the Royal Astronomical Society* [online]. Vol. 465, pp. 3793–3802 [visited on 2024-11-13]. ISSN 0035-8711. Available from DOI: 10.1093/mnras/stw2978. Publisher: OUP ADS Bibcode: 2017MNRAS.465.3793T.

Taylor, G. I., 1946. The Air Wave Surrounding an Expanding Sphere. *Proceedings of the Royal Society of London Series A* [online]. Vol. 186, pp. 273–292 [visited on 2025-03-04]. ISSN 0080-46301364-5021. Available from DOI: 10.1098/rspa.1946.0044. ADS Bibcode: 1946RSPSA.186..273T.

Tenorio-Tagle, G.; Bodenheimer, P.; Franco, J.; Rozyczka, M., 1990. On the evolution of supernova remnants. I. Explosions inside pre-existing wind-driven bubbles. *Monthly Notices of the Royal Astronomical Society* [online]. Vol. 244, p. 563 [visited on 2024-11-13]. ISSN 0035-8711. Available from: https://ui.adsabs.harvard.edu/abs/1990MNRAS.244..563T. Publisher: OUP ADS Bibcode: 1990MNRAS.244..563T.

Tenorio-Tagle, G.; Rozyczka, M.; Franco, J.; Bodenheimer, P., 1991. On the evolution of supernova remnants - II. Two-dimensional calculationsof explosions inside pre-existing wind-driven bubbles. *Monthly Notices of the Royal Astronomical Society* [online]. Vol. 251, p. 318 [visited on 2025-02-25]. ISSN 0035-8711. Available from DOI: 10.1093/mnras/251.2.318. Publisher: OUP ADS Bibcode: 1991MNRAS.251..318T.

Toalá, J. A.; Arthur, S. J., 2011. Radiation-hydrodynamic Models of the Evolving Circumstellar Medium around Massive Stars. *The Astrophysical Journal* [online]. Vol. 737, p. 100 [visited on 2025-02-27]. ISSN 0004-637X. Available from DOI: 10.1088/0004-637X/737/2/100. Publisher: IOP ADS Bibcode: 2011ApJ...737..100T.

Toalá, J. A.; Arthur, S. J., 2018. On the X-ray temperature of hot gas in diffuse nebulae. *Monthly Notices of the Royal Astronomical Society* [online]. Vol. 478, pp. 1218–1230 [visited on 2025-04-22]. ISSN 0035-8711. Available from DOI: 10.1093/mnras/sty1127. Publisher: OUP ADS Bibcode: 2018MNRAS.478.1218T.

Toalá, J. A.; Guerrero, M. A.; Ramos-Larios, G.; Guzmán, V., 2015. WISE morphological study of Wolf-Rayet nebulae. *Astronomy and Astrophysics* [online]. Vol. 578, A66 [visited on 2025-04-22]. ISSN 0004-6361. Available from DOI: 10.1051/0004-6361/201525706. ADS Bibcode: 2015A&A...578A..66T.

Toalá, J. A.; Oskinova, L. M.; González-Galán, A.; Guerrero, M. A.; Ignace, R.; Pohl, M., 2016. X-Ray Observations of Bow Shocks around Runaway O Stars. The Case of zeta Oph and BD+43°3654. *The Astrophysical Journal* [online]. Vol. 821, p. 79 [visited on 2025-04-22]. ISSN 0004-637X. Available from DOI: 10.3847/0004-637X/821/2/79. Publisher: IOP ADS Bibcode: 2016ApJ...821...79T.

Truelove, J. Kelly; McKee, Christopher F., 1999. Evolution of Nonradiative Supernova Remnants. *The Astrophysical Journal Supplement Series* [online]. Vol. 120, pp. 299–326 [visited on 2025-01-23]. ISSN 0067-0049. Available from DOI: 10.1086/313176. Publisher: IOP ADS Bibcode: 1999ApJS..120..299T.

Ugliano, Marcella; Janka, Hans-Thomas; Marek, Andreas; Arcones, Almudena, 2012. Progenitor-explosion Connection and Remnant Birth Masses for Neutrino-driven Supernovae of Iron-core Progenitors. *The Astrophysical Journal* [online]. Vol. 757, p. 69 [visited on 2025-03-13]. ISSN 0004-637X. Available from DOI: 10.1088/0004-637X/757/1/69. Publisher: IOP ADS Bibcode: 2012ApJ...757...69U.

Vink, Jorick S., 2012. Eta Carinae and the Luminous Blue Variables. In: [online]. eprint: arXiv:0905.3338. Vol. 384, p. 221 [visited on 2025-04-21]. Available from DOI: 10.1007/978-1-4614-2275-4_10. ADS Bibcode: 2012ASSL..384..221V.

Vink, Jorick S., 2018. Fast and slow winds from supergiants and luminous blue variables. *Astronomy and Astrophysics* [online]. Vol. 619, A54 [visited on 2025-04-21]. ISSN 0004-6361. Available from DOI: 10.1051/0004-6361/201833352. ADS Bibcode: 2018A&A...619A..54V.

Vink, Jorick S.; Sander, Andreas A. C., 2021. Metallicity-dependent wind parameter predictions for OB stars. *Monthly Notices of the Royal Astronomical Society* [online]. Vol. 504, pp. 2051–2061 [visited on 2025-03-07]. ISSN 0035-8711. Available from DOI: 10.1093/mnras/stab902. Publisher: OUP ADS Bibcode: 2021MNRAS.504.2051V.

Virtanen, Pauli et al., 2020. SciPy 1.0: Fundamental Algorithms for Scientific Computing in Python. *Nature Methods*. Vol. 17, pp. 261–272. Available from DOI: 10.1038/s41592-019-0686-2.

Weaver, R.; McCray, R.; Castor, J.; Shapiro, P.; Moore, R., 1977. Interstellar bubbles. II. Structure and evolution. *The Astrophysical Journal* [online]. Vol. 218, pp. 377–395 [visited on 2024-11-13]. ISSN 0004-637X. Available from DOI: 10.1086/155692. Publisher: IOP ADS Bibcode: 1977ApJ...218..377W.

Willems, B.; Henninger, M.; Levin, T.; Ivanova, N.; Kalogera, V.; McGhee, K.; Timmes, F. X.; Fryer, C. L., 2005. Understanding Compact Object Formation and Natal Kicks. I. Calculation Methods and the Case of GRO J1655-40. *The Astrophysical Journal* [online]. Vol. 625, pp. 324–346 [visited on 2025-03-30]. ISSN 0004-637X. Available from DOI: 10.1086/429557. Publisher: IOP ADS Bibcode: 2005ApJ...625..324W.

Wongwathanarat, A.; Janka, H. -Th.; Müller, E., 2013. Three-dimensional neutrino-driven supernovae: Neutron star kicks, spins, and asymmetric ejection of nucleosynthesis products. *Astronomy and Astrophysics* [online]. Vol. 552, A126 [visited on 2025-03-14]. ISSN 0004-6361. Available from DOI: 10.1051/0004-6361/201220636. ADS Bibcode: 2013A&A...552A.126W.

Woosley, Stan. E.; Heger, Alexander, 2015. The Deaths of Very Massive Stars [online]. Vol. 412, p. 199 [visited on 2025-03-13]. Available from doi: 10.1007/978-3-319-09596-7_7. Conference Name: Very Massive Stars in the Local Universe Place: eprint: arXiv:1406.5657 ADS Bibcode: 2015ASSL..412..199W.

Wrigge, M.; Wendker, H. J.; Wisotzki, L., 1994. X-ray emission from wind blown interstellar bubbles I. ROSAT observations of NGC 6888. *Astronomy and Astrophysics* [online]. Vol. 286, pp. 219–230 [visited on 2025-04-22]. issn 0004-6361. Available from: https://ui.adsabs.harvard.edu/abs/1994A&A...286..219W. ADS Bibcode: 1994A&A...286..219W.

Wrigge, Matthias; Chu, You-Hua; Magnier, Eugene A.; Wendker, Heinrich J., 2005. X-Ray Emission from Wind-blown Bubbles. III. ASCA SIS Observations of NGC 6888. *The Astrophysical Journal* [online]. Vol. 633, pp. 248–256 [visited on 2025-04-26]. issn 0004-637X. Available from doi: 10.1086/444530. Publisher: IOP ADS Bibcode: 2005ApJ...633..248W.

Wünsch, R; Walch, S; Dinnbier, F; Whitworth, A, 2018. Tree-based solvers for adaptive mesh refinement code flash – I: gravity and optical depths. *Monthly Notices of the Royal Astronomical Society* [online]. Vol. 475, no. 3, pp. 3393–3418 [visited on 2025-01-23]. issn 0035-8711. Available from doi: 10.1093/mnras/sty015.

Yadav, Naveen; Mukherjee, Dipanjan; Sharma, Prateek; Nath, Biman B., 2017. How multiple supernovae overlap to form superbubbles. *Monthly Notices of the Royal Astronomical Society* [online]. Vol. 465, pp. 1720–1740 [visited on 2025-04-22]. issn 0035-8711. Available from doi: 10.1093/mnras/stw2522. Publisher: OUP ADS Bibcode: 2017MNRAS.465.1720Y.

Yang, Y.; Bartos, I.; Gayathri, V.; Ford, K. E. S.; Haiman, Z.; Klimenko, S.; Kocsis, B.; Márka, S.; Márka, Z.; McKernan, B.; O'Shaughnessy, R., 2019. Hierarchical Black Hole Mergers in Active Galactic Nuclei. *Physical Review Letters* [online]. Vol. 123, p. 181101 [visited on 2025-03-29]. issn 0031-9007. Available from doi: 10.1103/PhysRevLett.123.181101. Publisher: APS ADS Bibcode: 2019PhRvL.123r1101Y.

Zevin, Michael; Bavera, Simone S.; Berry, Christopher P. L.; Kalogera, Vicky; Fragos, Tassos; Marchant, Pablo; Rodriguez, Carl L.; Antonini, Fabio; Holz, Daniel E.; Pankow, Chris, 2021. One Channel to Rule Them All? Constraining the Origins of Binary Black Holes Using Multiple Formation Pathways. *The Astrophysical Journal* [online]. Vol. 910, no. 2, p. 152 [visited on 2025-03-12]. issn 0004-637X. Available from doi: 10.3847/1538-4357/abe40e. Publisher: The American Astronomical Society.

Zhekov, Svetozar A., 2014. X-rays from wind-blown bubbles: an XMM-Newton detection of NGC 2359. *Monthly Notices of the Royal Astronomical Society* [online]. Vol. 443, pp. 12–18 [visited on 2025-04-22]. issn 0035-8711. Available from doi: 10.1093/mnras/stu1138. Publisher: OUP ADS Bibcode: 2014MNRAS.443...12Z.